University of Alberta

Reconstructing the recent accumulation history and mass balance trends for high elevation regions of the Devon Island Ice Cap in the Canadian Arctic

by

William Colgan

A thesis submitted to the Faculty of Graduate Studies and Research
in partial fulfillment of the requirements for the degree of

Master of Science

Department of Earth and Atmospheric Sciences

Edmonton, Alberta
Fall 2007

Library and Archives Canada

Published Heritage Branch

395 Wellington Street
Ottawa ON K1A 0N4
Canada

Bibliothèque et Archives Canada

Direction du Patrimoine de l'édition

395, rue Wellington
Ottawa ON K1A 0N4
Canada

Your file Votre référence
ISBN: 978-0-494-33224-5
Our file Notre référence
ISBN: 978-0-494-33224-5

NOTICE:
The author has granted a non-exclusive license allowing Library and Archives Canada to reproduce, publish, archive, preserve, conserve, communicate to the public by telecommunication or on the Internet, loan, distribute and sell theses worldwide, for commercial or non-commercial purposes, in microform, paper, electronic and/or any other formats.

The author retains copyright ownership and moral rights in this thesis. Neither the thesis nor substantial extracts from it may be printed or otherwise reproduced without the author's permission.

AVIS:
L'auteur a accordé une licence non exclusive permettant à la Bibliothèque et Archives Canada de reproduire, publier, archiver, sauvegarder, conserver, transmettre au public par télécommunication ou par l'Internet, prêter, distribuer et vendre des thèses partout dans le monde, à des fins commerciales ou autres, sur support microforme, papier, électronique et/ou autres formats.

L'auteur conserve la propriété du droit d'auteur et des droits moraux qui protège cette thèse. Ni la thèse ni des extraits substantiels de celle-ci ne doivent être imprimés ou autrement reproduits sans son autorisation.

In compliance with the Canadian Privacy Act some supporting forms may have been removed from this thesis.

While these forms may be included in the document page count, their removal does not represent any loss of content from the thesis.

Conformément à la loi canadienne sur la protection de la vie privée, quelques formulaires secondaires ont été enlevés de cette thèse.

Bien que ces formulaires aient inclus dans la pagination, il n'y aura aucun contenu manquant.

Canada

ABSTRACT

Recently observed thickening of the high elevation region of the Devon Island Ice Cap was assessed by (i) investigating inter-annual net accumulation variability, reconstructed from five shallow firn cores, during the 1963 to 2003 period; and (ii) calculating a 40-year mean rate of thickness change, by comparing the mean annual net accumulation and mean specific outflow rates in individual flux basins. This study suggests that the high elevation thickening is likely due to a decrease in the rate of ice outflow, which has exceeded a recent decrease in the annual net accumulation rate. Inter-annual variability in net accumulation and anion deposition was also compared to variability in (i) atmospheric transport to the ice cap, reconstructed using daily site-specific 120 hr air mass back-trajectories, and (ii) the regional sea ice fraction, derived from a passive microwave sea ice concentration dataset. Northern Baffin Bay was found to be the primary moisture source area for the Devon Island Ice Cap, although site-specific atmospheric transport and sea ice fraction variability in southern Baffin Bay and the Beaufort Sea also appear to account for variability in the net accumulation and anion deposition rates. The anion deposition records suggest that anthropogenic emissions have introduced a detectable signal to the sulphate and nitrate deposition records, while regional sea ice variability was found to explain a portion of the chloride and methanesulphonic acid deposition records.

ACKNOWLEDGEMENTS

I wish to express my sincere gratitude to Martin Sharp for fostering my development as a young scientist. By providing me with exciting opportunities and insightful suggestions during this degree, Martin has motivated me to pursue further studies in Arctic research. I would also like to thank Scott Lamoureux of Queen's University for giving me the initial opportunity to participate in Arctic field research, and for encouraging me to consider graduate school.

This thesis would not have been possible without the support of Alberta Ingenuity, the Natural Sciences and Engineering Research Council of Canada, the University of Alberta, the ArcticNet Network of Centres of Excellence, the Polar Continental Shelf Project, the Canadian Circumpolar Institute, and the Northern Scientific Training Program. I am very grateful for their financial and logistical support.

A great number of people have been tremendously helpful in assisting me to complete this thesis. In particular, Hollie Bigelow, Lisa Hyrciw, Joel Barker and Nigel Atkinson who assisted in the laboratory, and Jamie Davis, Dave Burgess, Fiona Cawkwell, Christina Bell and Scott Williamson who assisted in the field. Alex Gardner, Lindsey Nicholson, Inka Koch, Brad Danielson, Roy Coulthard, John England, Alex Wolfe and Jeff Kavanaugh contributed to many helpful discussions around the office.

Finally, I would like to express my gratitude and appreciation to my family, friends and especially my girlfriend Christine, for their support through the ups and downs of graduate school.

TABLE OF CONTENTS

CHAPTER 1: Thesis introduction

1.1 – Introduction

1.1.1 – Motivation 1

1.1.2 – Thickening scenarios 2

1.1.3 – High elevation outflow 4

1.1.4 – High elevation surface mass balance 5

1.1.5 – Glaciochemistry records 6

1.1.6 – Thesis outline and goals 7

1.2 – Literature cited 8

CHAPTER 2: Combined oceanic and atmospheric influences on net accumulation on the Devon Island Ice Cap, Nunavut, Canada

2.1 – Introduction 10

2.2 – Methods

2.1.1 – Shallow firn core recovery 11

2.2.2 – Reconstructing annual net accumulation 12

2.2.3 – Site-specific atmospheric transport 14

2.2.4 – Regional sea ice fraction 15

2.2.5 – Moisture source probabilities 15

2.2.6 – Investigating controls on annual net accumulation 17

2.3 – Results

2.3.1 – Reconstructed annual net accumulation 18

2.3.2 – The high elevation ablation regime 20

2.3.3 – Site-specific low elevation atmospheric transport 21

2.3.4 – Regional sea ice fraction 22

2.3.5 – Regional moisture source probabilities 22

2.3.6 – Variability in relative moisture source probabilities 23

2.3.7 – High and low net accumulation comparison 24

2.3.8 – High and low Arctic Oscillation comparison 24

2.4 – Discussion

2.4.1 – Net accumulation variability 25

2.4.2 – Observed high elevation thickening 26

2.5 – Conclusion 27

2.6 – Literature cited 29

CHAPTER 3: Surface elevation changes in the high elevation region of the Devon Island Ice Cap, Nunavut, Canada *(Co-authored by James A Davis)*

3.1 – Introduction 46

3.2 – Methods

3.2.1 – Surface flow velocities 48

3.2.2 – Delineating flux basins 50

3.2.3 – Determining annual rate of specific outflow 51

3.2.4 – Determining annual net accumulation rate 53

3.2.5 – Determining annual rate of thickness change 53

3.2.6 – Error analysis 54

3.3 – Results

3.3.1 – Annual flux basin thickness change 57

3.4 – Discussion

3.4.1 – Level of uncertainty 58

3.4.2 – Flow regimes 59

3.4.3 – A comparison with remotely sensed estimates 61

3.4.4 – Ice dynamics 62

3.5 – Conclusion 64

3.6 – Literature cited 66

CHATPER 4: Influence of source and transport variability on anion deposition records from the Devon Island Ice Cap, Nunavut, Canada

4.1 – Introduction 78

4.2 – Methods

4.2.1 – High resolution anion analysis 81

4.2.2 – Glaciochemistry records 83
4.2.3 – Long-term anion records: trends 84
4.2.4 – Short-term anion records: source variability 85
4.2.5 – Short-term anion records: transport variability 87
4.3 – Results
4.3.1 – Comparison of the counted and Nye time-scales 88
4.3.2 – Long-term anion records: trends 89
4.3.3 – Short-term anion records: source and transport variability 90
4.4 – Discussion
4.4.1 – Signal-to-noise 92
4.4.2 – Sources of anion deposition variability 93
4.4.3 – Anthropogenic sulphate and nitrate emissions 93
4.4.4 – Sea ice-modulated MSA and chloride emissions 94
4.4.5 – Arctic Oscillation 96
4.5 – Conclusion 96
4.6 – Literature cited 98

CHAPTER 5: Thesis conclusion
5.1 – Conclusion
5.1.1 – Thickening scenarios 109
5.1.2 – Oceanic and atmospheric influences on snowfall and anion dep. 110
5.1.3 – Contribution to glaciology 110
5.1.4 – Future improvements 112
5.2 – Literature cited 112

LIST OF TABLES

2-1 Characteristics of the five shallow firn cores 45
2-2 Net accumulation principal components 45
3-1 Influence of satellite look and ice flow directions on velocity 75
3-2 Width, thickness and basin area of flux gates 75
3-3 Multiple linear regression residual at core sites 76
3-4 Velocity profile uncertainty of flux gates 76
3-5 High elevation outflow, net accumulation and thickness change 77
4-1 Characteristics of the five shallow core sites 108
4-2 Mean anion deposition at the five shallow core sites 108
4-3 Correlation between mean and individual anion records 108

LIST OF FIGURES

1-1 Continuity equation coordinate system 3

2-1 Elevation map of core sites 31

2-2 Mass balance and area versus elevation 31

2-3 Core B ^{137}Cs profile 32

2-4 Reconstructed net accumulation (1963-2003) 33

2-5 Reconstructed net accumulation principal components 33

2-6 120 hr back-trajectories 34

2-7 Seasonal site-specific atmospheric transport 35

2-8 Seasonal regional sea ice fraction 36

2-9 Seasonal relative moisture source probability 37

2-10 PC1 correlated to seasonal relative moisture source probability 38

2-11 PC1 correlated to seasonal sea ice fraction 39

2-12 PC1 correlated to seasonal atmospheric transport 40

2-13 Differences between high and low net accumulation periods 41

2-14 Differences high and low AO index years 42

2-15 Reconstructed and observation mass balance comparison 43

2-16 Annual ice fraction versus elevation 44

2-17 PC1 and relative moisture source probability comparison 44

3-1 Elevation map of core sites 68

3-2 Differences between InSAR-derived and measured velocities 69

3-3 High elevation outflow, net accumulation and thickness change 70

3-4 Net accumulation multiple linear regression 71

3-5 Comparison between measured and InSAR-derived velocity profiles 72

3-6 Horizontal velocity profile uncertainty versus gate width 73

3-7 Drivers of thickness change 73

3-8 Flow regimes and flux basins 74

4-1 Elevation map of core sites 102

4-2 Counted and Nye time-scale comparisons 102

4-3 Reconstructed anion deposition records 103

4-4 SO_2 emission and SO_4^{2-} deposition time series 104

4-5 NDJF seasonal atmospheric transport 104
4-6 MJJAS and ONDJF sea ice fraction PCs 105
4-7 MJJAS sea ice fraction PC and MSA deposition time series 106
4-8 ONDJF and MJJAS atmospheric transport PC1 loading patterns 106
4-9 ONDJF sea ice fraction PC and Cl^- deposition time series 107
4-10 SO_4^{2-} : NO_3^- timeseries 107

Chapter 1: Thesis introduction

1.1 – INTRODUCTION

1.1.1 – Motivation

Second only to the thermal expansion of sea water, increased freshwater input from melting glaciers is the single greatest contributor to sea level rise (Raper and Braithwaite, 2002; 2006). The potential sea level rise contribution of the ice caps and alpine glaciers external to Greenland and Antarctica is far less than the 70 m estimated for the two polar ice sheets. Their smaller size and more temperate environs however, reduce their response time to climatic perturbations and make them potentially more significant short term contributors to sea level rise (Raper and Braithwaite, 2006). Historically, these ice caps and alpine glaciers have been significant contributors to sea level rise, with an estimated contribution of approximately 0.22 ± 0.07 mm a^{-1} during the 1865 to 1990 period (Zuo and Oerlemans, 1997). Between 2001 and 2004 the contribution of these ice masses to sea level rise was approximately 0.77 ± 0.15 mm a^{-1} (Kaser and others, 2006). Recent models suggest that these ice masses will contribute between 46 and 51 mm of sea level rise by the year 2100 (Raper and Braithwaite, 2006). The Devon Island Ice Cap (75 °N, 82 °W) is the sixth largest ice cap in the Arctic, equivalent to approximately 10 mm of sea level rise if melted completely, and is currently estimated to be contributing between 0.036 and 0.046 mm a^{-1} to sea level rise (Dowdeswell and others, 2004; Sharp and others, 2004; Abdalati and others, 2004).

Earnest scientific study of the Devon Island Ice Cap began in 1961, when Koerner (1966) began recording annual surface mass balance measurements along a transect extending from near sea level (50 m) to near the summit (1750 m) in the northwest sector of the ice cap. In 1976, two long ice cores (~ 300 m) were recovered from the summit of the ice cap and used to reconstruct the paleoclimate of the ice cap (Koerner, 1977). Using the thickness of ice layers within each annual layer as a proxy for summer warmth, an "unusually high percentage of ice between the surface and 40 m" depth, relative to the deeper (earlier) portions of these ice cores, provided the first evidence that melt was presently occurring more frequently on the Devon Island Ice Cap than at any other time in the past six centuries (Koerner, 1977). This study was also the first to suggest a

common climatological forcing for variability in the sea ice fraction within the Queen Elizabeth Islands and the melt record from the Devon Island Ice Cap (Koerner, 1977). More recently, a comparison of 1960 aerial photos with 1999 satellite images found a 2.4 % decrease in the surface area of the Devon Island Ice Cap, equivalent to a reduction in volume of 67 ± 12 km^3 (Burgess and Sharp, 2004). This suggests that the ice cap has been loosing mass at approximately 1.6 ± 0.7 km^{3}WE a^{-1} (WE: water equivalent) during this period (Burgess and Sharp, 2004). NASA laser altimetry surveys, conducted in 1995 and 2000, found the high elevation region (> 1200 m) of the Devon Island Ice Cap to be thickening, at a rate of up to 20 cm a^{-1}, while the low elevation region (< 1200 m) was found to be thinning, at a rate of up to 40 cm a^{-1}, resulting in a total contribution of 0.046 mm a^{-1} to sea level rise (Abdalati and others, 2004).

These recent laser altimetry observations provide the motivation for this study of the Devon Island Ice Cap. The main goals of this study are to: (i) investigate whether short term variations in either net accumulation or firnification rates may account for the observed high elevation thickening trend; and (ii) compare the 5-year mean thickening rate, observed by laser altimetry, with a 40-year mean thickening rate calculated from in situ measurements. A more detailed discussion of the primary objectives of this study, as well as several secondary objectives, can be found in section 1.1.6.

1.1.2 – Thickening scenarios

The vertically integrated continuity equation expresses the rate of thickness change of an ice mass (dh/dt; expressed in m a^{-1}; Paterson, 1994):

$$\frac{dh}{dt} = -\frac{dQ}{dx} + \dot{B} \qquad \text{Equation 1-1}$$

where $\dot{B}$ (expressed in m a^{-1}) is the annual net surface mass balance. dQ/dx (expressed in m a^{-1}) is the horizontal divergence of the ice flux. Assuming that the horizontal ice flux is negligible at the main drainage divide ($Q_o \approx 0$ m^2 a^{-1}), where ice flow is by definition strictly vertical, dQ can be taken to represent the ice outflow at distance x from the main ice divide (where $x_o = 0$ m). In this study, x is taken to be the distance along a flow line between the main ice divide and the 1200 m contour, which is used to delineate the high elevation study region (Figure 1-1).

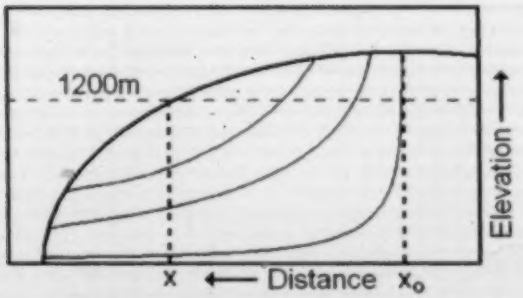

Figure 1-1 – The coordinate system used to define x (the 1200 m contour) and x_o (the main drainage divide) when calculating thickness changes in the region above 1200 m (dQ/dx; Equation 1-1).

An ice mass in steady state equilibrium shows no thickening or thinning ($dh/dt \approx 0$ m a^{-1}). The observed high elevation thickening of the Devon Island Ice Cap therefore suggests that the high elevation region of the ice cap is not in an equilibrium state ($dh/dt > 0$ m a^{-1}). The continuity equation suggests that a positive rate of thickness change can arise from four basic scenarios: (i) if the long term net accumulation rate has remained constant or increased and the rate of outflow has decreased; (ii) if the rate of outflow has remained constant or decreased and the long term net accumulation rate has increased; (iii) if both the outflow and net accumulation rates have decreased, as long as the effect of the decrease in outflow is greater than that of the decrease in net accumulation; and (iv) if both the outflow and net accumulation rates have increased, as long as the net accumulation rate has increased relative to the outflow rate. Therefore, to address the observed thickening of the high elevation region of the Devon Island Ice Cap in terms of the continuity equation, both the high elevation outflow and net accumulation rates must be investigated.

Changes in the rate of firnification, the process by which snow is converted to ice, can result in changes to the firn density profile of an ice mass. A decrease in the rate of firnification results in thickening, while an increase in the rate of firnification results in thinning. Therefore, the rate of firnification during the laser altimetry survey period was compared to a long term mean, to determine whether the observed thickening may be due to a decreased rate of firnification.

1.1.3 – High elevation outflow

The flow of ice from the accumulation zone to the ablation zone, due to gravity, occurs through a combination of viscous deformation, basal sliding and basal sediment deformation (Paterson, 1994). The relative contributions of these three processes to ice flow vary with ice rheology and temperature, as well as local conditions such as topographical controls and the shear strength of the basal substrate (Paterson, 1994). Ice flow velocities are greatest at the surface and decrease with depth. Accurately describing this depth-averaged ice flow velocity is crucial to determining the outflow through a flux gate. Significant uncertainty however, surrounds the determination of depth-averaged ice velocities from measured surface ice velocities. This uncertainty is primarily the result of uncertainty in the proportions of motion due to viscous deformation, basal sliding and basal sediment deformation, which determines the shape of the vertical velocity profile, and hence the relationship between the depth-averaged velocity and the observed surface velocity (Reeh and Paterson, 1988).

This study estimates the ice outflow from the high elevation region of the Devon Island Ice Cap, by summing the individual outflow rates through a series of flux gates aligned along the 1200 m contour. The outflow rate through each flux gate is calculated from in situ surface velocity measurements made between 2005 and 2006. The calculated outflow rate for the high elevation region is compared to a 40-year mean net accumulation rate to determine an approximately 40-year mean rate of thickness change. This calculated 40-year mean rate of thickness change is compared with the 5-year mean rate of thickness change observed by laser altimetry (Abdalati and others, 2004). The rate of thickness change is calculated for 11 flux basins across the high elevation study region, delineated by the 1200 m contour, to assess the spatial distribution of potential thickening or thinning trends.

Although outflow rates have traditionally been regarded as changing over long time-scales, a recent study of the Greenland Ice Sheet has suggested that changes in outflow can be detected at a 40-year time-scale (Paterson and Reeh, 2001). Therefore, a comparison between the 40-year mean and the 5-year mean rates of thickness change will allow the possibilities of increasing or decreasing trends in the outflow rate over the last 40-years to be assessed (Abdalati and others, 2004). Knowledge of whether the rate of

outflow from the high elevation region has been increasing or decreasing, and of its magnitude relative to the net accumulation rate, is needed to properly assess which of the four basic continuity equation scenarios may be responsible for the observed thickening.

1.1.4 – High elevation surface mass balance

The surface mass balance of an ice mass is the sum of its annual mass accumulation (positive) and mass lost by ablation (negative). This study uses shallow firn cores to reconstruct the annual net accumulation record, the sum of accumulation (positive) and ablation (negative), of the high elevation region of the Devon Island Ice Cap between 1963 and 2003. Annual layers in the shallow firn cores were identified using a range of chemical (such as sulphate or isotopes) and physical (such as stratigraphy) records that are known to display annual cycles (Legrand and Mayewski, 1997). Following the identification of annual layers, the net accumulation within a layer can be quantified using density measurements, allowing the surface mass balance history for the core site to be reconstructed over the period covered by the ice core. The shallow firn cores were also used to calculate the area-averaged 40-year mean net accumulation rate over the high elevation region of the Devon Island Ice Cap. This 40-year mean net accumulation rate was compared to the calculated outflow rate to estimate the rate of thickness change.

Following Koerner (1977), the percent of the annual net accumulation present as ice, rather than firn, was quantified to provide a proxy for annual melt. The rate of firnification is influenced by summer melt and subsequent refreezing, with increased melt resulting in an increased rate of firnification. The annual ice fraction record was therefore used to assess whether an anomalously low firnification rate during the survey period could account for the observed high elevation thickening trend.

Annual resolution in the reconstructed net accumulation record allows assessment of whether the 1995 to 2000 period had anomalously high net accumulation, which could account for the thickening observed during that period (Abdalati and others, 2004). This study assumes that the inter-annual variability in net accumulation in the high elevation region of the Devon Island Ice Cap is dominated by variability in snow accumulation, rather than variability in ablation. This assumption is supported by previous findings that

the high elevation annual net accumulation has been positive for the majority of the 1961 to 2003 period, with even the summer net accumulation being positive in some cases, and by the poor correlation seen between the high elevation annual net mass balance record and the low elevation annual net mass balance record. In the low elevation region, ablation processes are known to dominate the variability in annual mass balance (Dyurgerov and Meier, 2005).

To better understand the observed trends and variability in the high elevation annual net accumulation record, the controls on snow accumulation are investigated. The reconstructed net accumulation record is examined in the context of inter-annual variability in site-specific potential moisture source regions, calculated during the 1979 to 2003 period. Moisture source regions are defined through investigation of variability in low elevation atmospheric transport to the ice cap and the regional sea ice fraction.

1.1.5 – Glaciochemistry records

As ions are continuously being deposited on the surfaces of ice masses, shallow firn cores, with dated annual layers, a can provide a temporal proxy for regional atmospheric chemistry (Legrand and Mayewski, 1997). The full lengths of the five shallow firn cores were dated, using the Nye time-scale, to produce annually resolved anion deposition records for each core, with the oldest record extending back to 1922 (Nye, 1963). These five core records allow long term trends in anion deposition to be assessed during the 1922 to 2003 period. Variability is known to be introduced into ice core glaciochemistry records through variability in anion source (emissions), atmospheric transport, and anion deposition (storage) at the core site (Slater and others, 2001). Assessing the highest elevation, and best preserved, core record using annual counting allows inter-annual variability in anion deposition to be compared to inter-annual variability in atmospheric transport and anion source records, both anthropogenic and marine during the 1979 to 2003 period. The anion deposition record also provides insight into the magnitude of inter-site storage variability on the Devon Island Ice Cap, which can be used to assess the percentage 'noise' in these shallow firn core records.

1.1.6 - Thesis outline and goals

Chapter 2 reconstructs an annually-resolved record of the recent (1963 to 2003) annual net accumulation and ice fraction for the high elevation region of the ice cap to explore the influence of variations in atmospheric transport to the ice cap and regional sea ice cover on the inter-annual net accumulation variability in the study region. It also investigates the potential influence of variations in net accumulation or firnification rates on the thickening observed by laser altimetry during the 1995 to 2000 period. A version of this chapter is under review with the *Journal of Glaciology* (W. Colgan and M. Sharp. *submitted manuscript.* Combined ocean and atmospheric influences on the Devon Island Ice Cap, Nunavut, Canada. *J. Glaciol.* 07J044.)

Chapter 3 presents a calculation of the 40-year mean annual rate of thickness change in 11 flux basins within the high elevation region of the Devon Island Ice Cap, by comparing the mean annual net accumulation rate, derived from shallow firn cores, to the mean specific outflow rate, calculated from measured surface velocities, in those flux basins. It then addresses the questions of how representative the laser altimetry observations are of changes in ice thickness across the high elevation region as a whole, and whether a change in ice dynamics has occurred in the high elevation region within the last 40 years. A version of this chapter is also under review with the *Journal of Glaciology* (W. Colgan, J. Davis and M. Sharp. *submitted manuscript.* Surface elevation changes in the high elevation region of the Devon Island Ice Cap, Nunavut, Canada. *J. Glaciol.* 07J042. J. Davis processed all GPS data used in this chapter and was the primary author of Figures 3-3, 3-5 and 3-8.)

Chapter 4 explores the value of the glaciochemistry records from the shallow firn cores, as proxies of anthropogenic emissions and sea ice fraction. It presents both long term records (1922 to 2003) of sulphate (SO_4^{2-}), nitrate (NO_3^-), methanesulphonic acid (CH_3SO_3H) and chloride (Cl^-) deposition, dated using the Nye time-scale, to examine long term trends, as well as a short term (1963 to 2003) annually resolved record of these anions, dated using annual layer counting, to compare inter-annual variability in anion deposition to inter-annual variability in both anthropogenic and sea ice-modulated aerosol emissions, and atmospheric transport to the ice cap.

Chapter 5 uses the reconstructed annual net accumulation record produced in Chapter 2, and the long-term rates of outflow and thickness change calculated in Chapter 3, to assess which of the four thickening scenarios is most likely occurring in the high elevation region. It also reviews the influences of sea ice fraction and atmospheric transport to the ice cap on the annual net accumulation and anion deposition, and discusses the broader contributions and implications of this study of the Devon Island Ice Cap.

1.2 – LITERATURE CITED

Abdalati, W., W. Krabill, E. Frederick, S. Manizade, C. Martin, J. Sonntag, R. Swift, R. Thomas, J. Yungel and R. Koerner. 2004. Elevation changes of ice caps in the Canadian Arctic Archipelago. *J. Geophys. Res.* **109** (F04007), doi:10.1029/2003JF000045.

Burgess, D. and M. Sharp. 2004. Recent changes in areal extent of the Devon Ice Cap, Nunavut, Canada. *Arct., Antarc., and Alp. Res.* **36**, 261-271.

Dowdeswell, J., T. Benham, M. Gorman, D. Burgess and M. Sharp. 2004. Form and flow of the Devon Island Ice Cap, Canadian Arctic. *J. Geophys. Res.*, **109** (F02002), doi:10.1029/2003JF000095.

Dyurgerov, B. and M. Meier. 2005. Glaciers and the changing earth system: a 2004 snapshot. *Occasional paper no. 58*, INSTAAR. University of Colorado.

Johannessen, O., K. Khvorostovsky, M. Miles and L. Bobylev. 2005. Recent ice-sheet growth in the interior of Greenland. *Science*. **310**, 1013-1016.

Kaser, G., J. Cogley, M. Dyurgerov, M. Meier and A. Ohmura. 2006. Mass balance of glaciers and ice caps: consensus estimates for 1961-2004. *Geophys. Res. Lett.*, **35** (L19501), doi:10.1029/2006GL027511.

Koerner, R. 1966. Accumulation on the Devon Island Ice Cap, Northwest Territories, Canada. *J. Glaciol.* **6**, 383-392.

Koerner, R. 1977. Devon Island Ice Cap: core stratigraphy and paleoclimate. *Science*. **196**, 15-18.

Legrand, M. and P. Mayewski. 1997. Glaciochemistry of polar ice cores: a review. *Rev. Geophys.* **35,** 219-243.

Nye, J. 1963. Correction factor for accumulation measured by the ice thickness of the annual layers in an ice sheet. *J. Glaciol.* **4**, 141-150.

Paterson, W. 1994. *The Physics of Glaciers*. Butterworth-Heinemann. pp 255; 481.

Paterson, W. and N. Reeh. 2001. Thinning of the ice sheet in northwest Greenland over the past forty years. *Nature.* **414**, 60-62.

Raper, S. and R. Braithwaite. 2006. Low sea level rise projections from mountain glaciers and icecaps under global warming. *Nature*. **439**, 311-313.

Reeh, N. and W. Paterson. 1988. Application of a flow model to the ice-divide region of the Devon Island Ice Cap, Canada. *J. Glaciol.* **34**, 55-63.

Slater, J., J. Dibb, B. Keim and J. Kahl. 2001. Relations between synoptic-scale transport and interannual variability of inorganic cations in surface snow at

Summit, Greenland: 1992-1996. *J. Geophys. Res.* **106,** 20,897-20,912.
Zuo, Z. and J. Oerlemans. 1997. Contribution of glacier melt to sea-level rise since AD 1865: a regionally differentiated calculation. *Climate Dynamics*. **13**, 835-845.

Chapter 2: Combined oceanic and atmospheric influences on net accumulation on the Devon Island Ice Cap, Nunavut, Canada *

2.1 – INTRODUCTION

There is a significant discrepancy between the observed rate of sea level rise (1.5 ± 0.5 mm a^{-1}) and the rate calculated from the sum of the best estimates of freshwater inputs and thermal expansion (0.7 ± 1.5 mm a^{-1}; Cazenave and Nerem, 2004). This discrepancy indicates that inaccuracies likely exist in sea level observations, calculations of the major contributors to sea level rise, or both. This provides a motivation to improve the quantification of glacier and ice cap contributions to sea level change (Cazenave and Nerem, 2004). Outside of Greenland and Antarctica, the Canadian Arctic Archipelago contains the largest area of glaciated terrain in the world (Dyurgerov and Meier, 2005). Although the potential contribution of the Canadian Arctic ice caps to sea level rise is far less than that of the ice sheets in Greenland and Antarctica, their smaller size and more temperate environs make them potentially significant short term contributors to eustatic sea level rise (Dowdeswell, 1995; Abdalati and others, 2004). The 14,010 km^2 Devon Island Ice Cap (75 °N, 82 °W) is 880 m thick at its deepest point, and has an estimated volume of 3980 km^3, equivalent to approximately 10 mm of sea level rise if melted completely (Dowdeswell and others, 2004; Figure 2-1). The Devon Island Ice Cap is believed to be in long term negative mass balance, losing an estimated 1.6 ± 0.7 km^3 of water equivalent (WE) per year since 1960 (Burgess and Sharp, 2004; Koerner, 2005).

Although only 19 % of the Devon Island Ice Cap area lies above 1200 m (Dowdeswell and others, 2004), the high elevation region is of interest because its mass balance variations are poorly correlated with the overall net balance of the northwest sector of the ice cap, which has been measured annually since 1961 (Koerner, personal communication, 2005; Figure 2-2). The overall net balance of the northwest sector is well correlated with the summer net balance, which suggests that inter-annual mass balance

* *A version of this paper has been submitted to the Journal of Glaciology as "Combined oceanic and atmospheric influences on net accumulation on the Devon Island Ice Cap, Nunavut, Canada." by W. Colgan and M. Sharp (07J044).*

variability is controlled largely by summer melt processes at lower elevations (< 1200 m; Koerner, 2002; Abdalati and others, 2004). At higher elevations however, even the summer balance may be positive, and variability in snow accumulation may account for much of the variability in net balance. In addition, laser altimetry surveys conducted in 1995 and 2000 found the high elevation region (> 1200 m) of the ice cap to be thickening at a rate of up to 20 cm a^{-1} and the low elevation region (< 1200 m) to be thinning at a rate of up to 40 cm a^{-1} (Abdalati and others, 2004). Although this thickening may be due to anomalous accumulation, a decrease in the rate of firnification or a long-term reduction in ice outflow from the accumulation zone, could also explain the laser altimetry observations (Abdalati and others, 2004). Together, these observations suggest that there are at least two mass balance regimes on the Devon Island Ice Cap.

In order to best predict how the mass balance of the Devon Island Ice Cap will respond to future climatic conditions, present-day climatic controls on the mass balance must be well understood. This study aims to create an annually resolved record of the recent (1963 to 2003) net mass balance of the high elevation region, reconstructed from shallow firn cores. This record is used to (i) investigate the influences of variable atmospheric transport and regional sea ice fraction on the inter-annual variability of the high elevation net accumulation and (ii) assess whether the thickening observed by laser altimetry could be explained by anomalous net accumulation or firnification rates.

2.2 – METHODS

2.2.1 – Shallow firn core recovery

To reconstruct a net accumulation record for the high elevation regions of the Devon Island Ice Cap, five shallow (~ 20 m) firn cores (cores A, B, C, D and E) were recovered in April 2004 and April 2005 (Figure 2-1; Table 2-1). The cores were recovered using a Kovacs Mk II corer with 9 cm internal diameter. The length and mass of each approximately 40 cm firn core section was recorded in the field in order to construct a density profile for each core site. The core sections were then wrapped in polyethylene and shipped frozen to the University of Alberta for further analysis.

To constrain the dating of the cores, in situ ^{137}Cs gamma spectrometry was performed in each borehole using an NaI(Tl) detector connected to a multi-channel

analyzer (Dunphy and Dibb, 1994) to identify the depth of the 1963 'bomb' layer resulting from atmospheric thermonuclear weapons testing fallout. Gamma emissions were counted for a 20 min period over three discrete energy bands: a background band (885 to 1001 keV), the ^{137}Cs band (626 to 749 keV), and a ^{109}Cd control band (49 to 117 keV). The background band registers gamma emissions over a randomly selected energy band. These background emissions are expected to remain constant at depths below the level to which cosmic radiation penetrates. In addition to showing the near-surface increase due to cosmic radiation, the ^{137}Cs band also demonstrates a clear secondary peak at depth that is taken to be the 1963 ^{137}Cs peak (Figure 2-3; Dunphy and Dibb, 1994). The observed ^{109}Cd activity, which was three orders of magnitude greater than ^{137}Cs and background activity, originated from a ^{109}Cd source fixed to the detector to ensure the absence of instrument drift. Counts were performed in each of the three bands at 20 cm intervals from the bottom of the borehole upwards, resolving the 1963 ^{137}Cs peak to within ± 10 cm.

2.2.2 – Reconstructing annual net accumulation

The five firn cores were dated more precisely by counting annual layers defined by high-resolution chemical stratigraphy. In the laboratory, a detailed description of the physical stratigraphy of each core was made before the cores were manually sectioned with an electric band saw into slices of 3.1 ± 0.8 cm for anion and $\delta^{18}O$ analyses. Individual slices were melted at room temperature in Whirlpak bags and decanted and stored in 20 mL vials prior to analysis. A Dionex ICS-2500 ion chromatograph was used to measure the concentrations of methanesulphonic acid (MSA; CH_3SO_3H), sulphate (SO_4^{2-}) and chloride (Cl^-) in each sample. A full description of the ion chromatography procedure can be found in Chapter 4. The limits of detection (LOD), defined here as three times the standard deviation of the lowest concentration standard in a randomly selected sequence of eight consecutive runs, were 0.086 μeq L^{-1} for SO_4^{2-}, 0.109 μeq L^{-1} for NO_3^-, 0.079 μeq L^{-1} for MSA and 0.097 μeq L^{-1} for Cl^- (Chapter 4). A GV Isoprime continuous flow mass spectrometer with EuroEA combustion chamber and an injection volume of 0.1 μL was used to measure $\delta^{18}O$ ratios in samples from the highest elevation core (core

C). The instrument was calibrated with SMOW1675, GISP1381, and SLAP1499, with CO_2 as a reference gas.

Annual layers were identified in each core primarily by counting annual SO_4^{2-} concentration maxima. As snowfall SO_4^{2-} concentrations in the High Arctic reach a maximum in the month of March, annual layers defined by SO_4^{2-} maxima therefore define the approximate period March to February (Toom-Sauntry and Barrie, 2002). Within the majority of the annual layers, July / August MSA and $\delta^{18}O$ (when available) maxima and a January / February $\delta^{18}O$ (when available) minimum and Cl^- maximum were also present (Toom-Sauntry and Barrie, 2002). In addition, common horizons defined, for example, by unusually high Cl^- concentrations, were also used for core correlation when present in all five core chemistry records. The net accumulation in water equivalent (WE) was derived for the annual layers in each core using the density profiles measured in the field. This created a record of annual net accumulation between 1963 and 2003 for each core site, where the net accumulation in a given year represents the period from March of that year to February of the following year (Figure 2-4). Within each annual layer, the WE fraction of net accumulation present as ice, rather than firn, was also calculated (Table 2-1).

The thinning of annual layers with depth, due to ice deformation, is often a concern when using ice cores to reconstruct annual net accumulation records. In a previous study however, Pohjola and others (2002) considered the top 18.5 m of an ice core, containing the annual layers between the 1963 ^{137}Cs horizon and the present, to be minimally influenced by deformation. We therefore assume negligible flow-induced layer thinning with depth in our post-1963 reconstructed annual net accumulation record. The annual variation in anion concentrations can be dampened within an ice core chemistry record due to meltwater percolation and consequent anion redistribution (Gjessing and others, 1993). Therefore, unlike annual field measurements of net accumulation, we estimate the uncertainty in annual net accumulation as ± 0.046 mWE, which approximately corresponds to two glaciochemical sample intervals. The dating of each annual layer-by-layer counting is constrained to be accurate to ± 1 to 2 years between the 1963 ^{137}Cs horizon and the present.

Unrotated principal components analysis (PCA) was performed on the five reconstructed annual net accumulation records for the 1963 to 2003 period to extract common patterns of variability. The significance of the resulting principal components (PCs) was assessed using Rule N, which uses Monte Carlo simulation to derive a distribution of eigenvalues from > 100 random datasets of the same length (n) and number of variables (p) as the dataset being considered (Preisendorfer, 1988). The PCs extracted from the dataset being considered are deemed significant if their eigenvalues exceed their respective 95th percentile eigenvalue derived through Monte Carlo simulation (Preisendorfer, 1988). In this paper, the Rule N eigenvalue distribution for a random dataset of $n = 40$ and $p = 5$, representing the five annual net accumulation records during the 1963 to 2003 period, was determined from published tables (Preisendorfer, 1988). Only the primary principal component (PC1), which explains 39 % of the variance in all five records, was deemed significant (Figures 2-4 and 2-5).

2.2.3 – Site-specific atmospheric transport

A record of potential moisture source areas for the Devon Island Ice Cap was compiled for the 1979 to 2003 period. Potential moisture source areas are defined as regions with open water that have a relatively high probability of being traversed by low elevation (< 500 m) air masses en route to the Devon Island Ice Cap. Previous work indicates that precipitating trajectories travel closer to sea level than non-precipitating trajectories, as air masses traveling close to open water surfaces are more likely to acquire moisture by evaporation than higher elevation air masses (Reijmer and others, 2002).

Daily 120 hr kinematic back-trajectories were calculated for the summit of the Devon Island Ice Cap (75 °N, 82 °W) from NCEP / NCAR Reanalysis data (Kalnay and others, 1996), using the METEX model (Zeng and others, 2003), for the period 1979 to 2003. Each trajectory describes the most probable upwind path taken by a parcel of air arriving 500 m above ground level at the summit of the Devon Island Ice Cap at 0000 hr local time each day (Figure 2-6). This is similar to the 400 m arrival level used by Kahl and others (1997) for computing back-trajectories for the summit of the Greenland Ice Sheet. To identify the regions of the Arctic crossed by low elevation air masses en route to the Devon Island Ice Cap, all hourly back-trajectory points below 500 m elevation in a

given month were gridded on an 814 cell conic grid centered on the North Pole (hereafter G814). For a given G814 cell ($_X$), the monthly site-specific low elevation atmospheric transport density (D_{MX}; expressed in km^{-2}) was computed according to:

$$D_{MX} = \frac{b_{MX}}{A_X \times d_M \times 24 h\, d^{-1}} \qquad \text{Equation 2-1}$$

where b_{MX} is the number of hourly back-trajectory points below 500 m elevation counted in a given G814 cell, expressed in hr; A_X is the area of the given G814 cell, expressed in km^2; and d_M is the number of days in the given month. Although site-specific low elevation atmospheric transport provides a physical mechanism to link the ice cap with potential moisture source regions, sea ice cover is also an important control on the distribution of moisture sources (open water) in the Polar Regions.

2.2.4 – Regional sea ice fraction

To improve the identification of potential moisture source regions for the Devon Island Ice Cap, we combined the monthly site-specific low elevation atmospheric transport density history with a monthly open water fraction (O_{MY}) history. Monthly open water fraction values were obtained from the NSIDC northern hemisphere monthly sea ice fraction dataset, gridded in a 4640 cell standard 1° latitude cylindrical projection grid (hereafter G4640), and derived from passive microwave remote sensing using the NASA Team Algorithm (Walsh, 1978; Walsh and Chapman, 2006). Monthly open water fraction is given by:

$$O_{MY} = 1 - S_{MY} \qquad \text{Equation 2-2}$$

where S_{MY} is the monthly sea ice fraction in a given G4640 cell ($_Y$) in a given month ($_M$).

2.2.5 – Moisture source probabilities

Each G814 grid cell in the monthly site-specific low elevation atmospheric transport dataset encompasses multiple G4640 cells in the monthly open water fraction dataset. Therefore, each G4640 cell was assigned the monthly site-specific low elevation atmospheric transport history of the G814 cell within which its centre coordinates reside. Monthly moisture source index values (M_{MY}; expressed in km^{-2}) were generated for each

G4640 cell in a given month by combining monthly site-specific low elevation atmospheric transport and open water fraction histories according to:

$$M_{MY} = D_{MX} \times O_{MY} \qquad \text{Equation 2-3}$$

To express the monthly moisture source index value of each G4640 cell as a dimensionless relative probability, monthly moisture source index values were divided by a theoretical monthly maximum moisture source index value (M'_M; expressed in km^{-2}), which is the theoretical limit that would be reached if both monthly low elevation air mass density and monthly open water fraction reached maxima (D'_M; expressed in km^{-2}; O'_M; dimensionless) within a single cell which served as the sole moisture source for the Devon Island Ice Cap in a given month.

$$M'_M = D'_M \times O'_M \qquad \text{Equation 2-4}$$

To achieve this theoretical maximum moisture source index value, all daily back-trajectory points in a given month would have to lie below 500 m elevation and have access to perpetually open water within the single G814 cell at the summit of the Devon Island Ice Cap in which all trajectories terminate. D'_M is obtained using (2-1), with b_{MX} taken as the theoretical maximum number of daily low elevation back-trajectory points that could occur in a given grid cell in a given month (120 hr d^{-1} × d_{MX}), and A_X as the area of the terminal grid cell (77,788 km^2). M'_M is obtained using (2-4) assuming an open water fraction of 1, and has a value of 6.42×10^{-4} km^{-2}. The relative probability that a given G4640 cell acts a moisture source in a given month (P_{MY}; dimensionless), is then:

$$P_{MY} = \frac{M_{MY}}{M'_M} \qquad \text{Equation 2-5}$$

If $P_{MY} = 0.01$, then an air mass transits within 500 m of open water in G4640 cell '$_Y$' and goes on to travel to the summit of the Devon Island Ice Cap approximately once in every 100 hr in month '$_M$'. Although calculated P_{MY} values ranged between zero and 0.1, only G4640 cells where the P_{MY} value surpassed 0.001 for at least one month a year were chosen for further study. Cells where P_{MY} values are perpetually below 0.001 are unlikely to be important moisture source areas. This simple calculation of P_{MY} values provides only a first approximation of the likely location of moisture sources, as important parameters that influence evaporative moisture uptake, such as air mass temperature, relative humidity, and wind speed are ignored.

Monthly values of site-specific low elevation atmospheric transport density (D_{MX}), sea ice fraction (S_{MY}) and relative moisture source probability (P_{MY}) were averaged for three seasons (s) and denoted as D_{SX}, S_{SY} and P_{SY} respectively: late-summer / early-fall (JASO), late-spring / early-summer (MAMJ) and winter (NDJF; Figures 2-7, 2-8 and 2-9). These seasonal divisions were chosen because approximately twice as much accumulation occurs on the Devon Island Ice Cap in JASO as in MAMJ, and little accumulation occurs during NDJF (Koerner, 2002). The NDJF season represents January and February of a given year, and November and December of the previous year.

2.2.6 – Investigating controls on annual net accumulation

In order to examine the influence of changes in moisture source areas on the annual net accumulation on the Devon Island Ice Cap, during the 1979 to 2003 period, PC1 of the reconstructed annual net accumulation record was correlated with the seasonal relative moisture source probabilities for the JASO, MAMJ and NDJF seasons of each year for each G4640 cell (Figure 2-10). PC1 was also correlated with the seasonal sea ice fraction and site-specific low elevation atmospheric transport records to determine whether changes in relative moisture source probabilities were driven by changes in sea ice fraction or site-specific low elevation atmospheric transport (Figures 2-11 and 2-12). Positive and negative correlations between PC1 and seasonal sea ice fraction and relative moisture source probability were mapped on a continuous colour scale in each G4640 cell, within the moisture source region of interest defined by $P_{MY} > 0.001$. Positive and negative correlations between PC1 and seasonal low elevation air mass density were likewise mapped in each G18 cell within the moisture source region of interest. In all correlation maps, cells exhibiting significant correlations during the period 1979 to 2003 were highlighted ($p < 0.05$, $r > |0.42|$ and $df = 20$).

Differences in the magnitude and distribution of seasonal sea ice fraction, site-specific low elevation atmospheric transport and relative moisture source probability were examined between periods of significantly ($p < 0.05$) higher than average (1979 to 1988) and lower than average (1989 to 2003) annual net accumulation. To ensure that only significant differences ($p < 0.05$) in each dataset between the high and low net accumulation periods were mapped, one-tailed t-tests, assuming two-samples with equal

variance, were conducted for each G4640 or G814 cell to compare the 1979 to 1988 values with the 1989 to 2003 values (Figure 2-13). Similar difference maps were produced to investigate significant differences ($p < 0.05$) in the seasonal sea ice fraction, site-specific low elevation atmospheric transport and relative moisture source probability datasets between the three highest (1983, 1989 and 1994) and the three lowest (1979, 1981 and 1993) Arctic Oscillation (AO) JASO index years during the 1979 to 2003 period (NOAA, 2005; Figure 2-14).

2.3 – RESULTS

2.3.1 – Reconstructed annual net accumulation

The mean of the five reconstructed annual net accumulation records shows distinct periods of above (1964 to 1967, 1971 to 1979 and 1984 to 1988) and below (1968 to 1970, 1981 to 1983 and 1989 to 2003) average annual net accumulation (Figure 2-4). A t-test reveals a significant ($p < 0.05$) decrease in the mean annual net accumulation during the 1989 to 2003 period relative to the 1963 to 1988 period (Figure 2-4). Similar standard deviations of annual net accumulation suggest the five records exhibit similar amounts of inter-annual variability (Table 2-1). During the 1963 to 2003 period the annual net accumulation records of cores A, B and C, which comprise the western elevation transect, were significantly positively correlated with each other ($p < 0.05$ and $df = 40$), while cores D and E, in the northeast and southeast respectively of the high elevation region of the Devon Island Ice Cap, were not significantly correlated with each other, or with the other three cores ($p > 0.05$ and $df = 40$). This grouping is consistent with the results of the PCA, which loaded cores A, B and C together under PC1 and loaded cores E and D individually under PC2 and PC3 respectively (Table 2-2). These three principal components together explain 82 % of the variance in the Devon Island Ice Cap annual net accumulation record over the 1963 to 2003 period, although only PC1 is considered significant according to Rule N (Figure 2-5).

Good correlation between the annually measured mass balance record and the reconstructed annual net accumulation records is of paramount importance to instill faith in the use of shallow firn cores to reconstruct mass balance. PC1, which approximates the mean annual net accumulation record, and loads most strongly on the western cores (A, B

and C), was compared to the measured mass balance record from the northwest sector of the high elevation region of the Devon Island Ice Cap (Figures 2-1 and 2-4). The measured mass balance record used here is the mean of the annual mass balance measurements at 1250 m, 1350 m, 1450 m, 1550 m, 1650 m and 1750 m elevation (Koerner, personal communication, 2005). The two records were significantly correlated ($p < 0.01$, $r = 0.41$ and $df = 40$) over the 1963 to 2003 period (Figure 2-15).

The two records share a period of good correlation (1963 to c. 1988), followed by a period of poor correlation (c. 1989 to 2003; Figure 2-15). During the initial period of good correlation, differences arise from noise in either the measured or reconstructed records, or most likely both. Although the estimated error of the reconstructed annual net accumulation layer thickness (± 0.046 mWE) is less than that estimated for an annual mass balance measurement (± 0.054 mWE; Koerner, 1970), the core-based reconstructions have a dating uncertainty of ± 1 to 2 years. In addition, the two records may be differentially affected by meltwater redistribution, the unfortunate result of which is that "any one annual layer contains accumulation from more than one year, and yet does not contain all the accumulation from the year when the layer was deposited" (Koerner, 1970). During the period of poor correlation, PC1 exhibits decreased variability and appears to systematically underestimate net accumulation, in comparison to the observed mass balance record (Figure 2-15). Increased annual ice fractions during the 1989 to 2003 period in comparison to the 1963 to 1988 period (Figure 2-16) are likely evidence of both increased melt water percolation between annual layers, which may have resulted in a decrease in PC1 variation, and increased and / or more variable firn density, which may have resulted in more brittle firn cores and less accurate density profile measurements. However, the reconstructed and observed records are derived from different areas of the high elevation region of the ice cap, and the differences could therefore be real and indicative of spatial differences in net accumulation. Despite these possible sources of error, the overall good correlation between PC1 and the measured northwest mass balance record lends confidence to our use of the firn core records as net accumulation proxies for the high elevation region of the Devon Island Ice Cap.

2.3.2 – The high elevation ablation regime

Although this paper focuses on the influence of moisture source areas on net accumulation, further controls of annual net accumulation variability, especially the ablation regime of the high elevation region of the Devon Island Ice Cap, must also be understood to draw meaningful conclusions. To gain insight into the high elevation ablation regime, the mean number of melt days experienced at each core site between 2000 and 2004 was calculated according to the regression model developed by Wang and others (2005; Table 2-1). The melt day model, which incorporates both the elevation and the distance of each core site from a fixed point in Baffin Bay, found melt duration to vary between 18 and 31 days depending on core site (Table 2-1; Wang and others, 2005). The mean annual ice fraction, defined as the WE proportion of annual net accumulation present as ice rather than firn in each core, varied between 0.16 and 0.62, depending on core site, during the 1963 to 2003 period (Table 2-1). Both the calculated number of melt days and the observed ice fractions indicate that the five core sites experience some melt.

Extrapolation of annual ice fraction-elevation relations for the five core sites suggests that the upper limit of the superimposed ice zone (the lower limit of the wet snow zone) was found at approximately 1000 m elevation during the 1963 to 1988 period and 1160 m during the 1989 to 2003 period (Figure 2-16). Likewise, the upper limit of the percolation zone (the lower limit of the dry snow zone) was found at approximately 1880 m elevation during the 1963 to 1988 period and 2025 m during the 1989 to 2003 period (well above the 1930 m summit of the Devon Island Ice Cap; Figure 2-16). Although all five cores demonstrated an increase in annual ice fraction during the 1989 to 2003 period relative to the 1963 to 1988 period, the increase was only significant ($p < 0.05$) in cores C, D and E, according to two-tailed t-tests assuming two samples with equal variance.

The four lowest core sites were likely located in the percolation zone during the 1963 to 1988 period, with the highest core site (core C) possibly being in the dry snow zone. With the apparent upward migration of the both the snow line and the dry snow line, the four lowest elevation core sites are likely now located in the wet snow zone, while the highest elevation core site is now in the percolation zone. Melt and percolation would be expected to have had the greatest influence on the lowest elevation core (core

A) during the 1989 to 2003 period. The core A record is significantly correlated ($p < 0.05$ and $df = 23$) with the records from cores B and C at higher elevations along the western transect during the 1963 to 1988 period, but is not significantly correlated ($p > 0.05$ and $df = 13$) with those records during the 1989 to 2003 period. A reduction of the variability in the anion concentration records, due to increased meltwater percolation and anion redistribution, is evident in the most recent sections of each shallow firn core, but is most pronounced in core A.

2.3.3 – Site-specific low elevation atmospheric transport

Variations in atmospheric circulation can result in variations in both firn chemistry and accumulation. Maps of JASO, MAMJ and NDJF seasonal site-specific low elevation atmospheric transport provide a clear picture of the relative frequency with which air masses arriving at the summit of the Devon Island Ice Cap cross different regions of the Arctic below 500 m. Nearly all the calculated back-trajectories demonstrate a curvature indicative of a strong cyclonic influence on air mass transport routes (Reijmer and others, 2002; Figure 2-6). Seasonal site-specific low elevation atmospheric transport density patterns are similar for all three seasons (Figure 2-7). Transport density is a function of distance from the back-trajectory termination point, and values reach a maximum in all seasons where back-trajectories converge on the common G814 termination cell of the Devon Island Ice Cap. Variability in site-specific low elevation atmospheric transport increases rapidly with distance from the Devon Island Ice Cap and values range over three orders of magnitude throughout the Arctic. In all seasons, Northern Baffin Bay and the Queen Elizabeth Islands (QEI) appear to be primary regions traversed by low elevation air masses, while southern Baffin Bay, the western Arctic Ocean and Foxe Basin / northern Hudson Bay are traversed less often (Figure 2-7). The Atlantic Ocean east of Greenland and the Eurasian portion of the Arctic Ocean are not traversed frequently in any season (Figure 2-7). Either Greenland acts as an effective block to low elevation air mass transport from Europe and the east (Kahl and others, 1997), or the 120 hr back-trajectories do not capture the longer transport paths from Eurasia.

2.3.4 – Regional sea ice fraction

During the NDJF season, high sea ice fractions occur throughout the Arctic Archipelago and Baffin Bay (Figure 2-8). During the MAMJ season, as the polar pack margin migrates northward, the sea ice fraction begins to decrease in both Hudson and Baffin Bays, along the Eurasian shelves and in the North Open Water (NOW) Polynya (Figure 2-8). During the JASO season, Baffin Bay has a high open water fraction, and sea ice fractions also reach a minimum along the Eurasian shelves, in the coastal zone of the Beaufort Sea, throughout the QEI and in Hudson's Bay (Figure 2-8).

2.3.5 – Regional moisture source probabilities

The coupling of site-specific atmospheric back-trajectories with the observed regional sea ice fraction record allowed investigation of temporal and spatial variations in the relative probability that a given G4640 cell would act as a moisture source for the Devon Island Ice Cap in a given season. Primary moisture source areas were defined as regions where $P_{SY} > 0.01$ (Figure 2-9: blue), while secondary moisture source areas were defined as regions where $0.001 < P_{SY} < 0.01$ (Figure 2-9: orange). The sum of relative moisture source probabilities in all grid cells in the JASO season ($\Sigma P_{SY} = 1.95$) is approximately three times the sum of the probabilities in MAMJ ($\Sigma P_{SY} = 0.62$), which agrees well with the finding that there is approximately twice as much accumulation on the Devon Island Ice Cap in JASO as in MAMJ (Koerner, 2002). The sum of relative moisture source probabilities in NDJF ($\Sigma P_{SY} = 0.23$) is approximately three times less than during MAMJ, or nine times less than JASO, supporting the finding of minimal accumulation during this season. During the NDJF season no primary moisture source areas are found within 5 days transit time of the Devon Island Ice Cap, as relative moisture source probabilities drop to near zero in most G4640 cells. Only localized bands of secondary moisture source areas are inferred along the Greenland coast and in the NOW (Figure 2-9). During the MAMJ season a primary moisture source area is inferred in the NOW, with the remainder of Baffin Bay inferred to be a secondary moisture source area (Figure 2-9). During the JASO season, the main accumulation season on the Devon Island Ice Cap (Koerner, 2002), the northern half of Baffin Bay is inferred to be a primary moisture source area, while the southern half of Baffin Bay, the Labrador Sea,

the QEI, the southeast Beaufort Sea and Foxe Basin / northern Hudson Bay are inferred to be secondary moisture source regions (Figure 2-9). Relative moisture source probabilities surpass 0.04 in northern Baffin Bay in JASO, which represents one air mass traversing within 500 m of open water en route to the summit of the Devon Island Ice Cap once in every 25 hr, or almost daily, for the entire season in this region.

2.3.6 – Variability in relative moisture source probabilities

PC1 was correlated with the calculated relative moisture source probability histories of the G4640 cells in the NDJF, MAMJ and JASO seasons during the 1979 to 2003 period. PC1 is positively correlated ($p < 0.05$ and $df = 20$) with the relative moisture source probability histories of northern Hudson Bay in NDJF and southern Baffin Bay in both the MAMJ and JASO seasons (Figure 2-10: highlighted clusters; Figure 2-17). To discern whether changes in site-specific low elevation atmospheric transport or sea ice fraction are primarily responsible for changes in relative moisture source probabilities, correlations between these two independent datasets and PC1 were examined. No areas of significant negative correlation ($p > 0.05$ and $df = 20$) exist between the sea ice fraction history of southern Baffin Bay or northern Hudson Bay and PC1 in any season (Figure 2-11). A negative correlation ($p < 0.05$ and $df = 20$) does exist between PC1 and sea ice fraction in central Baffin Bay during NDJF (Figure 2-11). Positive correlations ($p < 0.05$ and $df = 20$) are seen between the site-specific low elevation atmospheric transport history of southern Baffin Bay and PC1 in the MAMJ and JASO seasons (Figure 2-12). We conclude therefore, that the positive correlation exhibited between the relative moisture source probability history of southern Baffin Bay and PC1 in MAMJ and JASO is primarily driven by positive correlations with site-specific low elevation atmospheric transport, and not the sea ice fraction history of this region. Unlike the southern Baffin Bay clusters, the positive correlation between the relative moisture source probability history of northern Hudson Bay and PC1 in the NDJF season appears to be explained through coupled variation of site-specific low elevation atmospheric transport and sea ice fraction, as neither record is independently correlated ($p > 0.05$ and $df = 20$) to PC1 in the northern Hudson's Bay region (Figures 2-11 and 2-12).

2.3.7 – High and low net accumulation comparison

The difference in magnitude and distribution of relative moisture source probabilities between periods of significantly ($p < 0.05$; t-test) higher than average (1979 to 1988) and lower than average (1989 to 2003) annual net accumulation was examined for the JASO season, the main accumulation season on the Devon Island Ice Cap (Koerner, 2002). During the higher net accumulation period, JASO relative moisture source probabilities were significantly lower ($p < 0.05$; t-test) in southwest Baffin Bay, the central QEI and the Beaufort Sea and significantly higher ($p < 0.05$; t-test) in southeast Baffin Bay (Figure 2-13). These differences in relative moisture source probability appear to be the result of significant differences ($p < 0.05$; t-test) in site-specific low elevation atmospheric transport (southern Baffin Bay), sea ice fraction (Beaufort Sea) or both (QEI; Figure 2-13). Southeast Baffin Bay functions as a secondary moisture source in JASO and is the only region to experience significantly higher relative moisture source probabilities during the period of higher annual net accumulation. Southeast Baffin Bay is also the only region where the relative moisture source probability history is positively correlated ($p < 0.05$ and $df = 20$) with PC1 during the 1979 to 2003 period.

2.3.8 – High and low Arctic Oscillation comparison

The difference in magnitude and distribution of JASO relative moisture source probabilities was examined between the three years of highest (1983, 1989 and 1994) and lowest (1979, 1981 and 1993) JASO Arctic Oscillation (AO) index values during the 1979 to 2003 period. During the JASO season, relative moisture source probabilities in southern Baffin Bay were found to be significantly higher ($p < 0.05$; t-test), and moisture source probabilities in the QEI surrounding the Boothia Peninsula significantly lower ($p < 0.05$; t-test) during the three lowest JASO AO years than in the three highest JASO AO years (Figure 2-14). The significant differences in relative moisture source probability in southern Baffin Bay appear to be the result of significant differences ($p < 0.05$; t-test) in site-specific low elevation atmospheric transport, while those around the Boothia Peninsula are due to either coupled variation in the site-specific low elevation atmospheric transport and sea ice fraction records, or random noise in the relative

moisture source probability dataset (Figure 2-14). Although a significant difference is seen in relative moisture source probabilities between the three highest and lowest JASO AO index years, a two-tailed t-test, assuming two samples with equal variance, reveals no significant difference ($p > 0.05$) in annual net accumulation between the two groups of years. The PC1 net accumulation signal is not significantly correlated to the JASO AO index during the 1963 to 2003 period ($p > 0.05$, $r = 0.16$ and $df = 38$). Nor is it significantly correlated to the AO index in NDJF, the season when the AO signal attains its greatest annual strength ($p > 0.05$, $r = -0.10$ and $df = 38$).

2.4 – DISCUSSION

2.4.1 – Net accumulation variability

Relative moisture source probabilities reached a maximum in both magnitude and extent in northern Baffin Bay during the JASO season, and a minimum in the NDJF season, with intermediate values in the MAMJ season (Figure 2-9). This supports observations that most accumulation on the Devon Island Ice Cap occurs during the JASO season, with the least accumulation during the NDJF season, and intermediate accumulation during the MAMJ season (Koerner, 2002).

The significant differences in moisture source probabilities between high and low JASO AO years, and also high and low net accumulation periods, have been shown to be the result of either significant changes in sea ice fraction or site-specific low elevation atmospheric transport (or both). Several authors have noted that both sea ice motion (Wang and Ikeda, 2000; Rigor and others, 2002; Barber and Hanesiak, 2004) and atmospheric circulation (Eckhardt and others, 2003) are related to hemispheric oscillations, such as the North Atlantic Oscillation (NAO) or the AO (the timeseries of which are highly correlated: $r = 0.92$; Ambaum and others, 2001). The AO can therefore be expected to influence the distribution and significance of moisture source areas, as well as the precipitation that falls at a given site. We find that the AO influences the distribution and magnitude of the relative moisture source probabilities we calculate from both atmospheric transport and sea ice variables.

The clusters of significant correlation between PC1 and relative moisture source probability histories in Hudson's Bay in NDJF and southern Baffin Bay in MAMJ

(highlighted in Figure 2-10) do not reside in seasonally identified primary or secondary moisture source regions (Figure 2-9). In addition to being significantly correlated with PC1, the JASO southern Baffin Bay cluster resides in a secondary moisture source region, where the relative moisture source probabilities exhibit significant changes ($p < 0.05$; t-test) between both high and low annual net accumulation periods and high and low JASO AO index years (Figures 2-13 and 2-14).

As the variability (standard deviation) in annual net accumulation is only 24 to 40 % of the mean annual net accumulation (Table 2-1), we interpret this to imply that the majority of net accumulation originates from the proximal primary moisture source regions, while variability is superimposed by the more distal secondary moisture source regions. The correlation of net accumulation variability with more distal moisture source areas, in southern Baffin Bay and Hudson's Bay, supports this notion. As the moisture source record of southern Baffin Bay is primarily controlled by the site-specific low elevation atmospheric transport record, this suggests that regions with relatively low air mass traverse densities, but high variability, may influence annual net accumulation variability through episodic events such as vigorous cyclones.

The finding that variability in low elevation atmospheric transport to the Devon Island Ice Cap in regions remote from the core sites (> 2000 km) is better correlated to the variability in the reconstructed annual net accumulation records than the local (< 100 km) sea ice fraction record suggests that core records likely contain proxies for more than just local sea ice fraction (Grumet and others, 2001; Kinnard and others, 2006). The use of glaciochemistry records will help to identify potential sea salt aerosol sources, which may be common with the potential moisture sources, and further clarify the relative roles of atmospheric transport and sea ice fraction variability in ice core proxy records (Chapter 4; Kinnard and others, 2006).

2.4.2 – Observed high elevation thickening

The airborne laser altimetry measurements, conducted between 1995 and 2000, suggested that many ice caps in the Canadian Arctic, including Agassiz, Prince of Wales, Devon, Barnes and Penny, thinned significantly at low elevations, while remaining in equilibrium or thickening slightly at high elevations (Abdalati and others, 2004). These

measurements suggest that high elevation regions of the Devon Island Ice Cap thickened by up to 20 cm a^{-1} during this period (Abdalati and others, 2004). Although Abdalati and others (2004) suggest these observations can be explained by anomalously high accumulation throughout the Arctic during the observation period (1995 to 2000), compared to the 52-year mean from three Arctic weather stations (Iqaluit, Clyde River and Eureka), our reconstructed record clearly demonstrates anomalously low annual net accumulation during this period (0.180 ± 0.010 mWE a^{-1}) in comparison to the annual net accumulation for the entire 1963 to 2003 period (0.220 ± 0.040 mWE a^{-1}; Figure 2-4). This conclusion is also supported by the observed mass balance record, which finds the annual net mass balance of the 1995 to 2000 period to be anomalously low in comparison to the 1961 to 2003 mean annual observed net mass balance (Koerner, 2005). This decrease in annual net accumulation, relative to the long term mean, during the study period, would be expected to result in surface lowering or ice cap thinning.

Changes in the rate of firnification can also influence the relative elevation of an ice surface. The reconstructed annual ice fraction record suggests that the annual ice fraction was higher during the 1989 to 2003 period than the during 1963 to 1988 period (Figure 2-17). If accumulation is constant, increasing annual ice fractions, due to increasing annual melt, result in an increasing rate of firnification and overall surface lowering. Trends of increased annual summer melt fractions, in comparison to long term mean values, are recognized throughout the Arctic (Dowdeswell, 1995). Therefore, the rate of firnification is likely to have been greater than the long term mean rate of firnification during the laser altimetry survey period. If the observed high elevation thickening cannot be explained by either (i) an increased net accumulation or (ii) a decreased rate of firnification, then a change in the ice dynamics, such as a reduction in ice outflow relative to the long term net accumulation rate, from the high elevation accumulation zone to the low elevation ablation zone, may be responsible for the observed high elevation thickening of the Devon Island Ice Cap.

2.5 – CONCLUSION

An annual net accumulation record for the period 1963 to 2003 was derived from PCA of independently reconstructed annual net accumulation records from five shallow

firn cores recovered from the percolation zone of the Devon Island Ice Cap. The PC1 of the reconstructed net accumulation record was significantly correlated with the observed surface mass balance during the 1963 to 2003 period. The mean annual net accumulation of the five cores was significantly lower during the 1989 to 2003 period, than in the 1963 to 1988 period. Conversely, the mean annual ice fraction in the five cores was higher (significantly higher in three cores) during the 1989 to 2003 period, than in the 1963 to 1988 period. This study used this reconstructed record of annually-resolved net accumulation and ice fraction of the high elevation region to: (i) identify site-specific atmospheric and oceanic controls on the inter-annual variability of the high elevation net accumulation; and (ii) investigate the hypothesis that the thickening observed by laser altimetry is driven by anomalous net accumulation or firnification rates during the survey period.

(i) Relative moisture source probabilities were found to reach a maximum in northern Baffin Bay during JASO, and a minimum throughout the Arctic during NDJF. Variability in seasonal low elevation atmospheric transport appears to play a more important role in determining variability in relative moisture source probability than variability in seasonal sea ice fraction. The good correlation between the relative moisture source probability history of southern Baffin Bay and PC1, as well as the significant differences seen in this region between the high and low annual net accumulation periods, suggests that variability in this region is closely tied to the variability superimposed on the annual net accumulation record of the Devon Island Ice Cap. The JASO moisture source probability of this region was also found to decrease during the three highest JASO AO index years.

(ii) The reconstructed core records indicate the rate of annual net accumulation was lower than its 1963 to 2003 mean during the laser altimetry survey period. The current rate of firnification in the high elevation region of the Devon Island Ice Cap is likely higher than its long term mean, as the reconstructed 1989 to 2003 mean annual ice fraction was higher than the 1963 to 1988 mean at the five core sites. We therefore speculate that a change in the ice dynamics, such as a decrease in ice outflow from the high elevation accumulation zone, may be responsible for the observed high elevation thickening of the Devon Island Ice Cap.

2.6 – LITERATURE CITED

Abdalati, W., W. Krabill, E. Frederick, S. Manizade, C. Martin, J. Sonntag, R. Swift, R. Thomas, J. Yungel and R. Koerner. 2004. Elevation changes of ice caps in the Canadian Arctic Archipelago. *J. Geophys. Res.* **109** (F04007), doi:10.1029/2003JF000045

Ambaum, M., B. Hoskins and D. Stephenson. 2001. Arctic Oscillation or North Atlantic Oscillation? *J. Climate*. **14,** 3495-3507.

Barber, D. and J. Hanesiak. 2004. Meteorological forcing of sea ice concentrations in the southern Beaufort Sea over the period 1979 to 2000. *J. Geophys. Res.* **109** (C06014), doi:10.1029/2003JC002027.

Burgess, D. and M. Sharp. 2004. Recent changes in areal extent of the Devon ice cap, Nunavut, Canada. *Arct., Antarc., Alp. Res.* **36**, 261-271.

Cazenave, A. and R. Nerem. 2004. Present-day sea level change: observations and causes. *Rev. Geophys.* **42** (RG3001), doi:10.1029/2003RG000139.

Dowdeswell, J. 1995. Glaciers in the High Arctic and recent environmental change. *Phil. Trans. R. Soc. Lon. Series A*. **352**, 321-334.

Dowdeswell, J., T. Benham, M. Gorman, D. Burgess and M, Sharp. 2004. Form and flow of the Devon Island Ice Cap, Canadian Arctic. *J. Geophys. Res.* **109** (F02002), doi:10.1029/2003JF000095.

Dunphy, P. and Dibb, J. 1994. ^{137}Cs gamma-ray detection at Summit, Greenland. *J. Glaciol.* **40**, 87-92.

Dyurgerov, B. and M. Meier. 2005. Glaciers and the changing earth system: a 2004 snapshot. *Occasional paper no. 58*, INSTAAR. University of Colorado.

Eckhardt, S., A. Stohl, S. Beirle, N. Spichtinger, P. James, C. Forster, C. Junker, T.Wagner, U. Platt, and S. G. Jennings. 2003. The North Atlantic Oscillation controls air pollution transport to the Arctic. *Atmos. Chem. Phys.* **3,** 1769-1778.

Gjessing, Y., I. Hanssen-Bauer, Y. Fuiji, T. Kameda, K. Kamiyama and T. Kawamura. 1993. Chemical fractionation in sea ice and glacier ice. *Bull. Glac. Res.* **11**, 1-8.

Grumet, N., C. Wake, P. Mayewski, G. Zielinski, S. Whitlow, R. Koerner, D. Fisher and J. Woollett. 2001. Variability of sea-ice extent in Baffin Bay over the last millennium. *Climate Change*. **49**, 129-145.

Kahl, J., D. Martinez, H. Kuhns, C. Davidson, J. Jaffrezo and J. Harris. 1997. Airmass trajectories to Summit, Greenland: a 44-year climatology and some episodic events. *J. Geophys. Res.* **102**, 26,861-26,875.

Kalnay, E., M. Kanamitsu, R. Kistler, W. Collins, D. Deaven, L. Gandin, M. Iredell, S. Sasha, G. White, J. Woollen, Y. Zhu, M. Chelliah, W. Ebisuzaki, W. Higgins, J. Janowiak, K. Mo, C. Ropelewski, J. Wang, A Leetmaa, R. Reynolds, R. Jenne and D. Joseph. 1996. The NCEP/NCAR 40-year reanalysis project. *Bull. Amer. Meteor. Soc.* **77**, 437-471.

Kinnard, C., C. Zdanowicz, D. Fisher and C. Wake. 2006. Calibration of an ice-core glaciochemical (sea slat) record with sea ice variability in the Canadian Arctic. *Ann. Glaciol.* **44**, 383-390.

Koerner, R. 1970. The mass balance of the Devon Island Ice Cap, Northwest Territories, Canada, 1961-66. *J. Glaciol.* **9**, 325-336.

Koerner, R. 2002. Glaciers of the High Arctic Islands. *US Geological Survey Professional Paper*. 1386-J: 111 –164.

Koerner, R. 2005. Mass balance of glaciers in the Queen Elizabeth Islands, Nunavut, Canada. *Ann. Glaciol.* **42**, 417-423.

NOAA, 2005: The Arctic Oscillation Index. http://cpc.ncep.noaa.gov/products/precip/Cwlink/daily_ao_index/ao_index.html. Accessed 13 August 2005.

Pohjola, V., T. Martma, H. Meijer, J. Moore, E. Isaksson, R. Vaikmäe, R. van de Wal. 2002. Reconstruction of three centuries of annual accumulation rates based on the record of stable isotopes of water from Lomonosovfonna, Svalbard. *Ann. Glaciol.* **35**, 57-62.

Preisendorfer, R. 1988. *Principal component analysis in meteorology and oceanography.* Ed. C. Mobley. Elsevier. pp. 199-206.

Reijmer, C., M. van den Broeke and M. Scheele. 2002. Air parcel trajectories and snowfall related to five deep drilling locations in Antarctica based on the ERA-15 dataset. *J. Climate.* **15**, 1957-1968.

Rigor, I., J. Wallace and R. Colony. 2002. Response of sea ice to the Arctic Oscillation. *J. Climate.* **15**, 2648-2663.

Toom-Sauntry, D. and L. Barrie. 2002. Chemical composition of snowfall in the High Arctic: 1990–1994. *Atmos. Environ.* **36**, 2683–2693.

Walsh, J. 1978. A data set on Northern Hemisphere sea ice extent: World Data Center-A for Glaciology (Snow and Ice). *Glaciological Data, Report GD-2 Part 1.* 49-51.

Walsh, J. and W. Chapman. 2006. Northern Hemisphere Sea Ice Data Set. http://arctic.atmos.uiuc.edu/SEAICE. Accessed 15 June 2006.

Wang, L., M. Sharp, B. Rivard, S. Marshall and D. Burgess. 2005. Melt season duration on Canadian Arctic ice caps, 2000-2004. *Geophys. Res. Lett.* **32** (L19502), 101.1029/2005GL023962.

Zeng, J., M. Katsumoto, R. Ide, M. Inagaki, H. Mukai and Y. Fujinuma. 2003. Development of meteorological data explorer for Windows. In: *Data Analysis and Graphic Display System for Atmospheric Research Using PC.* Ed. Y. Fujinuma. CGER-M014-2003. Center for Global Environmental Research, NIES, 19-72.

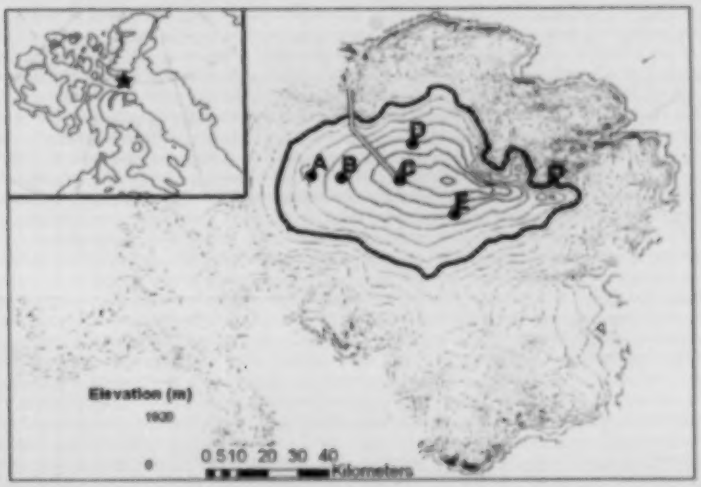

Figure 2-1 – Shaded contour map of the Devon Island Ice Cap (100 m interval), with the high elevation region enclosed by the 1200 m contour (black line). The locations of the five shallow firn core sites (A, B, C, D and E) and the northwest sector mass balance transect (white line) are shown (Koerner, 1970). **Inset:** The location of the Devon Island Ice Cap within the Canadian Arctic Archipelago.

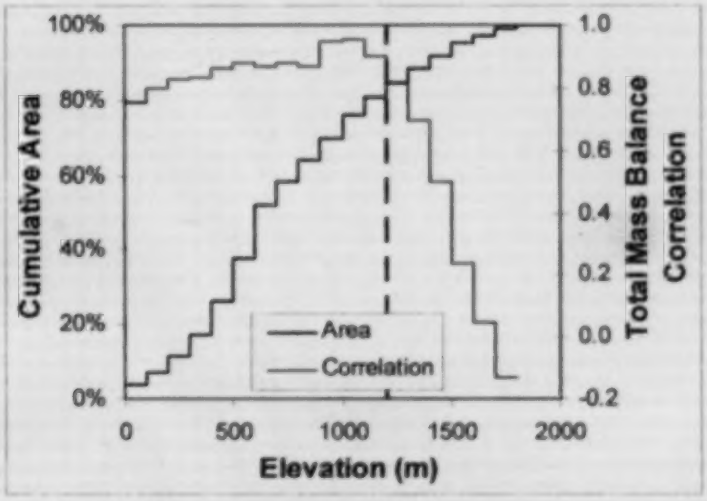

Figure 2-2 – Correlation between the overall northwest transect annual mass balance and the net balance of individual elevation bands over the period 1961 to 1998 (Dyurgerov and Meier, 2005). The cumulative area of the ice cap with elevation is also shown (Dowdeswell and others, 2004). The dashed line denotes 1200 m elevation.

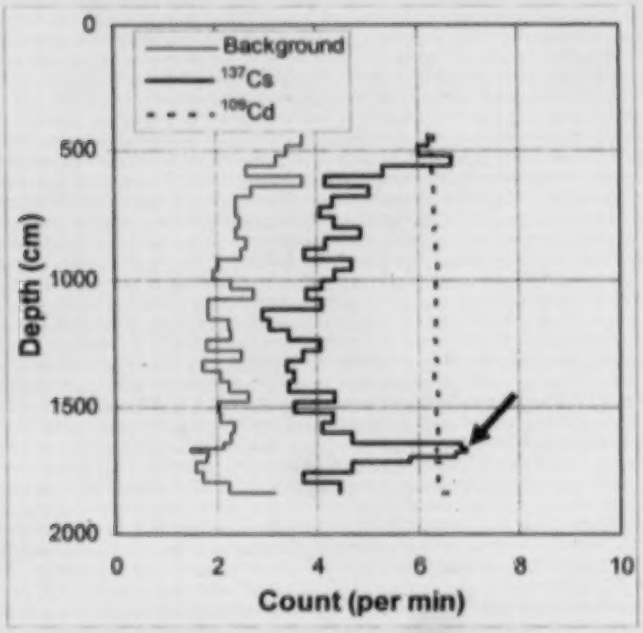

Figure 2-3 – The gamma count rates in the core B borehole over three discrete energy bands: a background band (885 to 1001 keV), the ^{137}Cs band (626 to 749 keV), and a ^{109}Cd control band (49 to 117 keV). ^{109}Cd gamma count values have been divided by 1000 for scaling. The 1963 ^{137}Cs horizon at 1660 ± 10 cm depth is shown (arrow).

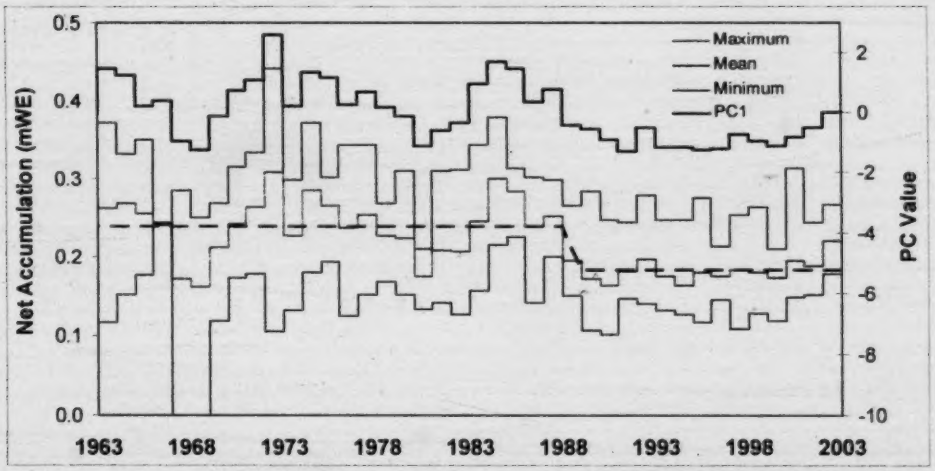

Figure 2-4 – The reconstructed mean (thick grey line) and minimum and maximum (thin lines) annual net accumulation values in the high elevation region of the Devon Island Ice Cap. The primary principal component (PC1) derived from the five core records is also shown (thick black line) as well as a significant decrease ($p < 0.05$; t-test) in the mean annual net accumulation after 1988 (dashed).

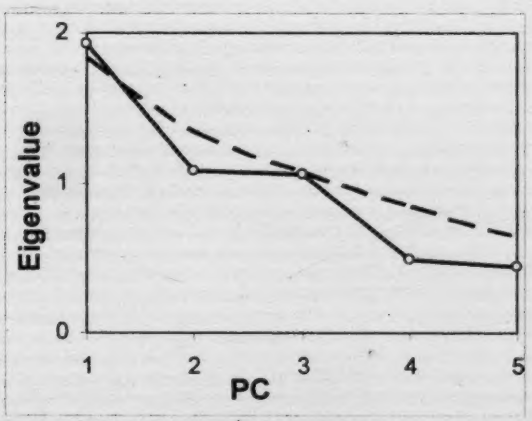

Figure 2-5 – An eigenvalue versus principal component (PC) scree plot (solid line) indicates that only the primary principal component (PC1; variance explained = 39 %) is significant according to Rule N (Preisendorfer, 1988).

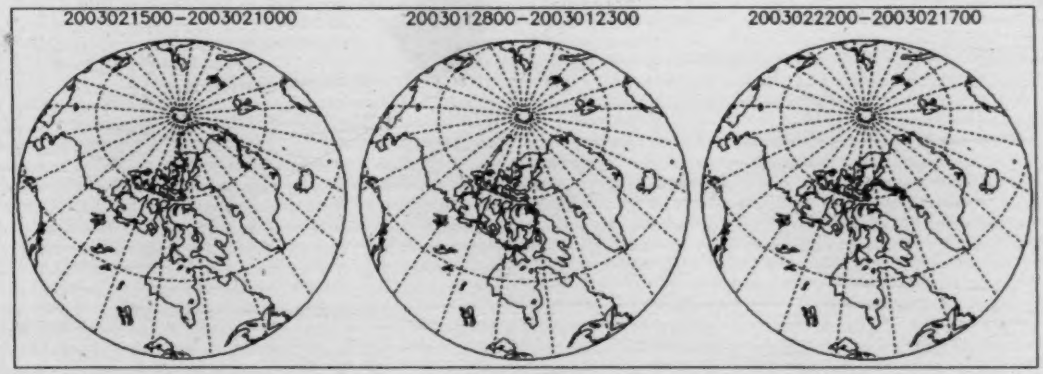

Figure 2-6 – Three randomly selected 120 hr daily back-trajectories produced by the METEX model for the winter of 2003. The back-trajectory termination date, the time of arrival at the summit of the Devon Island Ice Cap, is listed in YYYY/MM/DD/HH format followed by the back-trajectory initiation date. The nodes along each line indicate six-hourly positions.

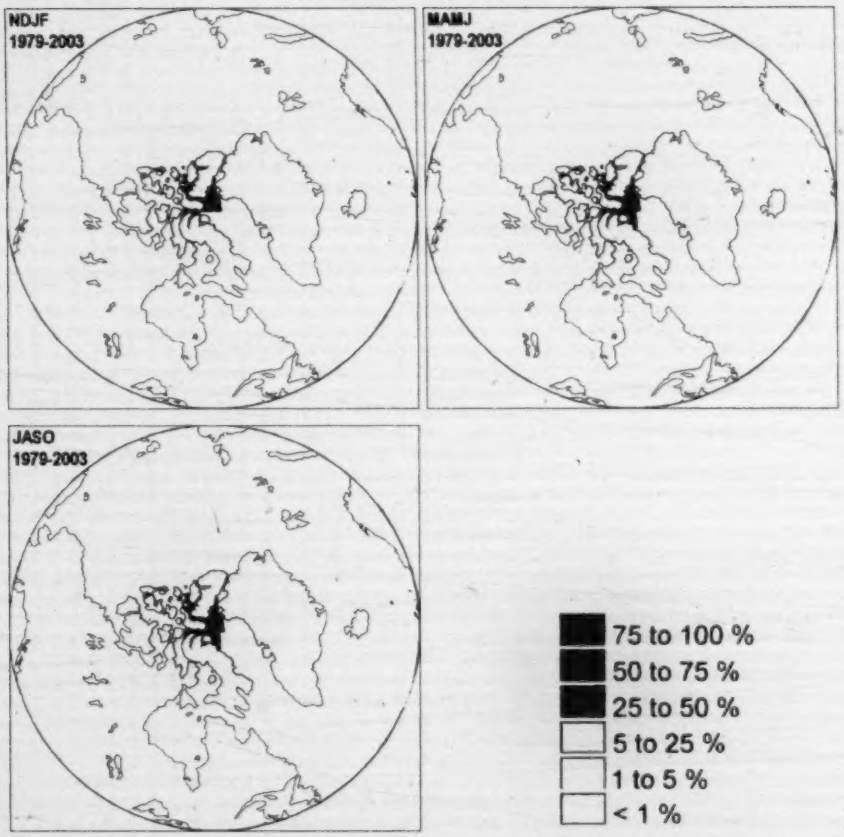

Figure 2-7 – The seasonal site-specific low elevation atmospheric transport en route to the Devon Island Ice Cap (D_{SX}; Equation 2-1) in G814 cells, during the period 1979 to 2003, in the winter (NDJF: **Top Left**), late-spring / early-summer (MAMJ: **Top Right**) and late-summer / early-fall (JASO: **Bottom Left**) seasons. D_{SX} values for each cell are expressed as a per cent of the maximum D_{SX} value achieved in each season.

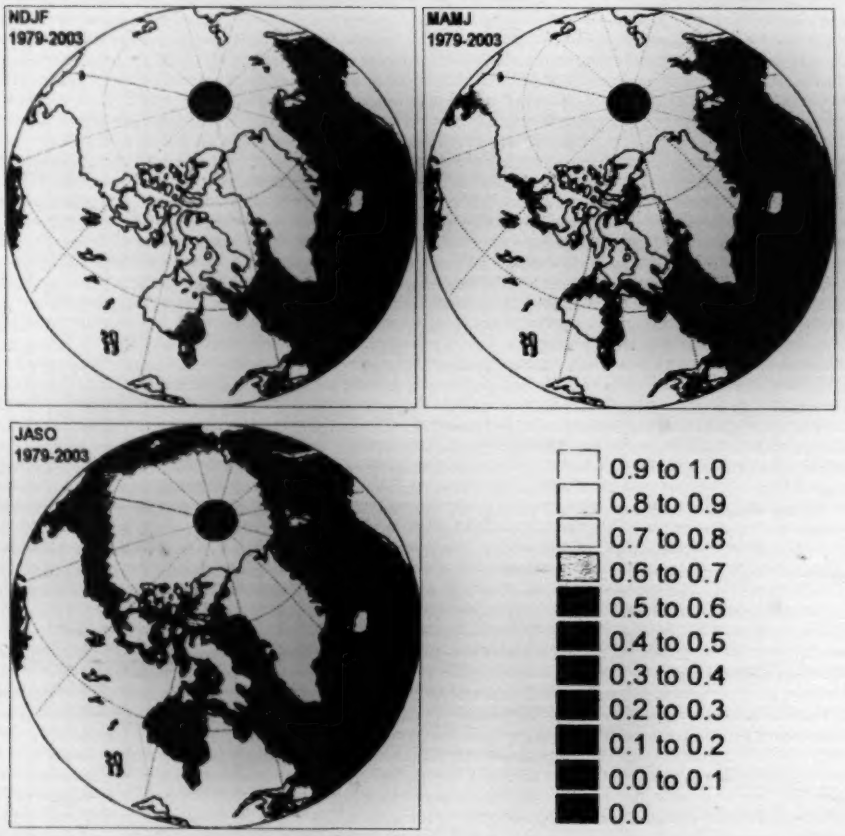

Figure 2-8 – The seasonal sea ice fraction (S_{SY}) in G4640 cells, during the period 1979 to 2003, in the winter (NDJF: **Top Left**), late-spring / early-summer (MAMJ: **Top Right**) and late-summer / early-fall (JASO: **Bottom Left**) seasons (Walsh and Chapman, 2006).

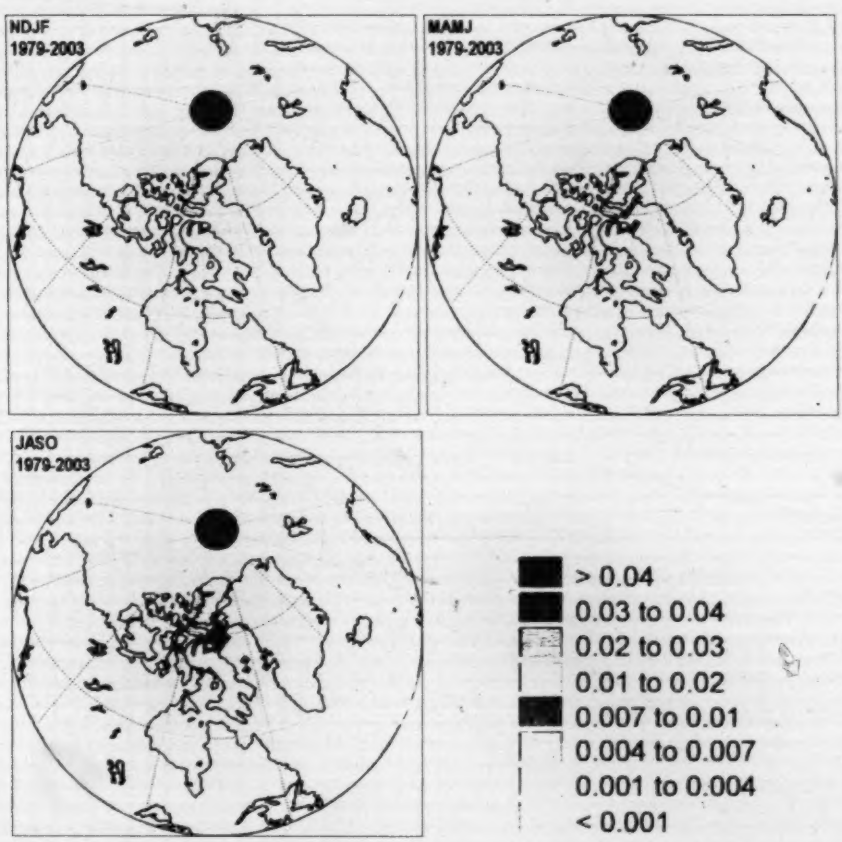

Figure 2-9 – The seasonal relative moisture source probability (P_{SY}; Equation 2-5) of a given G4640 cell in the winter (NDJF: **Top Left**), late-spring / early-summer (MAMJ: **Top Right**) and late-summer / early-fall (JASO: **Bottom Left**) seasons, during the 1979 to 2003 period.

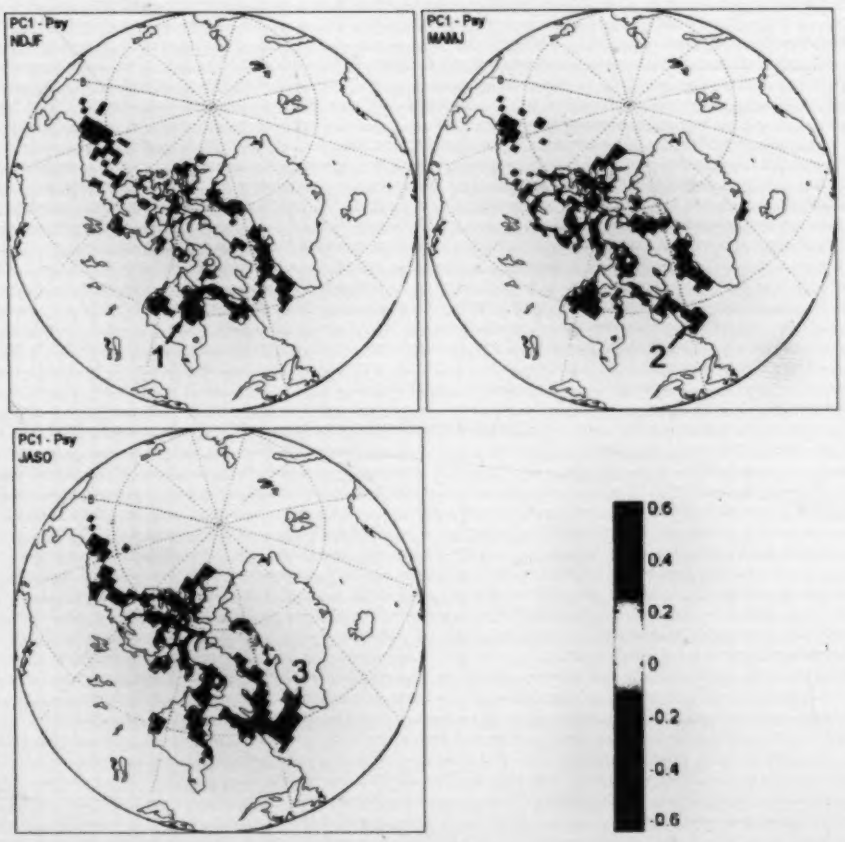

Figure 2-10 – The spatial distribution of correlations between net accumulation PC1 and the seasonal moisture source probabilities (P_{SY}; Figure 2-9) in the winter (NDJF: **Top Left**), late-spring / early-summer (MAMJ: **Top Right**) and late-summer / early-fall (JASO: **Bottom Left**) seasons, during the 1979 to 2003 period. G4640 grid cells with significant correlations ($p < 0.05$, $r > |0.42|$ and $df = 20$) are highlighted. P_{SY} timeseries of the labeled clusters are plotted in Figure 2-17. Grey areas indicate $P_{MY} < 0.001$.

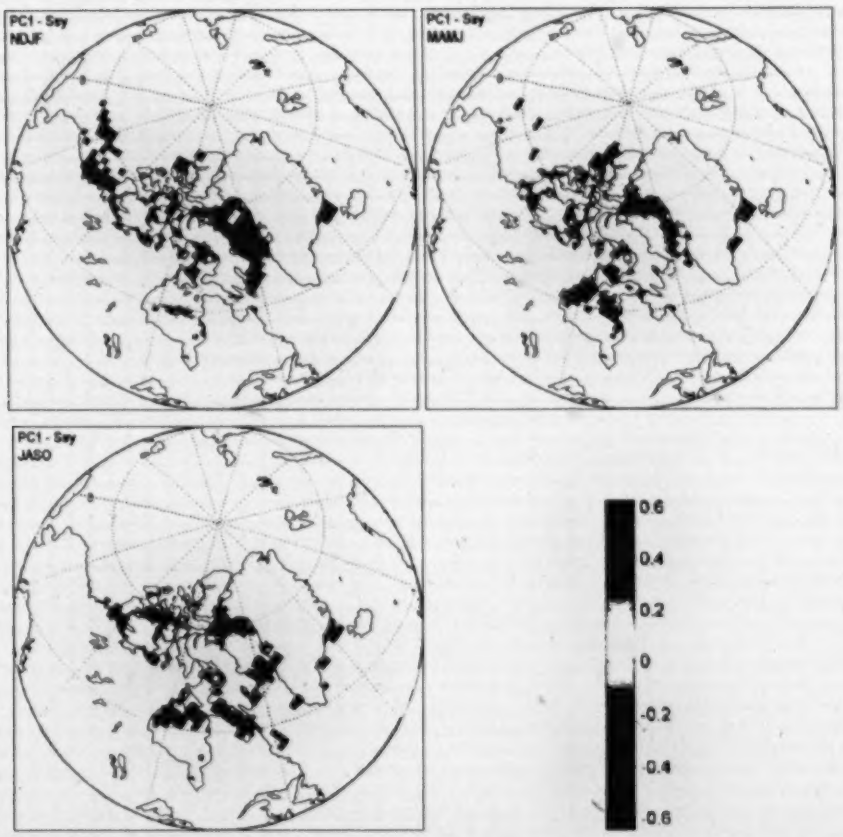

Figure 2-11 – The spatial distribution of correlations between net accumulation PC1 and the seasonal sea ice concentration (S_{SY}; Figure 3-8) in the winter (NDJF: **Top Left**), late-spring / early-summer (MAMJ: **Top Right**) and late-summer / early-fall (JASO: **Bottom Left**) seasons, during the 1979 to 2003 period. G4640 grid cells with significant correlations ($p < 0.05$, $r > |0.42|$ and $df = 20$) are highlighted. Grey areas indicate $P_{MY} < 0.001$.

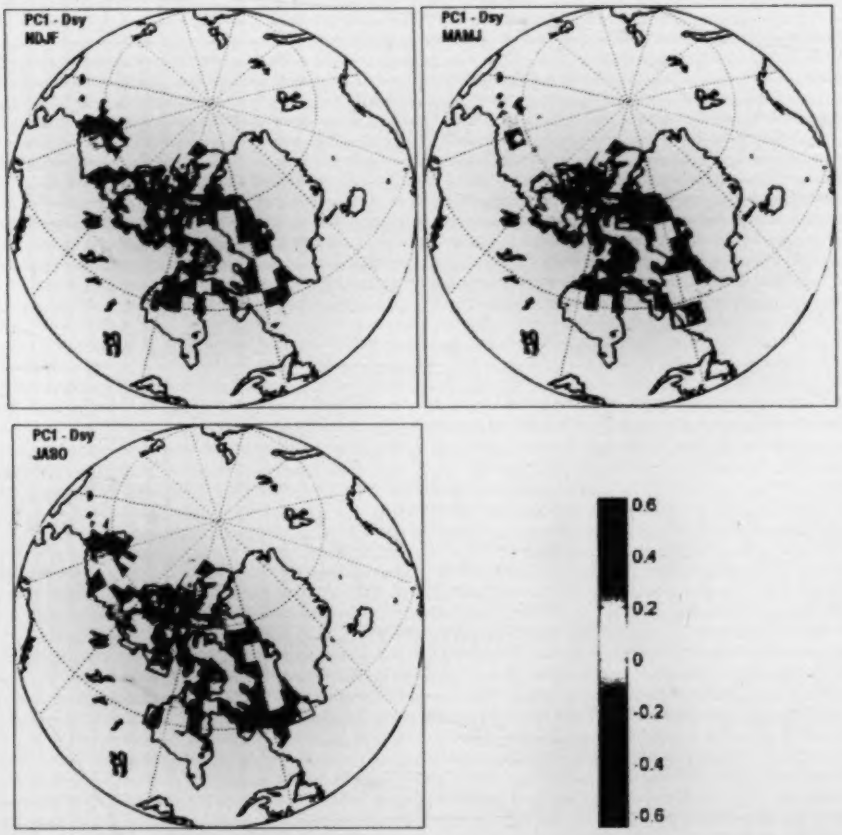

Figure 2-12 – The spatial distribution of correlations between net accumulation PC1 and the seasonal air mass densities (D_{SY}; Figure 3-7) in the winter (NDJF: **Top Left**), late-spring / early-summer (MAMJ: **Top Right**) and late-summer / early-fall (JASO: **Bottom Left**) seasons, during the 1979 to 2003 period. G814 grid cells with significant correlations ($p < 0.05$, $r > |0.42|$ and $df = 20$) are highlighted. Grey areas indicate $P_{MY} < 0.001$.

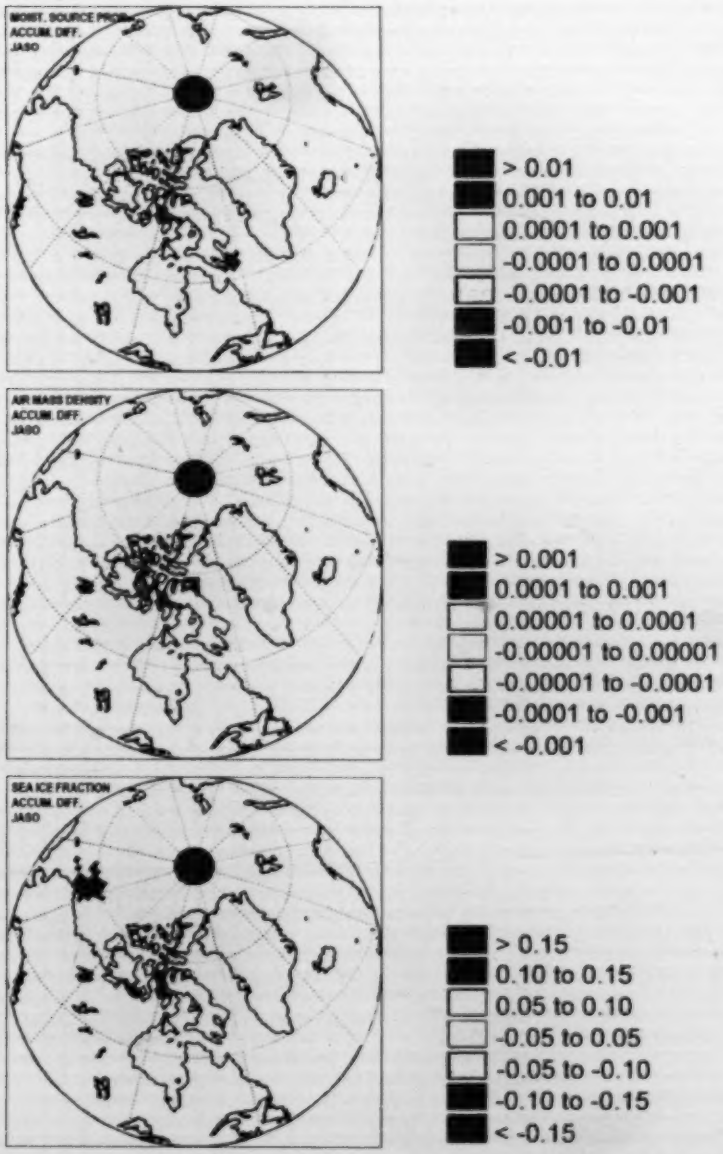

Figure 2-13 – A comparison of the period of significantly higher ($p < 0.05$; t-test) annual net accumulation (1979 to 1988) with the period of lower annual net accumulation (1989 to 2003; Figure 3-4) reveals significant differences ($p < 0.05$; t-test) in the mean seasonal moisture source probability (P_{SY}; **Top**), mean seasonal density of low elevation air masses en route to the Devon Island Ice Cap (D_{SX}; **Centre**) and mean seasonal sea ice fraction (S_{SY}; **Bottom**) in the late-summer / early-fall (JASO) season. Grey areas indicate $P_{MY} < 0.001$.

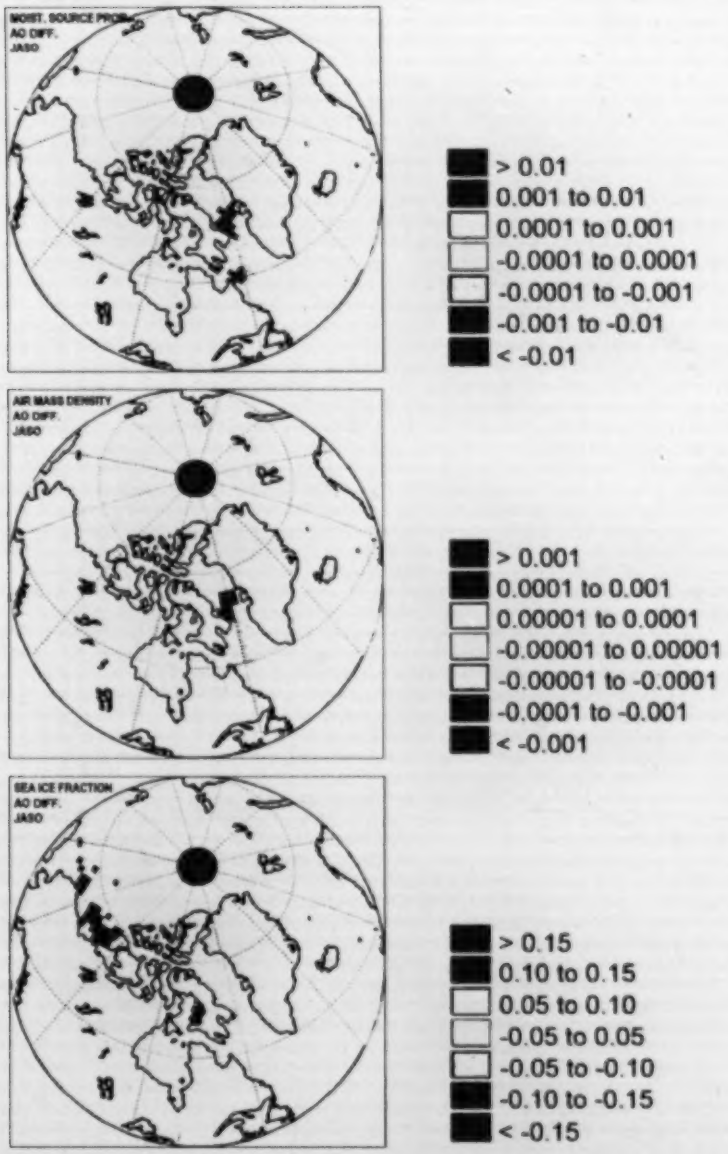

Figure 2-14 – A comparison of the three highest JASO Arctic Oscillation (AO) index years (1983, 1989 and 1994) with the three lowest JASO AO index years (1979, 1981 and 1993), during the 1979 to 2003 period, reveals significant differences ($p < 0.05$; t-test) in the mean seasonal moisture source probability (P_{SY}; **Top**), mean seasonal density of low elevation air masses en route to the Devon Island Ice Cap (D_{SX}; **Centre**) and mean seasonal sea ice fraction (S_{SY}; **Bottom**) in the late-summer / early-fall (JASO) season. Grey areas indicate $P_{MY} < 0.001$.

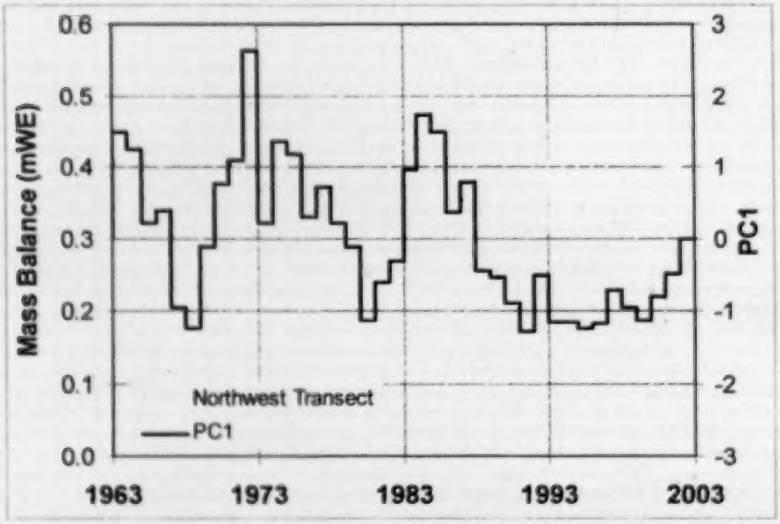

Figure 2-15 – The primary principal component (PC1) of the reconstructed annual net accumulation record, loading most strongly on the western cores A, B and C (Table 2-2), is significantly correlated ($p < 0.05$, $r = 0.45$ and $df = 35$) with the measured high elevation surface mass balance record (1250 m to 1750 m mean; Koerner, personal communication, 2005) of the northwest sector of the Devon Island Ice Cap over the period 1963 to 2003 (Figure 2-1). Thin lines indicate the measured mass balance error (~ 0.054 mWE a^{-1}; Koerner, 1970).

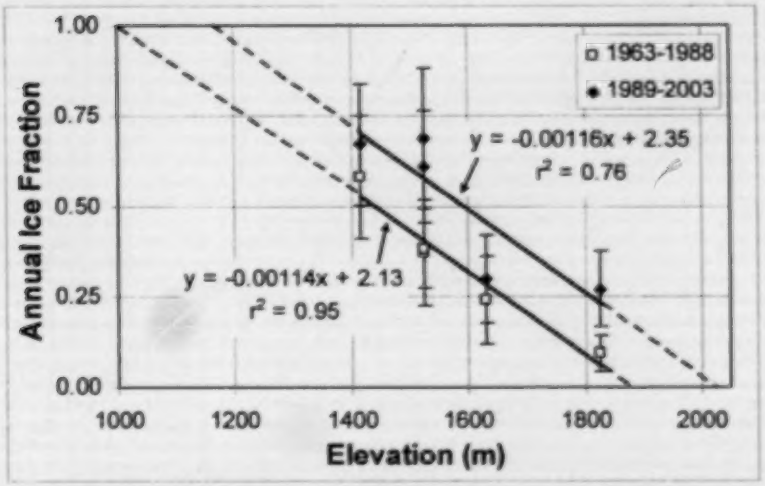

Figure 2-16 – Annual ice fraction-elevation relationship for the five shallow firn cores during the 1963 to 1988 and 1989 to 2003 periods. Vertical bars represent a half standard deviation in the annual ice fraction. The lower elevation limit of the dry snow zone (ice fraction = 0) and upper elevation limit of the superimposed ice zone (ice fraction = 1) are approximated through extrapolation of regressions during both periods.

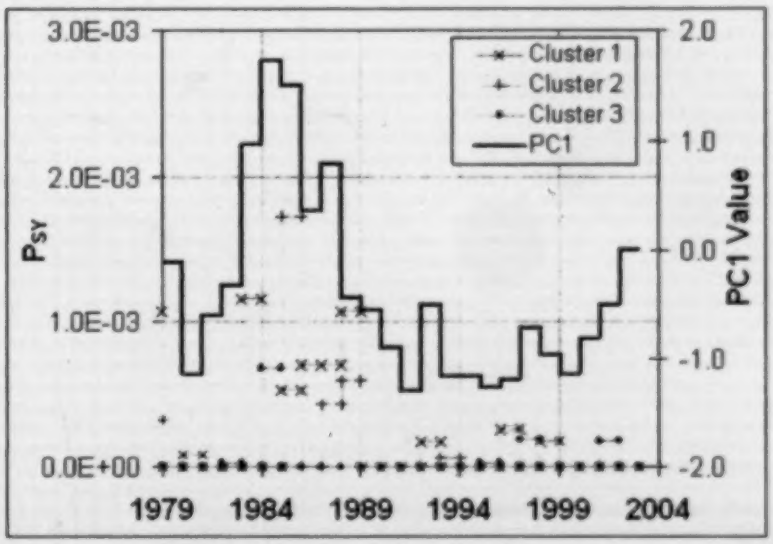

Figure 2-17 – The mean relative moisture source probability (P_{SY}) timeseries of each cluster identified in Figure 2-10, shown with PC1 during the 1979 to 2003 period. PC1 is significantly correlated with each cluster ($p < 0.05$ and $df = 20$).

Table 2-1 – Characteristics of the five shallow firn cores recovered from the Devon Island Ice Cap: location and elevation, the average number of melt days for the 2000 to 2004 period (Wang and others, 2005), the mean annual ice fraction (± standard deviation) and the mean annual net accumulation (± standard deviation).

	Core A	Core B	Core C	Core D	Core E
Latitude (°N)	75.3448	75.3427	75.3399	75.2390	75.4494
Longitude (°W)	83.7015	83.3525	82.6763	82.0310	82.5305
Elevation (m)	1415	1630	1825	1525	1525
Melt Days	31	24	18	27	29
Ice Fraction	0.615 ± 0.338	0.261 ± 0.243	0.158 ± 0.169	0.487 ± 0.360	0.459 ± 0.277
Net Accumulation (mWE)	0.221 ± 0.089	0.223 ± 0.070	0.246 ± 0.060	0.172 ± 0.055	0.230 ± 0.068

Table 2-2 – The variance explained and the loadings on each ice core of the first three principal components, only PC1 is significant according to Rule-N (Preisendorfer, 1988; Figure 2-5).

	PC1	PC2	PC3
Variance	39 %	22 %	21%
Core A	0.72	0.47	-0.23
Core B	0.77	-0.35	-0.01
Core C	0.77	-0.28	-0.25
Core D	0.24	-0.38	0.85
Core E	0.39	0.73	0.49

Chapter 3: Surface elevation changes in the high elevation region of the Devon Island Ice Cap, Nunavut, Canada *

(Co-authored by James A Davis)

3.1 – INTRODUCTION

Although the Devon Island Ice Cap has been losing mass at an estimated rate of 1.6 ± 0.7 km^{3}WE a^{-1} since 1960 (Burgess and Sharp, 2004), recent NASA laser altimetry surveys conducted in 1995 and 2000 found the high elevation region (> 1200 m) of the ice cap to be thickening, at a rate of up to 0.20 m a^{-1}, and the low elevation region (< 1200 m) to be thinning, at a rate of up to 0.40 m a^{-1} (Abdalati and others, 2004). These thickening and thinning trends have been extrapolated from relatively limited altimetry measurements along two flight lines (east-west and north-south), which intersect in the western high elevation region of the Devon Island Ice Cap, and are estimated to have an instrumental measurement accuracy of $\pm$ 0.02 m a^{-1} (Abdalati and others, 2004).

The high elevation region thickening was originally attributed to anomalously high snowfall during the survey period, based on 52-year meteorological station records (Abdalati and others, 2004). Recently however, shallow firn core reconstructions and an observed surface mass balance record have shown that the high elevation annual net accumulation rate was anomalously low, and the firnification rate anomalously high, during the 1995 to 2000 survey period, in comparison to the 1963 to 2003 mean (Chapter 2; Koerner, 2005). Anomalously high snowfall is therefore unlikely to be responsible for the observed thickening, unless the net accumulation rate during the 1995 to 2000 survey period is anomalously high in the context of an even longer term mean (>> 40 years). This may be possible if the ice outflow from the high elevation accumulation zone is still responding to an earlier period of lower mean net accumulation (Koerner, 2005).

The laser altimetry observations of the Devon Island Ice Cap are analogous to the findings of radar altimeter surveys of the Greenland Ice Sheet between 1992 and 2003,

* *A version of this paper has been submitted to the Journal of Glaciology as "Surface elevation changes in the high elevation region of the Devon Island Ice Cap, Nunavut, Canada." by W. Colgan, J. Davis and M. Sharp (07J042).*

which also show general low elevation thinning (< 1500 m; 0.020 ± 0.009 m a^{-1}) and high elevation thickening (> 1500 m; 0.064 ± 0.002 m a^{-1}; Johannessen and others, 2005). Repeat laser altimetry surveys of Greenland, performed using the same equipment as the NASA laser altimeter surveys of the Devon Island Ice Cap, also confirm this high elevation thickening and low elevation thinning trend (Krabill and others, 2004). Similar to recent studies of the Greenland Ice Sheet (Thomas and others, 1998; 2000), this paper performs an alternative calculation of the mean annual rate of thickness change of the high elevation region of the Devon Island Ice Cap, by comparing the mean annual net accumulation rates to the mean specific outflow rates from individual flux basins. A decrease in the rate of specific outflow from high to low elevation regions, relative to the net accumulation rate, could explain the observed concurrent high elevation thickening and low elevation thinning of the Devon Island Ice Cap. The objectives of this paper are to (i) calculate flux basin-scale rates of thickness change across the high elevation region of the Devon Island Ice Cap, (ii) provide an indication of how representative the laser altimetry observations are of the high elevation region, and (iii) assess whether there has been a change in ice outflow from the high elevation region of the Devon Island Ice Cap.

Long term changes in ice dynamics are of great interest, as the net transfer of land-based ice into the oceans is the second greatest contributor to contemporary sea level rise (Raper and Braithwaite, 2002; 2006). The primary cause of sea level rise is the thermal expansion of sea water (Raper and Braithwaite, 2002; 2006). The Canadian Arctic ice caps contain the largest area of glaciated terrain in the world outside Greenland and Antarctica (Dyurgerov and Meier, 2005). Although the potential sea level rise from these ice caps is far less than that from Greenland or Antarctica, their more temperate environs and shorter response time makes them potentially more reactive to changes in climate (Raper and Braithwaite, 2006). Between 2001 and 2004 the ice caps and alpine glaciers external to Greenland and Antarctica contributed approximately 0.77 ± 0.15 mm a^{-1} to sea level rise (Kaser and others, 2006). Recent models suggest that these glaciers will contribute between 46 and 51 mm of sea level rise by the year 2100 (Raper and Braithwaite, 2006). The Devon Island Ice Cap (75 °N, 82 °W) is the sixth largest ice cap in the Arctic, with an estimated volume of 3980 km^3, equivalent to approximately 10 mm of sea level rise if melted completely (Figure 3-1; Dowdeswell and others, 2004). The

Devon Island Ice Cap is currently estimated to be contributing between 0.036 and 0.046 mm a^{-1} to sea level rise (Burgess and Sharp, 2004; Abdalati and others, 2004).

3.2 – METHODS

3.2.1 – Surface flow velocities

The specific ice outflow from the high elevation region of the Devon Island Ice Cap was calculated based on measured surface ice velocities and previously published ice thickness data (Dowdeswell and others, 2004). Seventeen 4 m wooden stakes were installed approximately along the 1200 m contour of the Devon Island Ice Cap in April 2005. Ten of these stakes remained the following year for a second survey in April 2006. Static differential GPS methods were used to determine stake locations, using Leica Geosystems series 500 dual frequency GPS units, which detected between 8 and 11 American NAVSTAR satellites at any given time. Multiple base station locations were used in each field season to ensure a distance of less than 25 km between the base station and stake positions during each survey. Rover sampling times were between 10 and 90 min, depending on distances between the rover and base stations. Data were processed in Leica Geo Office (version 1.0) and achieved phase position solutions accurate to better than ± 0.5 cm in the horizontal (x, y) and ± 2.0 cm in the vertical (z).

As the height of the snow surface at a given location is variable between years, GPS measurements were corrected to reflect the base-of-stake location, rather than snow surface location, of each stake. This ensured that proper year-to-year comparisons were made. At each survey point, the GPS antenna was mounted on top of the stake, and the length of the stake (3 m) was subtracted from the vertical co-ordinate of the GPS measurement to yield a base-of-stake position. Therefore, at stakes with no tilt between surveys the positional uncertainty should be equivalent to instrument uncertainty (z: ± 2.0 cm; x and y: ± 0.5 cm). Two stakes, however, became tilted between the two surveys (6: 10 ° and 17: 20 °). For these two stakes, the GPS antenna was mounted on a survey tripod centred over the point where the stake protruded from the snow surface and trigonometry was used to estimate the base-of-stake position. For these two stakes, the total positional error was conservatively estimated as 25 % of the trigonometrically-corrected horizontal distance in the x and y coordinates (± 8.8 and 2.8 cm respectively) and 10 % of the

trigonometrically-corrected vertical distance in the z coordinate (± 6.2 and 9.6 cm respectively). The difference in stake positions between surveys was used to resolve the azimuth and magnitude of horizontal stake displacements. These vectors were then divided by the length of time between surveys at each stake to determine stake velocities.

To supplement the paucity of repeat GPS measurements in the eastern portion of the high elevation region, due to stake loss between surveys, 1 'dummy' velocity point was included with the 10 measured stake velocities and then treated in a similar manner. The dummy point velocity was derived from interferometric synthetic aperture radar (InSAR) using winter-spring 1996 ERS-1/2 satellite imagery (Burgess and others, 2005). At the 7 locations for which the necessary data were available, a regression of measured stake velocities against InSAR-derived velocities yielded a slope of 1.04 and an r^2 of 0.72, with a standard error of the estimate of 3.7 m a^{-1} (Figure 3-2). The difference between InSAR-derived and measured stake velocities is not uniform across the study site.

The InSAR-derived velocities lack true 3D resolution, as they were derived using only ascending orbit data, and were produced by resolving the look direction velocities onto the calculated direction of steepest down-glacier slope (Burgess and others, 2005). As a result, the uncertainty in InSAR-derived velocities increases with (i) increasing angle between the ice flow direction and the look direction of the satellite (β; expressed in °), and (ii) decreasing surface slope. Variability in the difference between measured and InSAR-derived velocities was found to be partly explained by variability in surface slope at all stake sites ($r^2 = 0.51$; Figure 3-2). Variability in β values only partly explains InSAR versus stake-derived velocity differences at stake sites other than stake 16 ($r^2 = 0.53$; Figure 3-2). At stake 16, a relatively high surface slope appears to have overcome the effects of a high β value (Table 3-1). The combined effect of β value and slope (taken as the quotient of β over slope) accounts for approximately 41 % of the difference between the measured and InSAR-derived velocities at all stake sites ($r^2 = 0.41$; Figure 3-2). The remaining 59 % of the variability between measured and InSAR velocities may result from either differences in the length of the measurement periods or represent true changes in surface velocity between the 1996 InSAR observations and the 2005 to 2006 velocity measurements.

InSAR-derived surface ice flow velocities are greater than the measured velocities at 5 of the 7 stakes (stakes 4, 5, 11, 16 and 17; Figure 3-2). As the InSAR-derived velocities are produced using winter-spring ERS imagery, they are expected to approximate the annual minimum surface ice flow velocities. By comparison, the stakes were surveyed over a 12-month period, and therefore more accurately reflect annual mean surface ice flow velocities. Annual surface ice flow velocities would be expected to be greater than winter-spring minimum surface ice flow velocities. Although the most likely explanation for this discrepancy is that surface velocities were higher during the period of InSAR observations, this dataset is insufficient to provide convincing evidence of a general decrease in high elevation surface ice flow velocity since 1996. These data do, however, emphasize the importance of field measurements to interpret remotely sensed surface ice velocity fields.

3.2.2 – Delineating flux basins

The rates of specific outflow and net accumulation were calculated for 11 flux basins within the high elevation region study area. The 1 dummy and 10 measured stakes were used to define 11 flux gates and their corresponding flux basins. Stake 12 was not used to delineate a flux basin due to its short distance from stake 11 (Figure 3-2; Table 3-1). The relatively high attrition rate of the wooden stakes, likely due to a combination of icing and wind, resulted in uneven flux gate sizes. Flux basins were delineated using a 1 km digital elevation model (DEM) of the Devon Island Ice Cap (Dowdeswell and others, 2004). Flow lines leading from the main drainage divide to the stakes were used to define the lateral boundaries of the flux basins (Thomas and others, 1998), using the flow direction tool in ArcGIS 9.0. The flow direction tool was applied to the DEM surface slope field to produce a flow direction field. Manual, rather than algorithm, flow lines were then extracted from the flow direction field (Le Brocq and others, 2006). Once the flow direction in each 1 km DEM cell was known, the up slope source cell of a given DEM cell could be identified. An up slope source cell is defined as a cell that flows into a given DEM cell. To produce a flow line for each stake, successive up slope source cells were traced from the cell containing the stake back to the main drainage divide of the ice cap (Figure 3-3).

To optimize flow line resolution, each DEM cell was recognized to have eight neighbours, each of which was evaluated as a potential upslope source cell (Le Brocq and others, 2006). When a cell was found to have two possible up slope source cells, repeat flow line traces were performed using both possible routes. Through multiple repeat flow line traces originating from each stake, we estimate an uncertainty of 10 % in the area of a given flux basin ($\sigma[A_B]$; expressed in m^2). Perimeter grid cells could be split diagonally by flow lines, but subsequent net accumulation and outflow calculations were performed using area-averaging techniques to ensure that the mean net accumulation or outflow value of a basin was properly weighted by the area of all full and partial cells within a given flux basin (Le Brocq and others, 2006).

3.2.3 – Determining annual rate of specific outflow

For each flux basin, the difference between the mean annual specific outflow through the flux gate and the mean annual net accumulation averaged over the upstream flux basin was taken as an estimate of the rate of thickness change (dh/dt; expressed in mWE a^{-1}). To determine the volumetric outflow from a given flux basin, the cross sectional area of the flux gate was derived from previously published ice thickness observations (Dowdeswell and others, 2004), and the horizontally and vertically-averaged ice velocities through the flux gate were derived from the one-year repeat GPS surveys. Dividing the calculated outflow by the area of the upstream flux basin produces an estimate of the mean annual rate of specific outflow (dh_O/dt; expressed in mWE a^{-1}), which is directly comparable with the mean annual net accumulation rate (dh_A/dt; expressed in mWE a^{-1}). The calculated annual rate of specific outflow is assumed to represent the mean annual specific outflow during the period 1963 to 2003, the interval for which mean annual net accumulation measurements are available from shallow firn cores.

The surface velocity (u_{TG}; expressed in m a^{-1}) of a given stake ($_T$) in the direction perpendicular to a given flux gate ($_G$) was calculated according to:

$$u_{TG} = u_T \times \cos \alpha_{TG} \qquad \text{Equation 3-1}$$

where u_T is the measured surface velocity of a given stake, expressed in m a^{-1}; and α_{TG} is the angle between the direction of movement of a given stake and the direction

perpendicular to a given flux gate expressed in degrees (°). The horizontally averaged surface velocity perpendicular to a given flux gate (u_G; expressed in m a^{-1}) was calculated according to:

$$u_G = \frac{(u_{TG1} + u_{TG2})}{2} \qquad \text{Equation 3-2}$$

where u_{TG1} and u_{TG2} are the gate-perpendicular velocities of the stakes at either side of a given flux gate. Assuming laminar flow, the vertically averaged ice outflow velocity through a given flux gate ($\overline{u_G}$; expressed in m a^{-1}) was calculated according to:

$$\overline{u_G} = \frac{(n+1)}{(n+2)} \times u_G \qquad \text{Equation 3-3}$$

where n is the dimensionless Glen's Flow Law parameter (Paterson, 2002). A value of $n = 3$ was used, following the findings of a modeling study of flow in the summit region of the Devon Island Ice Cap (Reeh and Paterson, 1988). The cross-sectional area of each gate (A_G; expressed in m^2) was calculated according to:

$$A_G = d_G \times \overline{h_G} \qquad \text{Equation 3-4}$$

where d_G is the distance between the two stakes that form a given flux gate, expressed in m; and $\overline{h_G}$ is the mean ice thickness across a given flux gate, expressed in m (Table 3-2). The mean ice thickness was derived from ice thicknesses interpolated at 1 km intervals across the gate (Dowdeswell and others, 2004). The annual volumetric outflow of ice (V_B; expressed in m^3 a^{-1}) from a given flux basin was calculated as:

$$V_B = \overline{u_G} \times A_G \qquad \text{Equation 3-5}$$

To facilitate comparison with measurements of net accumulation rate in the basin upstream from the flux gate, the volumetric outflow was converted into a rate of specific outflow, equivalent to a surface elevation change in each basin (dh_O/dt; expressed in mWE a^{-1}) according to:

$$\frac{dh_O}{dt} = \left(\frac{V_B}{A_B}\right) \cdot \left(\frac{\rho_I}{\rho_W}\right) \qquad \text{Equation 3-6}$$

where ρ_I is the density of ice, assumed to be 900 kg m^{-3}; ρ_W is the density of water, assumed to be 1000 kg m^{-3}; and A_B is the area of a given flux basin, expressed in m^2 (Figure 3-3).

3.2.4 – Determining annual net accumulation rate

The mean annual change in surface elevation due to net accumulation over the 1963 to 2003 period (dh_A/dt; expressed in mWE a^{-1}) was determined for each flux basin based on net accumulation rates previously determined at 13 shallow firn core sites (Chapter 2; Mair and others, 2005). The mean annual net accumulation rate at each of the 13 shallow firn core sites was calculated by dividing the water equivalent (WE) depth of the 1963 ^{137}Cs 'bomb' layer by the number of years between 1963 and the year the core was recovered (Chapter 2; Mair and others, 2005). The bomb layer is the result of fallout from atmospheric thermonuclear weapons testing (Dunphy and Dibb, 1994). Multiple linear regression (MLR; van der Veen and others, 2001) produced the following relationship between net accumulation and elevation and latitude at each core site:

$$\frac{dh_A}{dt} = 1.09 \cdot 10^{-4} Z - 2.46 \cdot 10^{-6} Y + 20.6 \qquad \text{Equation 3-7}$$

where Z is the elevation (m) and Y is the UTM northing (m; $p < 0.01$, adjusted $r = 0.73$ and $df = 13$; Figure 3-4). The standard error of the regression estimate is 0.023 mWE a^{-1}, with residuals of between |0.003| and |0.067| mWE a^{-1}, distributed randomly across the high elevation region (Table 3-3). The inclusion of longitude as an additional predictor variable did not improve the adjusted r^2 (0.54), so longitude was excluded from the MLR (van der Veen and others, 2001). Equation 3-7 was used to estimate the mean annual net accumulation rate in each 1 km DEM cell within the high elevation region (van der Veen and others, 2001). An area-averaged mean of the MLR-derived net accumulation rates of the grid cells within a given flux basin was taken to represent the mean annual net accumulation rate in that flux basin (Figure 3-3).

3.2.5 – Determining annual rate of thickness change

As the annual specific outflow rate (Equation 3-6) is assumed to be directly comparable with the mean annual net accumulation rate (Equation 3-7) the annual rate of

thickness change (dh/dt; expressed in mWE a^{-1}) of a given flux basin was calculated as (Figure 3-3):

$$\frac{dh}{dt} = \left(\frac{dh_A}{dt}\right) + \left(\frac{dh_O}{dt}\right) \qquad \text{Equation 3-8}$$

3.2.6 – Error analysis

Traditional error analysis was used to quantify the uncertainty associated with the calculated rates of specific outflow, net accumulation and thickness change. The largest sources of uncertainty in computing the rate of specific outflow for a given flux basin reside in the calculation of the horizontally and vertically averaged outflow velocities. Uncertainty in the vertically-averaged velocity profile due to the choice of n ($\sigma_V[\overline{u_G}]$; expressed in m a^{-1}) was assessed as the difference in vertically-averaged velocities determined assuming $n = 2$ and $n = 4$ for a given flux gate. Although the true value of n for the high elevation region of the Devon Island Ice Cap is likely close to 3 (Reeh and Paterson, 1988), calculating the vertically averaged velocity using a range of n values accommodates a wide spectrum of potential vertical velocity profiles. The spectrum of vertical velocity profiles ranges from the majority of movement occurring via basal sliding ($n = 4$) to the majority of movement occurring via internal ice deformation ($n = 2$). The uncertainty in the vertically averaged velocity profile can therefore be calculated from a simplification of Equation 3-3 (Table 3-4):

$$\sigma_V[\overline{u_G}] = \left(\frac{1}{12}\right) \cdot u_G \qquad \text{Equation 3-9}$$

Uncertainty in the horizontally-averaged velocity ($\sigma_H[u_G]$; expressed in m a^{-1}) is associated with the accuracy with which the two stakes in a given flux gate represent the 'true' horizontal surface velocity profile perpendicular to the gate. To assess the magnitude of uncertainty in the horizontally-averaged velocity, along-gate profiles of InSAR-derived surface velocity (Burgess and others, 2005) were compared with the two-stake surface velocity profiles inferred from stake azimuth velocities at either side of a given gate. Near-complete (> 80 %) InSAR-derived surface velocity profiles were available for only four gates (1, 6, 9 and 10; Table 3-4). The InSAR-derived surface velocity profiles across these 4 gates were linearly detrended and re-expressed as

deviations from the two-point stake profile (Figure 3-5). The standard error in the re-expressed InSAR profile was taken to represent the uncertainty in the horizontally averaged velocity across the four respective flux gates (Table 3-4). Although the InSAR-derived dummy velocity point on its eastern margin delineates Gate 6 and constrains the two along-gate surface velocity profiles to be equal at one side, the comparison is still useful to examine how well a two-point profile captures the range of surface velocities across the gate.

The comparison between InSAR-derived along-gate surface velocity profiles and two-point stake profiles demonstrated the presence of significant variability in surface flow velocity across all 4 flux gates, which is poorly captured by the two-point linear profile. A comparison of the surface velocities through flux gate 1 measured by InSAR (sampled at 1 km intervals) and the surface velocities estimated by the two-point linear profile, yielded a standard error of 1.6 m a^{-1}. The standard error is defined as the standard deviation of the differences between the InSAR-derived velocities and those estimated by the linear two-point profile at 1 km intervals across the flux gate. This is taken as an estimate of the uncertainty in using the two-point linear profile to represent the 'true' velocity profile, which is assumed to be reflected in the InSAR-derived profile (Table 3-4). An increasing departure between the two profiles towards the south is likely an artifact of an increasing angle between the satellite look and ice flow directions (Figure 3-5). A higher standard error across flux gate 9 (2.5 m a^{-1}) indicates that the two-point stake profile is a weaker fit to the InSAR-derived profile (Figure 3-5). The standard errors across flux gates 6 and 10 are higher, 6.6 and 13.3 m a^{-1} respectively, as the InSAR-derived velocity profiles show the existence of regions of substantially higher velocity, which are not captured by the two-point stake profiles (Figure 3-5). As variability in the surface velocity profile is expected to increase with the width of the flux gate, estimates of the uncertainty in the horizontally-averaged velocity of the remaining 7 flux gates were produced using a regression ($p < 0.05$, $r = 0.87$ and $df = 4$) of the uncertainty in the horizontally-averaged velocity against flux gate width from the 4 flux gates for which data were available (Figure 3-6; Table 3-4).

Assuming that the errors in both the horizontally and vertically-averaged velocities are independent and random, the total error in average velocity through a given

flux gate ($\sigma[\overline{u_G}]$; expressed in m a^{-1}) can be estimated as the quadratic sum of the fractional uncertainties in both terms (Thomas and others, 1998):

$$\sigma[\overline{u_G}] = \sqrt{(\sigma_H[u_G])^2 + (\sigma_v[\overline{u_G}])^2} \qquad \text{Equation 3-10}$$

Likewise, assuming that the errors in each term used to compute specific outflow are independent and random, the error in the mean annual change in surface elevation due to specific outflow from a given flux basin ($\sigma[dh_O/dt]$; expressed in mWE a^{-1}; Table 3-5) can be estimated as (Thomas and others, 1998):

$$\sigma\left[\frac{dh_O}{dt}\right] = \sqrt{\left(\frac{\sigma[A_B]}{A_B}\right)^2 + \left(\frac{\sigma[d_G]}{d_G}\right)^2 + \left(\frac{\sigma[\overline{u_G}]}{\overline{u_G}}\right)^2 + \left(\frac{\sigma[\overline{h_G}]}{h_G}\right)^2 + \left(\frac{\sigma[\rho_I]}{\rho_I}\right)^2} \cdot \left(\frac{dh_O}{dt}\right) \qquad \text{Eq. 3-11}$$

where $\sigma[A_B]$ is the uncertainty in flux basin area, assessed as 10 % of A_B through repeat flow line traces; $\sigma[d_G]$ is the horizontal positional error of ± 0.005 m for all stakes except for 6 and 17 (for which the errors are ± 0.088 and 0.028 m respectively); $\sigma[\overline{u_G}]$ is calculated according to Equation 3-10 for a given flux gate; $\sigma[\overline{h_G}]$ is an assumed ice thickness error of ± 10 m (Dowdeswell and others, 2004); and $\sigma[\rho_I]$ is an assumed density uncertainty of ± 50 kg m^{-3}.

Two sources of uncertainty arise in the computation of the rate of surface elevation change due to net accumulation for a given flux basin: (i) the uncertainty associated with the calculation of the mean annual net accumulation rate at each core site, and (ii) the uncertainty introduced by the use of MLR to interpolate the net accumulation rates of the 13 core sites throughout the high elevation region. The uncertainty in the mean annual net accumulation rate ($\sigma[a_c]$; expressed in mWE a^{-1}) is assumed to be the quotient of the uncertainty in the water equivalent depth of the 1963 ^{137}Cs horizon (± 0.1 mWE) over 40 years (± 0.0025 mWE a^{-1}). As the differences between observed and MLR-interpolated net accumulation rates at the 13 core sites appear to be randomly distributed throughout the high elevation region (Table 3-3), the uncertainty in the use of MLR to interpolate net accumulation rates ($\sigma[a_m]$; expressed in mWE a^{-1}) was taken as the standard error of the MLR regression estimate (0.023 mWE a^{-1}; Figure 3-4). The uncertainty in the mean annual change in surface elevation due to net accumulation

($\sigma[\dot{h}_A/dt]$; expressed in mWE a^{-1}; Table 3-5) was estimated for all flux basins according to (Thomas and others, 1998):

$$\sigma\left[\frac{d\dot{h}_A}{dt}\right] = \sqrt{(\sigma[a_c])^2 + (\sigma[a_m])^2} \qquad \text{Equation 3-12}$$

Therefore, assuming that the errors in both of the terms used to arrive at the calculated rate of thickness change (Equation 3-8) are independent and random, the error in the mean annual change in surface elevation in a given flux basin ($\sigma[\dot{h}/dt]$; expressed in mWE a^{-1}; Table 3-5) can be estimated as the quadratic sum of the fractional uncertainties in the mean annual change in surface elevation due to both specific outflow and net accumulation (Thomas and others, 1998):

$$\sigma\left[\frac{d\dot{h}}{dt}\right] = \sqrt{\left(\sigma\left[\frac{d\dot{h}_O}{dt}\right]\right)^2 + \left(\sigma\left[\frac{d\dot{h}_A}{dt}\right]\right)^2} \qquad \text{Equation 3-13}$$

3.3 – RESULTS

3.3.1 – Annual flux basin thickness change

There is a clear contrast between the rates of specific outflow, net accumulation and thickness change of flux basins south of the main east-west drainage divide (basins 7, 8, 9, 10 and 11; hereafter: southern basins) and the flux basins north of the main drainage divide (basins 1, 2, 3, 4, 5 and 6; hereafter: northern basins). A two-tailed t-test, assuming equal variance, reveals that the annual specific outflow rates of the southern basins (area-average: -0.251 ± 0.175 mWE a^{-1}) are significantly ($p < 0.01$) greater than those from the northern basins (area-average: -0.121 ± 0.132 mWE a^{-1}; Figure 3-3). Variation in specific outflow rates appears to be largely attributable to variation in the depth-averaged velocity (Figure 3-7). Likewise, the uncertainty in the specific outflow term is dominated by the uncertainty in the depth-averaged velocity across each flux gate, which in turn appears to be more dependent on variation in the horizontally averaged velocity than in the vertically averaged velocity (Table 3-4). InSAR-derived velocities range from 67% (stake 15: 2.9 versus 4.3 m a^{-1}) to 260 % (stake 17: 13.2 versus 4.9 m a^{-1}; Figure 3-2) of the measured stake velocities. InSAR-derived velocities average 128 ± 66 % of the measured stake velocities. As specific outflows calculated using InSAR-derived velocities should therefore be greater than those calculated using measured velocities, estimates of rates of

thickness change based on InSAR-derived specific outflows should be lower than estimates based on specific outflows computed from stake measurements.

A two-tailed t-test, assuming equal variance, reveals that the annual net accumulation rates of the southern basins (area-average: 0.222 ± 0.023 mWE a^{-1}) are significantly ($p < 0.001$) greater than the annual net accumulation rates of the northern basins (area-average: 0.176 ± 0.023 mWE a^{-1}; Figure 3-5). MLR suggests that variation in net accumulation rate is primarily explained by latitude (UTM northing) rather than elevation, leading to a strong north-south net accumulation gradient across the study region (Figure 3-3). The uncertainty in net accumulation rate is uniform across the flux basins due to the fixed uncertainties in the calculation of the annual net accumulation rate at each shallow firn core site, and the assumed random distribution of MLR residuals (Table 3-3).

A two-tailed t-test, assuming equal variance, reveals that the thickness change rates of the northern basins (area-averaged: 0.054 ± 0.137 mWE a^{-1}) are significantly ($p < 0.05$) greater than those of the southern basins (area-averaged: -0.029 ± 0.165 mWE a^{-1}), four of which are experiencing net thinning (Figure 3-3). Across all the flux basins in the high elevation region of the Devon Island Ice Cap, the area-averaged mean annual rate of thickness change was found to be 0.009 mWE a^{-1}, which is well within the estimated margin of uncertainty (± 0.152 mWE a^{-1}; Table 3-5). The rate of thickness change of a given flux basin appears to be more dependent on its rate of specific outflow, than its net accumulation rate (Figure 3-7). Accordingly, variation in the uncertainty of the rate of thickness change is driven largely by variation in the uncertainty of specific outflow rates, rather than by the uniform uncertainty associated with the net accumulation rate (Table 3-5).

3.4 – DISCUSSION

3.4.1 – Level of uncertainty

The area-averaged rate of thickness change across all the flux basins in the high elevation region of the Devon Island Ice Cap (0.009 mWE a^{-1}) is 17 times smaller than the uncertainty associated with its calculation (± 0.152 mWE a^{-1}). Although the calculated rates of thickness change exceed their associated uncertainty in 4 flux basins

(3, 4, 9 and 11), in 7 basins the estimated rates of thickness change are less than the associated uncertainty. We would expect the methods employed in this study to confidently resolve rates of thickness change greater than approximately |0.2| mWE a^{-1} at the basin level. Similarly, the observation that the northern basins are thickening approximately twice as fast as the southern basins are thinning is within the associated uncertainty.

Uncertainties in the horizontally and vertically-averaged velocity profiles are the main source of uncertainty in the calculated rates of thickness change. Although remotely sensed surface velocity fields can potentially improve horizontally-averaged across gate surface velocity profiles, this study has found that InSAR-derived velocities which lack true 3D resolution are susceptible to the influences of (i) the angle between the directions of satellite look and ice flow and (ii) surface slope, and that they over-estimate surface flow velocities by 1.8 m a^{-1} on average (Figure 3-2). This highlights the need for increased in situ surface velocity stake measurements, or the development of an InSAR-derived surface velocity field produced using both ascending and descending orbits, to refine outflow calculations for the high elevation region of the Devon Island Ice Cap.

3.4.2 – Flow regimes

Based on the ratio of ice velocity to ice thickness and driving stress, four flow regimes were delineated within the Devon Island Ice Cap by Burgess and others (2005). These flow regimes differentiate regions of differing flow resistance. Measured stake velocities are largely determined by the local flow regime at each stake site. Flow regime 1 is inferred to represent flow primarily by internal deformation, flow regime 2 basal sliding, flow regime 3 enhanced basal sliding at low driving stress and flow regime 4 flow by basal sediment deformation. The high elevation area investigated in this study is dominated by flow regime 1, with minor local areas of flow regime 2. Flow regimes 3 and 4 tend to be found at lower elevations (Figure 3-8). Flow regime 1 is characterized by relatively low surface velocities and low driving stress, creating a convex-up surface profile and an environment where ice flows mainly through internal deformation, as the ice is likely frozen to the bed (Burgess and others, 2005). Flow regime 2 appears when flow becomes channelled by bedrock topography and results in increased surface

velocities, creating a concave-up surface profile and an environment where ice flows through basal sliding as well as, or instead of, internal deformation (Burgess and others, 2005).

Although the majority of the high elevation area is characterised by flow regime 1, there are areas of flow regime 2 near the 1200 m contour. The comparison between the InSAR-derived and two-point measured along gate surface velocity profiles provides evidence that the flux gates are influenced by flow regime 2 (Figures 3-5 and 3-8). Flux gates which straddle both flow regimes 1 and 2 are undesirable, as the two-point horizontally averaged velocity profile has been shown to be a poor approximation for gates with both flow regimes (Figure 3-5). As the vertical velocity profiles of flow regimes 1 and 2 are inherently different, a generous uncertainty was assigned to the vertically averaged velocities to account for the likely scenario that both flow regimes 1 and 2 are represented within a given flux gate (Equation 3-9). Likewise, it was conservatively assumed that uncertainty in the horizontal velocity profile always increases with flux gate width (Figure 3-6).

These generous uncertainties are likely reflective of the 'true' uncertainty associated with the rate of thickness change estimates in the eastern basins (6, 7 and 11), where both flow regimes are evident across the flux gates (Figure 3-10). These uncertainties however, may be an over-estimate of the 'true' uncertainty associated with the rate of thickness change in the west (basins 1, 2, 3 and 10), where flow regime 1 extends from the main drainage divide to near the ice cap margin (Burgess and others, 2005). In the west, the straddling of flow regimes 1 and 2 by flux gates is likely minimal. The western horizontal and vertical velocity profiles are therefore likely to be simpler and more uniform than those in the east. As a result of this, the western flux gates are more likely to be more accurately described by the first-order outflow calculations used in this paper than the eastern flux gates (Figure 3-8).

Future studies could further reduce specific outflow uncertainties by (i) decreasing flux gate widths, to minimize the sampling of both flow regimes 1 and 2 by flux gates, (ii) assessing vertical and horizontal velocity profile assumptions and uncertainties at each gate independently, or (iii) moving the flux gates upstream to a higher elevation, above the heads of the flow regime 2 threads.

3.4.3 – A comparison with remotely sensed estimates

Laser altimetry observations of the high elevation region suggest a maximum rate of thickening of 0.20 m a^{-1}, with a mean rate of thickening of approximately 0.05 m a^{-1} (Abdalati and others, 2004). Although an instrumental error of 0.02 m a^{-1} was assigned to these laser altimetry observations, it is not possible to determine an area-averaged high elevation thickening value or its associated uncertainty from the available information (Abdalati and others, 2004). Our results corroborate a high elevation thickening trend. To make the conclusions comparable, the laser altimetry measurements were converted from an absolute thickening rate (m a^{-1}) to a WE thickening rate (mWE a^{-1}). WE conversions were performed based on two distinct density scenarios: (i) close to ice (850 kg m^{-3}), if the observed elevation changes are the result of decreased ice outflow from the high elevation region, as suggested by a recent decrease in the annual net accumulation rate and an increase in the rate of firnification (Chapter 2), and (ii) fresh snow (300 kg m^{-3}), if the observed changes are the result of differences in the spring snow pack between survey years (Abdalati and others, 2004). These two density scenarios correspond to an approximate mean rate of thickness change within the high elevation region of between 0.015 and 0.043 mWE a^{-1}. This is between 2 and 5 times greater than area-averaged rate calculated in this study (0.009 ± 0.152 mWE a^{-1}).

The high elevation thickness changes observed by laser altimetry range between approximately -0.15 and +0.20 m a^{-1}. The majority of observations lie between zero and 0.10 m a^{-1} (Abdalati and others, 2004). Only approximately 10 % of the high elevation region laser altimetry observations suggest thinning, and no well-defined high elevation region of thinning is identified by Abdalati and others (2004). There are no laser altimetry observations over the flux basins in which we find thinning (Figure 3-3). The majority of the high elevation region laser altimetry observations suggest thickening, with the east-west flight line showing more rapid thickening than the north-south flight line (Abdalati and others, 2004). These two flight lines provide only partial coverage of the Devon Island Ice Cap (Figure 3-3). As the laser altimetry measurements over the eastern portion of the high elevation region were limited by cloud cover, and the north-south flight line was flown west of the main north-south drainage divide of the ice cap, the laser altimetry

observations are biased towards the western portion of the high elevation region (Abdalati and others, 2004). In the western portion of the high elevation region (basins 1, 2, 3 and 4), our calculations suggest thickening in all four flux basins (between 0.010 and 0.132 mWE a^{-1}; Table 3-5). In the eastern portion of the high elevation region (basins 5, 6, 7, 8 and 11), where laser altimetry observations were limited, we find no general thickening or thinning trend, with two basins thickening (0.040 and 0.055 mWE a^{-1}), two basins thinning (-0.030 and -0.237 mWE a^{-1}) and one in approximate equilibrium (~0 mWE a^{-1}; Table 3-5). As differences in the spatial distribution of thickening observations can be expected to result in differences in the "observed" thickening, increased laser altimetry observations in the eastern portion of the high elevation region, where our calculations suggest a rate of thickness change close to or below zero, would likely have resulted in lower estimate of the rate of thickening by Abdalati and others (2004), closer to the rate of thickening found in this thesis.

3.4.4 – Ice dynamics

Over short survey periods, laser altimeter measurements of elevation change can be heavily influenced by inter-annual variability in the snow surface where the laser is reflected (Thomas and others, 2001). The laser-altimetry observations of high elevation thickening of the Devon Island Ice Cap are unlikely to reflect anomalously high net accumulation between 1995 and 2000, as both the 1961 to 2003 measured surface mass balance record and the 1963 to 2003 reconstructed net accumulation record suggest anomalously low net accumulation during this period (Chapter 2; Koerner, 2005). It is also unlikely that a change in the rate of firnification can explain the laser altimetry observations, as the ice content in shallow firn cores recovered from the high elevation region of the Devon Island Ice Cap increased between 1989 and 2003, relative to the 1963 to 1988 mean (Chapter 2; Thomas and others, 2001). We speculate that the laser-altimetry observations capture a longer-term trend in ice dynamics. As changes in ice flow dynamics have recently been detected at the 40-year scale on the larger Greenland Ice Sheet, it is quite possible that ice flow dynamic changes occur on even shorter time-scales on the smaller Devon Island Ice Cap (Paterson and Reeh, 2001).

The thickening in the northwest sector of the high elevation region, where the calculated rate of thickening is greater than its associated uncertainty, could be the result of a decrease in the mean annual specific outflow relative to the mean annual net accumulation. This would result in decreased ice flux from the high elevation accumulation zone to the low elevation ablation zone, which could explain the concurrent high elevation thickening and low elevation thinning. The east-west laser altimetry flight line, which appears to be thickening slightly faster than the north-south flight line, approximates the main north-south drainage divide of the ice cap (Abdalati and others, 2004). Dynamic thickening due to decreased outflow from the accumulation zone would be expected to be a maximum along the main drainage divide, where lateral flow is negligible. Therefore the observation that the drainage divide (east-west line) appears to be thickening slightly faster than other areas of the high elevation region (north-south line) supports a change in ice dynamics as the cause of the observed thickening (Abdalati and others, 2004; Figure 3-3).

A potential contributing factor to the observed thickening is the downwards diffusion of the Neoglacial cooling temperature signal, which may have resulted in a stiffening of the ice near the bed where the most shear occurs, thereby slowing outflow. If the Neoglacial cooling is assumed to have begun around 2000 years BP, and peaked during the Little Ice Age (200 years BP), it can be assigned a period of approximately 3600 a. A temperature cycle of this period can propagate downwards through an ice mass to a depth of approximately 610 m (where its amplitude reaches 5 % of the surface value; Paterson, 1994). This propagation is not instantaneous, with peak cooling at depth lagged approximately 1700 years behind peak cooling at the surface (Paterson, 1994). The ice depth in flux basins 3 and 4 (where thickening beyond uncertainty is observed) ranges from approximately 600 m near the summit, to approximately 250 m across the flux gates along the 1200 m contour (Dowdeswell and others, 2004). Therefore, it is possible that Neoglacial cooling has only recently begun near the glacier bed in these basins (< 300 a), and further cooling, and subsequent stiffening of the ice, can be expected for some time (> 1500 a).

The laser altimetry derived rate of thickness change is approximately 2 to 5 times greater than the rate of thickness change calculated in this thesis (between 0.015 and

0.043 mWE a^{-1} (Abdalati and others, 2004) versus 0.009 ± 0.152 mWE a^{-1}). To reconcile our findings with the laser altimetry observations, we must assess the difference in the magnitudes of the calculated and observed rates of thickness change. This difference in magnitude may partially be explained by the previously mentioned spatial bias in the laser altimetry observations to the western portion of the high elevation region, where the calculated rate of thickening is greatest. A lower thickening rate might have been found if more eastern laser altimetry observations had been included. The laser altimetry observations and calculated rates of thickness change also pertain to different time periods. The calculated rate is assumed to be an approximately 40-year mean rate of thickness change, while the repeat laser altimetry observations pertain to a more recent 5-year mean rate of thickness change. It should be stressed however, that the calculated specific outflow rate ($d\bar{h}_O/dt$) was determined from one annual velocity measurement which has been assumed to approximate the 40-year mean rate. If the specific outflow from the high elevation region has indeed been decreasing over time, then our estimate of specific outflow will be lower than the true 40-year mean, as it was sampled during the period of lowest surface flow velocities since 1963, and the 40-year mean rate of thickening will have been overestimated. Therefore, as the actual 40-year mean outflow rates are likely higher than our estimate, our calculated rate of thickening is probably an overestimate, with the true rate being < 0.009 mWE a^{-1}. This results in an even larger discrepancy with the rates found by Abdalati and others (2004; 0.015 to 0.043 mWE a^{-1}).

3.5 – CONCLUSION

The objectives of this chapter have been to (i) calculate flux basin-scale rates of thickness change across the high elevation region of the Devon Island Ice Cap, (ii) provide an indication of how representative the NASA laser altimetry observations are of the high elevation region, and (iii) assess whether there has been a recent change in ice dynamics in the high elevation region of the Devon Island Ice Cap.

(i) Our calculations suggest that the high elevation region of the Devon Island Ice Cap is thickening slightly, although the magnitude of the associated uncertainty is far greater than the magnitude of the rate of thickness change (0.009 ± 0.152 mWE a^{-1}). A contrast is seen in the behaviour of flux basins south and north of the main drainage

divide. The southern portion of the high elevation region appears to be more dynamically active than the northern portion, with higher net accumulation and outflow rates. Our calculations suggest that the southern portion of the high elevation region is most likely to be thinning (-0.029 ± 0.165 mWE a^{-1}), while the northern portion is most likely to be thickening (0.054 ± 0.137 mWE a^{-1}). Both of these rates, however, lie within error of zero, and therefore should not be interpreted as conclusive evidence of thickening or thinning. In most flux basins, the rates of thickness change appear to be too low to be accurately resolved by the methods used in this paper ($< |0.2|$ mWE a^{-1}).

(ii) Although our calculations agree with the trend of high elevation thickening suggested by the NASA laser altimetry observations (Abdalati and others, 2004), the calculated rate is approximately 2 to 5 times lower. This difference can be partially attributed to spatial bias in the laser altimetry measurements, both towards the western portion of the high elevation region, where we find thickening to be greater than in the eastern portion, and to the region of the main drainage divide, where dynamic thickening would be expected to be greatest. Future estimates of the rate of thickening would benefit from either improved spatial distribution of the laser altimetry measurements or a reduction in the uncertainty associated with calculated specific outflow.

(iii) We speculate that the slight thickening detected in this study is more likely to be indicative of a recent change in ice dynamics, which has resulted in a decrease in the specific outflow rate relative to the net accumulation rate, than a period of anomalously high net accumulation. This decrease in specific outflow may be due to the downwards diffusion of the Neoglacial cooling temperature signal, which has resulted in a stiffening of the ice near the bed, reducing outflow from the high elevation region of the ice cap. This general thickening trend does not apply to the entire high elevation region however, as thickening only exceeds uncertainty in the northwest portion of the high elevation region, and 2 flux basins in the southern portion are thinning at a rate greater than their associated uncertainty. A decreasing rate of specific outflow from the high elevation region would be expected to result in an increasing rate of thickening. This is supported by the observation that the 5-year mean rate of thickening observed by laser altimetry is greater than the approximately 40-year mean rate calculated in this paper.

3.6 – LITERATURE CITED

Abdalati, W., W. Krabill, E. Frederick, S. Manizade, C. Martin, J. Sonntag, R. Swift, R. Thomas, J. Yungel and R. Koerner. 2004. Elevation changes of ice caps in the Canadian Arctic Archipelago. *J. Geophys. Res.* **109** (F04007), doi:10.1029/2003JF000045.

Bales, R., J. McConnell, E. Mosley-Thompson and B. Csatho. 2001. Accumulation over the Greenland ice sheet from historical and recent records. *J. Geophys. Res.* **106**, 33,813-33825.

Burgess, D. and M. Sharp. 2004. Recent changes in areal extent of the Devon Ice Cap, Nunavut, Canada. *Arct., Antarc., Alp. Res.* **36**, 261-271.

Burgess, D., M. Sharp, D. Mair, J. Dowdeswell and T. Benham. 2005. Flow dynamics and ice-berg calving rates of the Devon ice cap, Nunavut, Canada. *J. Glaciol.* **51**, 219-230.

Dowdeswell, J., T. Benham, M. Gorman, D. Burgess and M. Sharp. 2004. Form and flow of the Devon Island Ice Cap, Canadian Arctic. *J. Geophys. Res.* **109** (F02002), doi:10.1029/2003JF000095.

Dunphy, P. and Dibb, J. 1994. ^{137}Cs gamma-ray detection at Summit, Greenland. *J. Glaciol.* **40**, 87-92.

Dyurgerov, B. and M. Meier. 2005. Glaciers and the changing earth system: a 2004 snapshot. INSTAAR. *University of Colorado Occasional Paper*. 58: 80309-0450.

Johannessen, O., K. Khvorostovsky, M. Miles and L. Bobylev. 2005. Recent ice-sheet growth in the interior of Greenland. *Science*. **310**, 1013-1016.

Kaser, G., J. Cogley, M. Dyurgerov, M. Meier and A. Ohmura. 2006. Mass balance of glaciers and ice caps: consensus estimates for 1961-2004. *Geophys. Res. Lett.* **35** (L19501), doi:10.1029/2006GL027511.

Koerner, R. 2005. Mass balance of glaciers in the Queen Elizabeth Islands, Nunavut, Canada. *Ann. Glaciol.* **42**, 417-423.

Krabill, W., E. Hanna, P. Huybrechts, W. Abdalati, J. Cappelen, B. Csatho, E. Frederick, S. Manizade, C. Martin, J. Sonntag, R. Swift, R. Thomas and J. Yungel. 2004. Greenland Ice Sheet: Increased coastal thinning. *Geophys. Res. Lett.* **31** (L24402), doi:10.1029/2004GL021533.

Le Brocq, A., A. Payne and M. Siegert. 2006. West Antarctic balance calculations: impact of flux-routing algorithm, smoothing algorithm and topography. *Comp. Geosci.* **32**, 1780-1795.

Mair, D., D. Burgess and M. Sharp. 2005. Thirty-seven year mass balance of Devon Ice Cap, Nunavut, Canada, determined by shallow ice coring and melt modeling. *J. Geophys. Res.* **110** (F01011), doi:10.1029/2003JF000099.

Paterson, W. 2002. *The Physics of Glaciers*. 3rd Ed. Butterworth-Heinemann. pp 251-252.

Paterson, W. and N. Reeh. 2001. Thinning of the ice sheet in northwest Greenland over the past forty years. *Nature*. **414**, 60-62.

Raper, S. and R. Braithwaite. 2006. Low sea level rise projections from mountain glaciers and icecaps under global warming. *Nature*. **439**, 311-313.

Raper, S. and R. Braithwaite. 2002. Glaciers and their contribution to sea level change. *Phys. Chem. Earth*. **27**, 1445-1454.

Reeh, N. and W. Paterson. 1988. Application of a flow model to the ice-divide region of

the Devon Island Ice Cap, Canada. *J. Glaciol.* **34,** 55-63.

Thomas, R., B. Csatho, S. Gogineni, K. Jezek and K. Kuivinen. 1998. Thickening of the western part of the Greenland ice sheet. *J. Glaciol.* **44**, 653-658.

Thomas, R., T. Akins, B. Csatho, M. Fahnestock, S. Gogineni, C. Kim and J. Sonntag. 2000. Mass balance of the Greenland Ice Sheet at high elevations. *Science.* **289**, 426-428.

Thomas, R., B. Csatho, C. Davis, C. Kim, W. Krabill, S. Marizade, J. McConnell and J. Sonntag. 2001. Mass balance of higher-elevation parts of the Greenland ice sheet. *J. Geophys. Res.* **106**, 33,707-33,716.

van der Veen, C., D. Bromwich, B. Csatho and C. Kim. 2001. Trend surface analysis of Greenland accumulation. *J. Geophys. Res.* **106**, 33,909-33,918.

Figure 3-1 – The Devon Island Ice Cap, in the Canadian High Arctic (**inset**), shown in an orthorectified mosaic of Landsat 7 images acquired in July and August of 1999, overlaid with a 1 km DEM based on the measurements of Dowdeswell and others (2004). Contour spacing is 100 m with the 1200 m contour highlighted. The locations of the 13 shallow firn cores used in this paper are shown (Chapter 2: circles; Mair and others, 2005: squares).

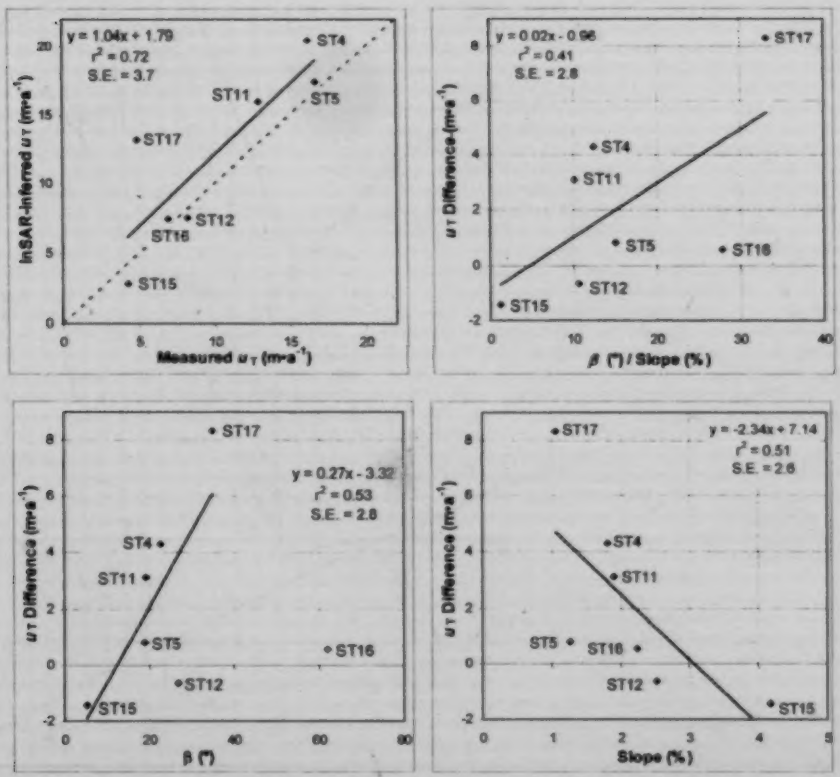

Figure 3-2 – Top Left: InSAR-derived down-slope surface velocities (Burgess and others, 2005) regressed against measured stake velocities for the 7 stakes for which data are available. Line x = y is shown for reference (dashed). **Top Right:** The difference between InSAR-derived and measured stake velocities regressed against the ratio of the angle between the satellite look and ice flow directions (β) to surface slope. **Bottom Left:** The difference between InSAR-derived and measured stake velocities regressed against β with the stake 16 outlier removed. **Bottom Right**: The difference between InSAR-derived and measured stake velocities regressed against surface slope. The regression value (r^2) and standard error of the estimate (S.E.) are given in each plot.

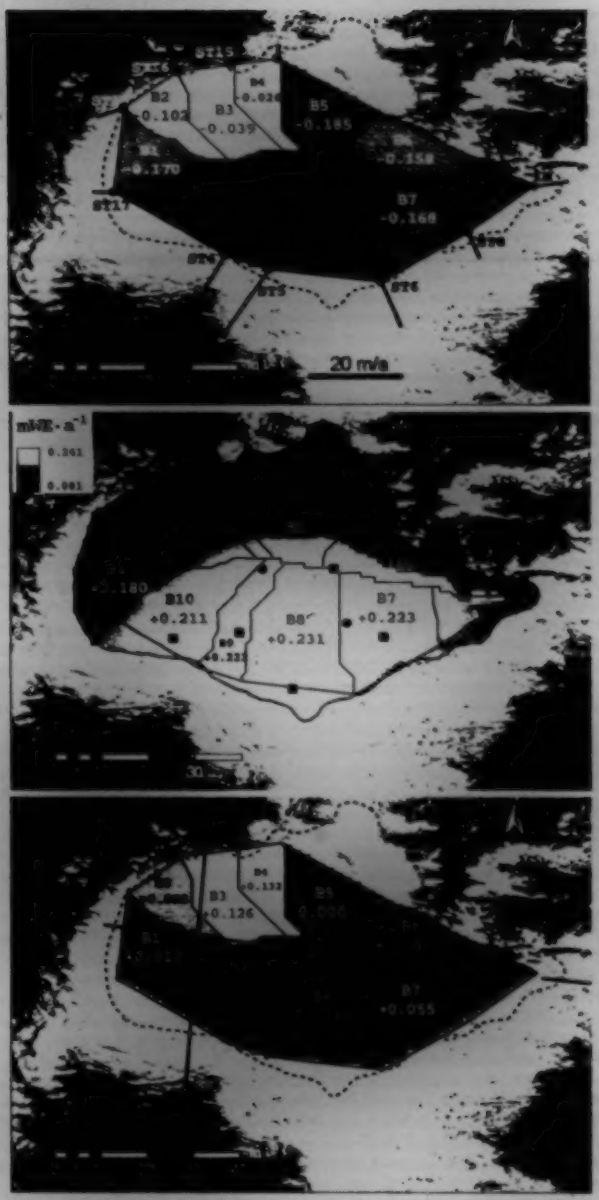

Figure 3-3 – Top: The mean annual rate of specific outflow (dh_O/dt; mWE a^{-1}; Equations 3-1 to 3-6). The 10 stakes (ST) and 1 InSAR-derived velocity point (IN) are shown with velocity vectors exaggerated 1000 times. **Centre:** The mean annual net accumulation rate (dh_A/dt; mWE a^{-1}; Equation 3-7), based on net accumulation rates at 13 cores sites (Chapter 2: circles; Mair and others, 2005: squares). **Bottom:** The mean annual rate of thickness change (dh/dt; mWE a^{-1}; Equation 3-8). The approximate locations of the NASA laser altimetry flight lines are also shown (solid lines; Abdalati and others, 2004).

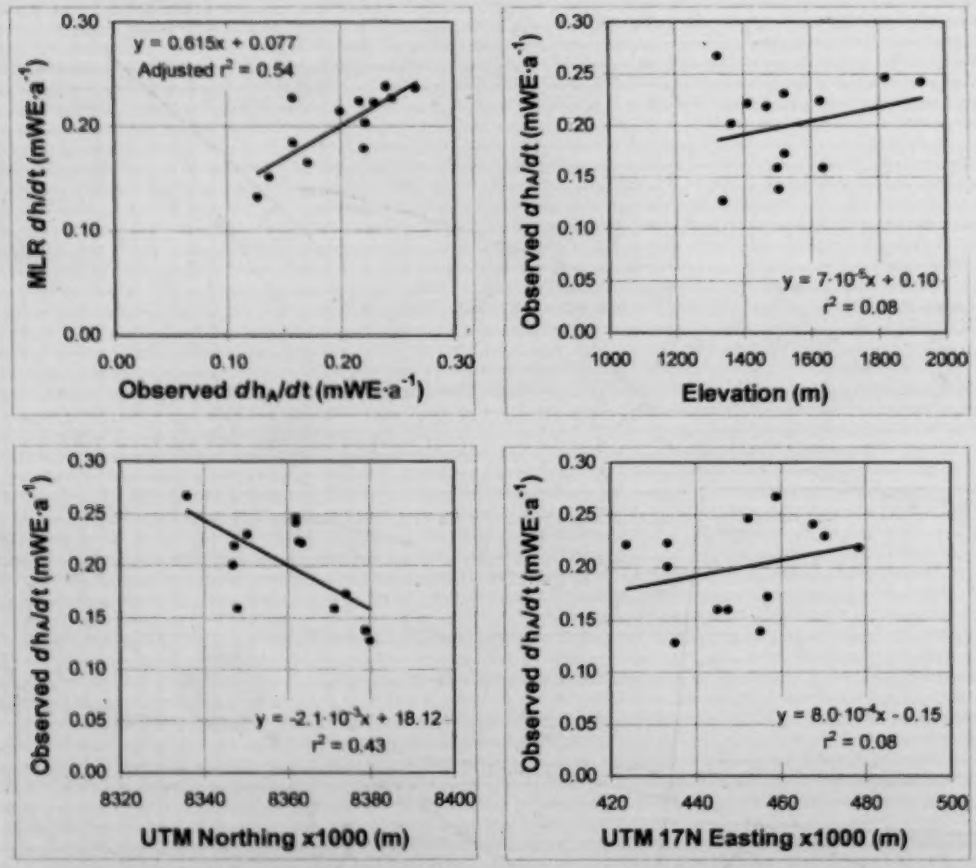

Figure 3-4 – Top Left: Multiple linear regression-derived annual net accumulation rate (MLR; Equation 3-7) versus observed mean annual net accumulation rate (dh_A/dt) at the 13 core sites (residuals: Table 3-3). **Top Right:** Core site elevation versus observed dh_A/dt. **Bottom Left:** Universal Transverse Mercator (UTM) northing (latitude) versus observed dh_A/dt. **Bottom Right:** Easting in UTM zone 17N (longitude) versus observed dh_A/dt. Regression values (r^2) are given in each plot. Core locations are shown in Figure 3-1.

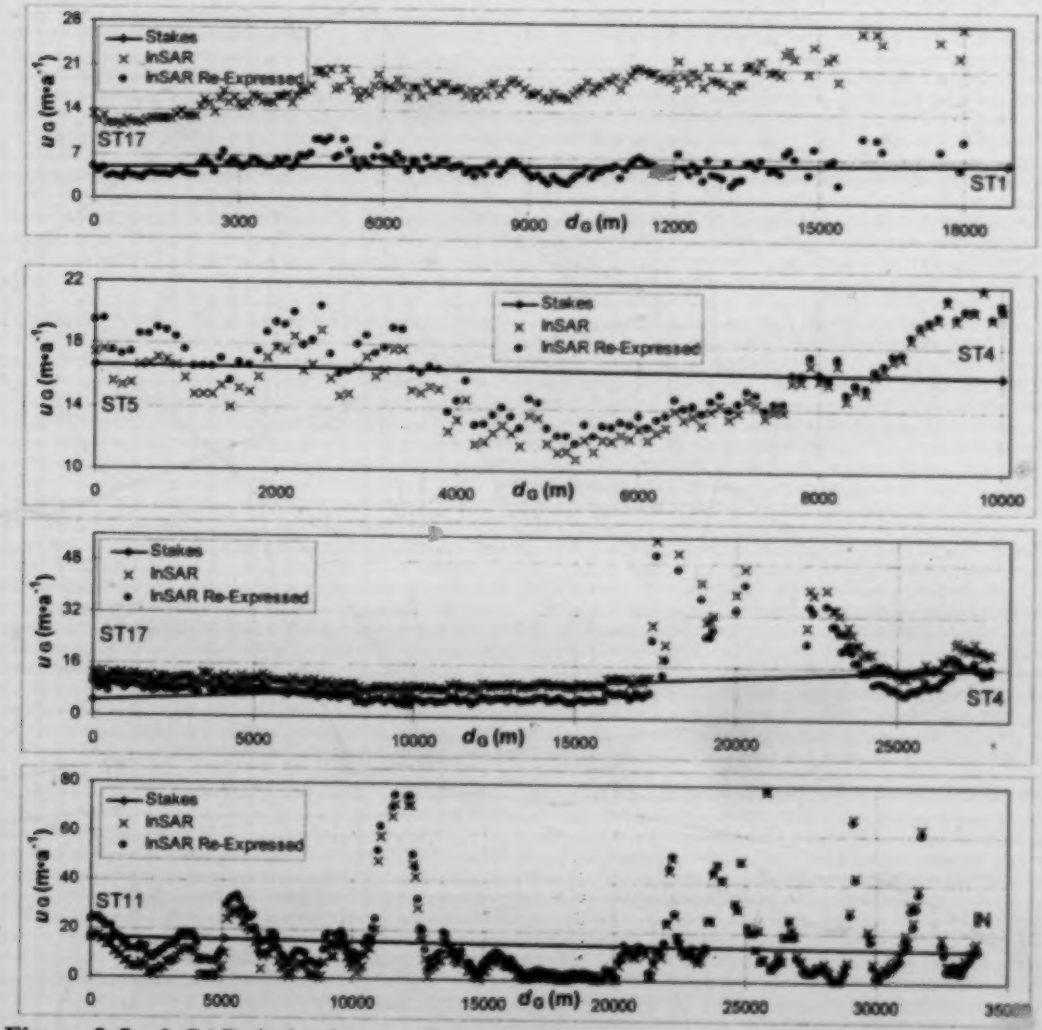

Figure 3-5 – InSAR-derived across flux gate (d_G) surface velocity (u_G) profiles (points) are compared to the inferred two-point stake velocity profiles (lines) across flux gates 1, 9, 10 and 6 (in descending order). Original InSAR-derived velocity points (crosses) have been linearly detrended and re-expressed as deviations from the two-point stake profile (circles). The standard error of the estimate of the re-expressed InSAR profile has been taken to represent the uncertainty in the horizontally-averaged velocity ($\sigma_H[u_G]$; Figure 3-8).

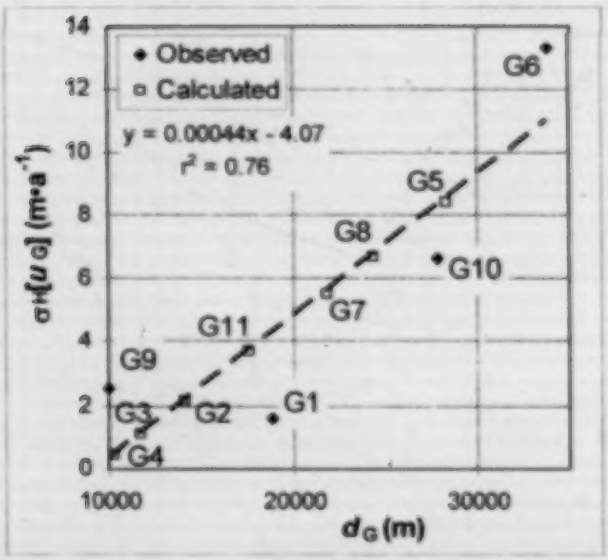

Figure 3-6 – Uncertainty in the horizontally-averaged velocity ($\sigma_H[u_G]$) as a function of flux gate width (d_G). For flux gates 1, 6, 9 and 10 $\sigma_H[u_G]$ has been taken as the standard error of the estimate of the re-expressed InSAR profile (Figure 3-7). The $\sigma_H[u_G]$ values for the remaining flux gates were calculated using the resulting regression.

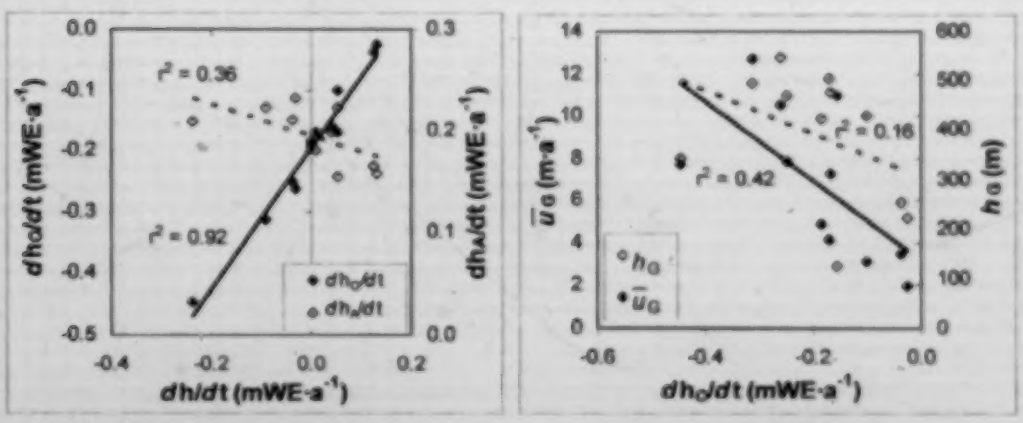

Figure 3-7 – Left: Mean annual net accumulation rate ($d\bar{h}_A/dt$) and rate of specific outflow ($d\bar{h}_O/dt$) versus the rate of rate of thickness change ($d\bar{h}/dt$) in the 11 flux basins. **Right:** Depth averaged outflow velocity ($\overline{u_G}$; solid line) and mean ice thickness ($\overline{h_G}$; dashed line) versus the rate of specific outflow ($d\bar{h}_O/dt$) in the 11 flux basins.

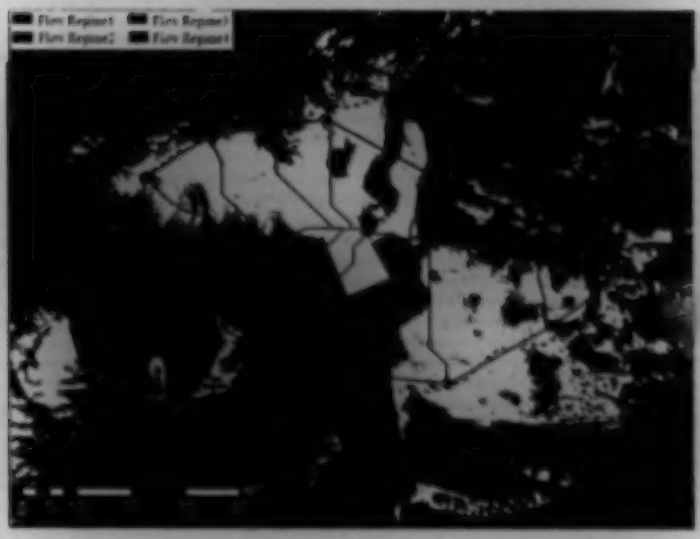

Figure 3-8 – The four flow regimes of the Devon Island Ice Cap according to Burgess and others (2005), with the 11 flux basins and velocity points within the high elevation region (> 1200 m: dashed contour) used in this study overlaid.

Table 3-1 – The angle between the satellite look and ice flow directions (β), the surface slope, and the ratio of β to surface slope at the 7 stakes in Figure 3-2.

Stake	β (°)	Slope (%)	β / Slope
4	23	1.82	12.5
5	19	1.26	15.0
11	19	1.90	10.1
12	27	2.52	10.6
15	5	4.17	1.3
16	62	2.24	27.8
17	35	1.06	33.2

Table 3-2 – The flux basin area ($A_B \pm \sigma[A_B]$), flux gate width (d_G) and flux gate mean ice thickness ($\overline{h_G} \pm \sigma[\overline{h_G}]$) for the 11 flux basins. The uncertainty in flux gate width ($\sigma[d_G]$) is < ± 10 cm for all gates.

Flux Gate	$A_B \pm \sigma[A_B]$ (m^2 x 10^8)	d_G (m)	$\overline{h_G} \pm \sigma[\overline{h_G}]$ (m)
1	2.10 ± 0.21	18,865	505 ± 10
2	1.69 ± 0.17	14,112	430 ± 10
3	2.36 ± 0.24	11,734	251 ± 10
4	1.53 ± 0.15	10,290	220 ± 10
5	2.84 ± 0.28	28,350	423 ± 10
6	2.60 ± 0.26	33,838	123 ± 10
7	4.05 ± 0.41	21,839	476 ± 10
8	4.84 ± 0.48	24,389	547 ± 10
9	1.80 ± 0.18	10,008	494 ± 10
10	3.67 ± 0.37	27,884	468 ± 10
11	0.93 ± 0.09	17,608	341 ± 10

Table 3-3 – The multiple linear regression (MLR) residuals at each of the 13 shallow core sites (Figure 3-4). Core locations shown in Figure 3-1.

Core Site	MLR Residual (mWE a^{-1})
C1	-0.003
C3	0.004
C4	0.025
C5	0.013
C6	0.013
C7	0.067
C8	-0.031
C9	0.006
CA	-0.042
CB	-0.020
CC	-0.019
CD	-0.007
CE	-0.007

Table 3-4 – The mean of the two-point stake-inferred and the mean of the InSAR-derived (where available) across-gate surface velocity profiles (u_G), across-gate InSAR coverage, uncertainty in the horizontally-averaged velocity profile ($\sigma_H[u_G]$; Figure 3-8), uncertainty in the vertically-averaged velocity profile ($\sigma_V[\overline{u_G}]$; Equation 3-10) and total uncertainty in the depth-averaged velocity profile ($\sigma[\overline{u_G}]$; Equation 3-11) for the 11 flux gates.

Flux Gate	Stake u_G (m a^{-1})	InSAR u_G (m a^{-1})	InSAR Coverage (%)	$\sigma_H[u_G]$ (m a^{-1})	$\sigma_V[\overline{u_G}]$ (m a^{-1})	$\sigma[\overline{u_G}]$ (m a^{-1})
1	5.18	17.77	82	1.62	0.43	1.67
2	6.54	-	7	2.14	0.33	2.16
3	5.62	-	35	1.09	0.36	1.15
4	3.81	-	12	0.46	0.20	0.50
5	8.11	-	40	8.40	0.51	8.42
6	14.63	11.73	93	13.33	1.14	13.38
7	9.17	-	5	5.54	0.76	5.59
8	14.14	-	60	6.66	1.10	6.75
9	16.40	15.39	100	2.54	1.32	2.86
10	4.88	14.28	85	6.62	0.81	6.67
11	11.53	-	37	3.68	0.80	3.76

Table 3-5 – The mean annual rate of specific outflow ($d\bar{h}_O/dt \pm \sigma[d\bar{h}_O/dt]$; Figure 3-3), mean annual net accumulation rate ($d\bar{h}_A/dt \pm \sigma[d\bar{h}_A/dt]$; Figure 3-5) and mean annual rate of thickness change ($d\bar{h}/dt \pm \sigma[d\bar{h}/dt]$; Figure 3-6) in the 11 flux basins, as well as the area-averaged mean for the entire high elevation region.

Flux Basin	$d\bar{h}_O/dt \pm \sigma[d\bar{h}_O/dt]$ (mWE a^{-1})	$d\bar{h}_A/dt \pm \sigma[d\bar{h}_A/dt]$ (mWE a^{-1})	$d\bar{h}/dt \pm \sigma[d\bar{h}/dt]$ (mWE a^{-1})
1	-0.170 ± 0.071	0.180 ± 0.023	0.010 ± 0.075
2	-0.102 ± 0.071	0.154 ± 0.023	0.053 ± 0.075
3	-0.039 ± 0.014	0.165 ± 0.023	0.126 ± 0.027
4	-0.026 ± 0.007	0.158 ± 0.023	0.132 ± 0.024
5	-0.185 ± 0.320	0.185 ± 0.023	0.000 ± 0.321
6	-0.158 ± 0.194	0.198 ± 0.023	0.040 ± 0.195
7	-0.168 ± 0.131	0.223 ± 0.023	0.055 ± 0.133
8	-0.261 ± 0.170	0.231 ± 0.023	-0.030 ± 0.172
9	-0.314 ± 0.080	0.222 ± 0.023	-0.092 ± 0.083
10	-0.250 ± 0.216	0.211 ± 0.023	-0.039 ± 0.217
11	-0.447 ± 0.225	0.210 ± 0.023	-0.237 ± 0.227
Mean	-0.191 ± 0.149	0.201 ± 0.023	0.009 ± 0.159

Chapter 4: Influence of source and transport variability on anion deposition records from the Devon Island Ice Cap, Nunavut, Canada

4.1 – INTRODUCTION

Ions are deposited on and stored within the snowpacks of ice caps and glaciers (Legrand and Mayewski, 1997). The dating of successive annual layers in ice cores allows a temporal record of ion deposition to be reconstructed and used as a proxy for regional atmospheric chemistry (Legrand and Mayewski, 1997). A sound comprehension of the historical trends and variability of atmospheric gases and aerosols, which can strongly influence the global radiation balance, is integral to the accurate forecasting and modeling of atmospheric chemistry (Hauglustaine and others, 1994; Iziomon and others, 2006). Likewise, the relationship between ice core sea-salt aerosol records and sea ice concentration is of great interest in providing insight into the long term trends and variability of Arctic sea ice extent and concentration (Grumet and others, 2001; Goto-Azuma and others, 2002). Arctic sea ice, which has been decreasing in both extent and concentration over the observed satellite record (1979 to present), influences the global radiation budget through its high albedo and also limits the heat flux from the ocean to the atmosphere (Cavalieri and others, 1997; Johannessen and others, 2004). Several Arctic ice core studies have provided evidence of increasing annual deposition of anthropogenic pollutants since the industrial revolution (Goto-Azuma and Koerner, 2001; Burkhart and others, 2006). Although an anthropogenic influence is recognizable within many Arctic deposition records, the precise identification of specific anthropogenic emissions source regions remains elusive (Goto-Azuma and Koerner, 2001).

To properly employ the glaciochemistry of ice cores as anthropogenic emissions and sea ice concentration proxies, transfer functions must be developed to differentiate between the variance in annual deposition records caused by emissions, atmospheric transport, and storage variability (O'Dwyer and others, 2000; Slater and others, 2001). The specific goals of this study are to (i) produce records of sulphate (SO_4^{2-}), nitrate (NO_3^-), methanesulphonic acid (MSA; CH_3SO_3H) and chloride (Cl^-) deposition on the Devon Island Ice Cap using five shallow firn cores (Figure 4-1), and (ii) relate inter-

annual deposition variability within the annually dated record of the highest and best preserved core to variability in source emissions and atmospheric transport.

During pre-industrial times (pre-1850), oxidation of the MSA produced by marine biota is believed to have been the main source of tropospheric sulphur dioxide (SO_2; the precursor to SO_4^{2-}), surpassing even volcanoes (Davis and others, 1998). Several studies have recently shown that anthropogenic SO_2 emissions are now the main source for tropospheric SO_4^{2-} concentrations in the Canadian High Arctic (Norman and others, 1999; Sirois and Barrie, 1999). Anthropogenic emissions are believed to constitute 62 % of tropospheric SO_4^{2-} during the summer months and 78 % during the remainder of the year (Li and Barrie, 1993). Highly effective long-range transport conveys anthropogenic SO_2 emissions from their source regions in the industrialized areas of Europe, North America and Asia, to the Arctic within days to weeks (Shaw, 1995; Kahl and others, 1997). The long-range transport of anthropogenic SO_2 emissions into the Arctic is most effective during polar night (November through February), when the Arctic front reaches as far south as 40 °N on the Asian continent, and encompasses maximum emission sources (Shaw, 1995; Stohl, 2006). In some regions of the Arctic, favourable pressure gradients during positive North Atlantic Oscillation (NAO+) and Arctic Oscillation (AO+) phases can further enhance northward transport of European and North American emissions during polar night (Eckhardt and others, 2003; Burkhart and others, 2006). During polar night, tropospheric SO_2 concentrations increase, as strong temperature gradients, low precipitable water, and the stable nature of the polar high create an environment where aerosols are not readily scavenged by precipitation from the troposphere (Shaw, 1995; Toom-Sauntry and Barrie, 2002). At polar sunrise (March), photochemical reactions convert the SO_2 that has built up during polar night into SO_4^{2-}, which is more readily scavenged by the spring snowfall (Sirois and Barrie, 1999; Toom-Sauntry and Barrie, 2002). This leads to a lag between peak tropospheric and snowfall SO_4^{2-} concentrations, with the latter reaching a peak in March through May (Sirois and Barrie, 1999; Toom-Sauntry and Barrie, 2002). The Arctic haze observed annually following polar sunrise is a visible manifestation of peak tropospheric SO_4^{2-} concentrations (Shaw, 1995; Iziomon and others, 2006).

Anthropogenic NO*x* (NO and NO_2; the precursor to NO_3^-) emissions have overtaken natural sources as the primary emissions source for both global (Galloway and others, 2003; Holland and Lamarque, 1997) and Arctic (Goto-Azuma and Koerner, 2001; Hastings and others, 2004) tropospheric NO*x* concentrations. Unlike tropospheric SO_2 however, tropospheric NO*x* has a relatively short residence time, being returned to the earth's surface within days of emission, either through dry deposition of NO*x*, or wet deposition of nitric acid (HNO_3), which is produced from NO*x* through a variety of pathways (Holland and Lamarque, 1997; Galloway and others, 2003). The larger aerosol size of NO_3^-, in comparison to SO_4^{2-}, also leads to more efficient scavenging by the limited snowfall during polar night (Toom-Sauntry and Barrie, 2002). Similar to SO_2, tropospheric NO_3^- concentrations reach a peak in the Canadian High Arctic during polar night (Sirois and Barrie, 1999). Peak snowfall NO_3^- concentrations display only a minor lag, however, and remain elevated from December until May (Toom-Sauntry and Barrie, 2002).

Marine sources, rather than anthropogenic emissions, are the main source for tropospheric Cl^-. Sea salt aerosols, including sodium chloride (NaCl), are primarily introduced into the marine boundary layer by wave action at the ocean surface (Kaleschke and others, 2004). Recently however, it has been suggested that Cl^- may also be transferred to the troposphere via frost flowers, ice crystals which form on recently frozen sea ice, and are supersaturated in sea-salts with a high effective surface area. The frost flower mechanism however, is believed to be spatially and temporally limited (Kaleschke and others, 2004). Observations at Alert, Nunavut, suggest that the majority (95 %) of the variability in tropospheric Cl^- concentrations in the Canadian High Arctic is dominated by a sea-salt signal (Sirois and Barrie, 1999). During polar night, tropospheric Cl^- concentrations increase until a rapid depletion at polar sunrise, when Cl^- ions are involved in a variety of photochemical reactions (Sander and others, 1997; Foster and others, 2001). There is no lag between peak tropospheric and snowfall Cl^- concentrations, with both exhibiting a December through February peak (Sirois and Barrie, 1999; Toom-Sauntry and Barrie, 2002).

Tropospheric and snowfall MSA concentrations are approximately two orders of magnitude lower than SO_4^{2-} and NO_3^- concentrations (Davis and others, 1998; Toom-

Sauntry and Barrie, 2002). Although the reaction pathways and controls of MSA production are still not completely understood, it is recognized to be an atmospheric oxidation product of dimethyl sulfide (DMS; $(CH_3)_2S$), with a heterogeneous spatial distribution. DMS is a strictly biogenic compound produced by marine biota, which is converted to MSA in a temperature-dependent reaction at the ocean-atmosphere interface (Davis and others, 1998; Trevena and Jones, 2006). Marine DMS emissions are the main source for tropospheric MSA in the Canadian High Arctic (Li and Barrie, 1993; Sirois and Barrie, 1999). In both the Arctic and the Antarctic, the activity of DMS-producing marine biota (*Phaeocytis pouchetii*) is influenced by sea ice conditions and sea surface temperature (O'Dwyer and others, 2000; Isaksson and others, 2006). Tropospheric and snowfall MSA concentrations both reach maxima in the Canadian High Arctic between May and September (Sirois and Barrie, 1999; Toom-Sauntry and Barrie, 2002). Tropospheric MSA concentrations exhibit distinct peaks in June-July and August-September, which have been suggested to be due to DMS emissions and long range transport from North Atlantic source areas followed by DMS emissions from proximal Arctic source areas (Sirois and Barrie, 1999; O'Dwyer and others, 2000).

4.2 – METHODS

4.2.1 – High resolution anion analysis

A detailed description of the recovery of the five shallow firn cores from the Devon Island Ice Cap can be found in Chapter 2. A Dionex ICS-2500 ion chromatograph was used to measure the concentrations of SO_4^{2-}, NO_3^-, MSA and Cl^- in samples taken at 3.1 ± 0.8 cm intervals along each core. Analyses were conducted using a gradient concentration of 22 to 40 mM potassium hydroxide (KOH) eluent, with a 100 µL injection volume. A Dionex AS18 column was used for the majority of samples (93 %) and a Dionex AS15 column was used for the remainder (7 %). The limits of detection (LOD), defined as three times the standard deviation of the lowest concentration standard in a randomly selected sequence of eight consecutive runs, were 0.033 µeq L^{-1} for SO_4^{2-}, 0.063 µeq L^{-1} for NO_3^-, 0.018 µeq L^{-1} for MSA and 0.097 µeq L^{-1} for Cl^- with the AS18 column, and 0.086 µeq L^{-1} for SO_4^{2-}, 0.109 µeq L^{-1} for NO_3^-, 0.015 µeq L^{-1} for MSA and 0.079 µeq L^{-1} for Cl^- with the AS15 column.

Over half of the AS15 samples were also analyzed with the AS18 column to ensure comparable results. Two-tailed t-tests of 107 randomly selected samples, assuming two populations with equal variance, revealed no significant differences ($p > 0.05$) between the NO_3^-, MSA and Cl^- concentrations measured by the two columns, and regressions of AS18 against AS15 concentration measurements had high coefficients of determination ($r^2 = 0.96$, 0.87 and 0.96 respectively) with slopes close to 1 (slope = 0.92, 1.18 and 0.97 respectively). Although AS18 and AS15 SO_4^{2-} concentrations are highly correlated ($r^2 = 0.98$), a similar t-test revealed a significant difference ($p < 0.05$) between the SO_4^{2-} concentrations measured by the two columns (slope = 0.70). This is likely a result of the bromine (Br^-) peak, immediately adjacent to the SO_4^{2-} peak, being better resolved by the AS18 column than by the AS15 column. AS15 SO_4^{2-} standards were therefore likely calibrated to a larger SO_4^{2-} peak area, which included some of the Br^- peak, than the AS18 SO_4^{2-} standards. To correct for this systematic difference between AS18 and AS15 SO_4^{2-} concentrations, all AS15 SO_4^{2-} concentrations were multiplied by 0.70 to make them equivalent to AS18 SO_4^{2-} concentrations.

In order to calculate robust annual anion deposition rates, and examine trends within the reconstructed record, the quality of the anion concentration dataset must be evaluated. Frequency distributions of the concentration dataset of each anion species show the presence of outliers, concentration values which are not part of the main population of values. We interpret the outliers as evidence of either sample contamination during processing, such as elevated Cl^- concentrations in the deionized rinse water, or the misidentification of chromatograph peaks by the ion chromtograph, such as abnormally large organic acid peaks over-riding the MSA peak and being mistakenly identified as MSA. We established an outlier threshold, conservatively defined as 5 standard deviations above the mean concentration, and concentration measurements in excess of this threshold were removed from the dataset and replaced by the mean concentration of the two adjacent samples. Of the 3275 samples processed from the five cores, 10 SO_4^{2-}, 8 NO_3^-, 16 MSA and 27 Cl^- outliers, in some cases involving up to 6 samples in a row, were replaced.

4.2.2 – Glaciochemistry records

Two distinct glaciochemistry records were extracted from the five Devon Island Ice Cap shallow firn cores. Long-term (1922 to 2003) anion deposition records were produced for each core from records of concentration that were dated using the Nye time-scale. These records are presented as 3-year running means, and were used to study long-term trends in anion deposition. As the Nye time-scale assumes a constant rate of net annual accumulation, it is not appropriate to use these records to examine inter-annual variability. Therefore, a short-term (1963 to 2003) record of annual anion deposition was produced from the portion of core C that could be dated by annual layer counting. Core C was selected for this as it comes from the highest elevation and has the best-preserved chemical stratigraphy (Chapter 2). This record was used to investigate the influences of inter-annual variability in anion sources and atmospheric transport on anion deposition. The Nye time-scale was chosen to date the five long term records to account for (i) the thinning of layers with depth due to compaction and ice deformation and (ii) the lack of a known age horizon in all cores that could be used to constrain annual layer counting prior to 1963 (O'Dwyer and others, 2000; Pohjola and others, 2002). For the Nye time-scale records, the age before recovery year of a given interval of a shallow ice core (t_i; expressed in years) was calculated according to (Nye, 1963):

$$t_i = -\frac{h}{c}\ln\left(\frac{z_i}{h}\right) \qquad \text{Equation 4-1}$$

where h is the ice thickness (expressed in mWE) at each core site derived from radio echo sounding measurements (Dowdeswell and others, 2004); c is the 1963 to 2003 mean annual accumulation rate (expressed in mWE a^{-1}; Chapter 2); and z_i is the ice thickness-equivalent height above the bed of a given interval of shallow ice core (expressed in mWE; Table 4-1).

The annual mean concentration of a given anion ($[C]_a$; expressed in μeq L^{-1}) was determined as:

$$[C]_a = \frac{\sum_{i=x}^{y}([a]_i \cdot V_i)}{\sum_{i=x}^{y}(V_i)} \qquad \text{Equation 4-2}$$

where $[a]_i$ and V_i represent the anion concentrations and volumes of the samples in a given year (expressed in μeq L^{-1} and L respectively), and x and y denote the first and last samples in a given year. The first and last samples in a given year were identified in each core using the Nye time-scale. In core C, the additional short-term deposition record was calculated based on the first and last samples identified to be in a given year by annual layer counting.

Using the annual mean concentration record and the cross-sectional area of the Kovacs MkII corer (A; calculated as 0.00608 m^2), the mean annual deposition of a given anion (D_a; expressed in μeq m^{-2}) was calculated according to:

$$D_a = \frac{[C]_a}{A} \cdot \sum_{i=x}^{y} (V_i) \qquad \text{Equation 4-3}$$

The counted and Nye time-scale anion deposition records derived for core C were compared during the common 1963 to 2003 period to assess differences arising from the use of the alternate dating methods.

4.2.3 – Long-term anion records: trends

The individual long term deposition records were smoothed with 3-year running means, to compensate for potential Nye time-scale dating errors in which 'annual layers' may exclude anion peaks in high net accumulation years, when the annual anion peaks are widely spaced with depth, or include multiple anion peaks in low net accumulation years, when the annual anion peaks are closely spaced with depth. A long term 3-year running mean standard normalized annual deposition record was then calculated for each species by averaging the standard normalized 3-year running means from the 5 cores. (Hereafter, 'standard normalized long term mean' anion deposition records are simply referred to as 'long term mean' anion deposition records unless otherwise stated.) To examine how representative the long term mean records are of the individual long term records which comprise them, each individual 3-year running mean long term deposition record was correlated to the 3-year running mean long term mean deposition record for the 1958 to 2003 period common to all five cores. The use of a running mean introduces autocorrelation into a record, reducing its effective sample size by 1.5 / w, where w is the number of points used in the running mean (Moore and others, 2006). Therefore, the use

of a 3-year running mean results in an effective sample size of half the original sample size.

4.2.4 – Short-term anion records: source variability

The influences of inter-annual variability in anion sources and atmospheric transport on the short-term anion deposition record from core C were investigated. Although anthropogenic emissions are the main source of SO_4^{2-} and NO_3^-, the ocean is a secondary source of both anions, contributing between 3 to 24 % and 15 to 29 % of the variability of each anion in the Canadian High Arctic atmosphere respectively (Sirois and Barrie, 1999). As a conservative marine tracer record, such as sodium (Na^+) or magnesium (Mg^+), is not yet available to complement the anion records from our five cores, we cannot assess the secondary ocean source components of the SO_4^{2-} and NO_3^- records at this time (Grumet and others, 2001; Toom-Sauntry and Barrie, 2002). Although Cl^- is primarily marine-derived, and Cl^- records have been used in the past to calculate anion sea-salt fractions (Pasteur and others, 1995), the participation of Cl^- in a variety of tropospheric gas phase reactions precludes it from being considered a conservative marine tracer (Keene and others, 1986; Toom-Sauntry and Barrie, 2002).

North America, Eastern and Western Europe and Northern Asia are all potential source areas for the SO_4^{2-} and NO_3^- deposited in the Canadian High Arctic (Goto-Azuma and Koerner, 2001). To identify a primary source region, the core C SO_4^{2-} deposition record was compared to the SO_2 emissions records of North America, Eastern and Western Europe and Northern Asia during the 1963 to 2003 period (Stern, 2005). Multiple linear regression (MLR) of the 3-year running mean core C SO_4^{2-} deposition record against the 3-year running mean SO_2 emissions records of the four potential source regions was performed. The residual core C SO_4^{2-} deposition record was taken to represent variability due to processes other than anthropogenic emissions variability, such as secondary (marine) source variability, and transport and storage variability. As anthropogenic NO*x* emissions data are not available at annual resolution for the 1963 to 2003 period, a similar assessment of possible source regions using the core C NO_3^- deposition record is not possible.

As the ocean is the main source of both tropospheric MSA and Cl^-, and sea ice cover modulates ocean-atmosphere interactions, the core C MSA and Cl^- deposition records were compared to annual records of the regional sea ice fraction for the seasons during which tropospheric and snowfall concentrations of these species reach a maximum in the Canadian High Arctic (Sirois and Barrie, 1999; Toom-Sauntry and Barrie, 2002). The 3-year running mean core C MSA deposition was compared to the 3-year running mean May through September (MJJAS) sea ice fraction, while the 3-year running mean core C Cl^- deposition was compared to the 3-year running mean October through February (ONDJF) sea ice fraction. Similar to Grumet and others (2001), the core C MSA and Cl^- deposition records were compared to a previously published northern hemisphere sea ice fraction dataset, gridded on a 4640 grid cell standard 1° latitude cylindrical projection grid (Walsh, 1978; Walsh and Chapman, 2006). Only the portion of the NSIDC sea ice fraction dataset within the previously defined Devon Island Ice Cap moisture source region of interest was used, as the ocean outside of this region has been shown to be an infrequent source area of low elevation air masses en route to the Devon Island Ice Cap (Chapter 2). Comparisons between the core C MSA and Cl^- deposition records and the sea ice fraction dataset are limited to the 1963 to 2003 period for which constrained annual layer counting is possible. The 1963 to 1979 portion of the sea ice fraction dataset was derived from observational charts gathered from a variety of sources, including the US Navy and Naval Oceanographic Office, British Meteorological Office, Canadian Meteorological Service and Danish Meteorological Institute, while the 1979 to 2003 portion of the dataset was derived from passive SMMR and SSMI microwave remote sensing using the NASA Team Algorithm (Walsh and Johnson, 1979; Chapman and Walsh, 1993; Walsh and Chapman, 2001). Although the 1963 to 1979 dataset suffers from both temporal and spatial interpolation of sea ice concentrations, it remains one of the most comprehensive sea ice data sets for the northern hemisphere (Chapman and Walsh, 1993; Chapman and Walsh, 2001).

Common modes of sea ice fraction variability during the 1963 to 2003 period were extracted through principal components analysis (PCA). PCA was performed on both the ONDJF ($n = 45$ and $p = 345$) and MJJAS ($n = 45$ and $p = 339$) seasonal sea ice fraction datasets within the moisture source region of interest (Singarayer and Bamber,

2003; Kinnard and others, 2006). The significance of principal components (PCs) could not be assessed using Rule N (Chapter 2), as the number of timeseries was greater than the length of the timeseries ($p > n$; Preisendorfer, 1988). Therefore, exponential curves were fitted to scree plots of percent variance explained versus PC to determine which PCs were likely to contain a signal different from noise (Singarayer and Bamber, 2003). The residual core C MSA and Cl^- deposition records were taken to represent variability in the anion deposition records due to processes other than marine emission (source) variability, such as transport and storage variability.

4.2.5 – Short term anion records: transport variability

The core C residual deposition records were compared to records of atmospheric transport variability during the 1979 to 2003 period. Similar to Kahl and others (1997; 1999) and Chapter 2, daily 120 hr kinematic back-trajectories for the summit of the Devon Island Ice Cap were calculated using the METEX model (Zeng and others, 2003) and NCEP / NCAR Reanalysis data (Kalnay and others, 1996). Each back-trajectory describes the most probable upwind path taken by a parcel of air arriving 500 m above ground level at the summit of the Devon Island Ice Cap at 0000 hr local time each day. Hourly back-trajectory points were gridded on an 814 cell conic grid centered on the North Pole (hereafter G814). For a given G814 cell, the monthly site-specific low elevation atmospheric transport density (D_{MX}; expressed per km^2) was computed according to:

$$D_{MX} = \frac{b_{MX}}{A_X \times d_M \times 24\text{h d}^{-1}} \qquad \text{Equation 4-4}$$

where b_{MX} is the number of hourly back-trajectory points (expressed in hr) counted in a given G814 cell (X) in a given month (M); A_X is the area of the given cell (expressed in km^2); and d_M is the number of days in the given month. As SO_2 accumulates within the Arctic front during polar night, the residual SO_4^{2-} deposition record was compared to a record of November through February (NDJF) atmospheric transport. A NDJF seasonal site-specific atmospheric transport density dataset (D_{SX}; expressed per km^2; Chapter 2) was calculated as the arithmetic mean of the November through February monthly site-specific atmospheric transport density values. Unlike

anthropogenic SO_2 emissions, both MSA and Cl^- oceanic emissions require atmosphere-ocean interaction to become entrained in the troposphere. Therefore, the residual MSA and Cl^- records were compared to records of low elevation air mass densities, which include only air masses traversing within 500 m of the ocean surface (Chapter 2), rather than to records of air mass densities crossing cells at all elevations. The core C residual MSA deposition record was compared to MJJAS low elevation site-specific atmospheric transport, while the core C residual Cl^- deposition record was compared to ONDJF low elevation site-specific atmospheric transport. PCA of the NDJF atmospheric transport record, as well as both the MJJAS and ONDJF low elevation atmospheric transport records, was used to discern primary modes of seasonal atmospheric variability. An exponential curve was fitted to a scree plot to identify significant modes of variability within these datasets (Singarayer and Bamber, 2003). The residual anion deposition records were compared to these proxies of seasonal atmospheric transport variability to examine the influence of site-specific atmospheric transport variability on anion deposition.

4.3 – RESULTS

4.3.1 – Comparison of the counted and Nye time-scales

Nye time-scale dating identified the 1963 ^{137}Cs horizon to within less than a year in core C, but differed from the counted time-scale by up to ± 2 years during some intervals between 1963 and 2003 (Figure 4-2). The pre-1963 dating uncertainty of the Nye time-scale is assumed to be similar to this post-1963 dating uncertainty. Although the counted time-scale is a better dating tool for the 1963 to 2003 period, the Nye time-scale allows comparable pre-1963 time-scales to be developed for all five cores. The oldest year in each core calculated using the Nye time scale ranged from 1922 (core D) to 1958 (core B; Table 4-1). A comparison of the counted and Nye time-scale anion deposition records from core C showed that the 3-year running mean annual deposition for a given year differed substantially depending on the dating method (SO_4^{2-} ± 44 %; NO_3^- ± 55 %; MSA ± 110 % and Cl^- ± 57 %). There appear to be distinct periods when the Nye time-scale deposition overestimates (1976 to 1983, 1988 to 1991 and 1995 to 2003) and underestimates (1963 to 1975, 1984 to 1987 and 1992 to 1994) counted time-

was found during the 1955 to 1995 period, a period defined by visual inspection (Figure 4-3).

4.3.3 – Short-term anion records: source and transport variability

The variability in the 3-year running mean core C SO_4^{2-} deposition record was compared to variability in the 3-year running mean SO_2 emissions records of the four potential source regions during the 1963 to 2003 period (Figure 4-4). MLR found that variability in the 3-year running mean core C SO_4^{2-} deposition record (D_{SO4}) was significantly correlated ($p < 0.01$, adjusted $r = 0.79$ and $df = 19$) to variability in the 3-year running mean SO_2 emissions records of Western (S) and Eastern (T) Europe, Northern Asia (U), and North America (V) according to:

$$D_{SO4} = -116.1S + 41.9T - 51.0U + 125.6V + 188.5 \quad \text{Equation 4-5}$$

A residual SO_4^{2-} deposition record was derived from the 3-year running mean core C SO_4^{2-} deposition record using the MLR equation above. This record is assumed to have source variability removed, and therefore to reflect the influences of transport and storage variability on the core C SO_4^{2-} deposition record. This residual core C SO_4^{2-} deposition record could not be compared with a site-specific transport variability dataset however, as no significant or primary mode of atmospheric transport variability was identified during polar night (NDJF) by PCA of the atmospheric transport dataset ($n = 24$ and $p = 526$; Figure 4-5). The initiation points of the daily 120 hr back-trajectories used to derive the NDJF site-specific atmospheric transport dataset indicate that only a very small percentage (< 1 %) of trajectories originate in industrialized regions (Figure 4-5). The NDJF site-specific atmospheric transport dataset therefore describes transport to the Devon Island Ice Cap from within the Arctic front, rather than long-range transport from lower latitude SO_2 emission source regions.

The variability in the 3-year running mean core C MSA deposition record was compared to variability in summer (MJJAS) sea ice fraction during the 1963 to 2003 period. A scree plot indicates two significant PCs of sea ice variability during the MJJAS season. MJJAS sea ice PC1 describes a significant decreasing trend in regional sea ice fraction ($p < 0.01$, $r = -0.89$ and $df = 39$) while MJJAS sea ice PC2 describes sea ice variability in Northern Baffin Bay and the Beaufort Sea (Figure 4-6). The 3-year running

mean core C MSA deposition record was found to be positively correlated to the 3-year running mean MJJAS PC1 ($p < 0.01$, $r = 0.65$ and $df = 19$) but not to PC2 ($p > 0.05$, $r = 0.02$ and $df = 19$; Figure 4-7).

A residual MSA deposition record was derived by regressing the 3-year running mean core C MSA deposition record against the 3-year running mean MJJAS PC1 ($p < 0.01$, $r = 0.65$ and $df = 19$). Similar to the residual SO_4^{2-} deposition record, the residual MSA deposition record is assumed to have source variability removed and therefore to reflect transport and storage-related variability. PCA ($n = 24$ and $p = 94$) of the MJJAS low elevation site-specific atmospheric transport dataset produced a significant atmospheric transport PC1 during the 1979 to 2003 period, which appears to represent a dipole between the Beaufort Sea / western Queen Elizabeth Islands and Baffin Bay (Figure 4-8). The residual MSA deposition record however, is not significantly correlated ($p > 0.05$, $r = -0.45$ and $df = 11$) to the 3-year running mean of this MJJAS atmospheric transport PC.

The variability in the 3-year running mean core C Cl^- deposition record was compared to variability in the winter (ONDJF) sea ice fraction during the 1963 to 2003 period. During the ONDJF season, a scree plot indicates three significant PCs of sea ice variability. Similar to the MJJAS sea ice PC1, ONDJF sea ice PC1 also describes a significant decreasing trend in regional sea ice fraction ($p < 0.01$, $r = -0.56$ and $df = 39$), while PCs 2 and 3 appear to describe a dipole of variability between the Beaufort Sea and southern Baffin Bay (Figure 4-6). The 3-year running mean core C Cl^- deposition record was found to be positively correlated to the 3-year running mean ONDJF PC1 ($p < 0.05$, $r = 0.42$ and $df = 19$), negatively correlated to the 3-year running mean ONDJF PC3 ($p < 0.01$ $r = -0.63$ and $df = 19$), and not correlated ($p > 0.05$, $r = -0.15$ and $df = 19$) to the 3-year running mean ONDJF PC2 (Figure 4-9). MLR found that variability in the 3-year running mean core C Cl^- deposition record (D_{Cl}) was significantly correlated ($p < 0.01$, adjusted $r = 0.72$ and $df = 19$) to variability in the 3-year running means of ONDJF PCs 1 (Q) and 3 (R) according to:

$$D_{Cl} = 138.9Q - 221.8R + 863.8 \qquad \text{Equation 4-6}$$

A residual Cl^- deposition record was derived from the 3-year running mean core C Cl^- deposition record using the MLR equation given above. Similar to the residual SO_4^{2-}

and MSA deposition records, the residual Cl^- deposition record is also assumed to have source variability removed, and therefore reflect transport and storage variability in the core C Cl^- deposition record. PCA (n = 24 and p = 94) of the ONDJF low elevation site-specific atmospheric transport dataset produced a significant atmospheric transport PC1 during the 1979 to 2003 period. Similar to the MJJAS season, this PC appears to represent a dipole between the Beaufort Sea / western Queen Elizabeth Islands and Baffin Bay (Figure 4-8). The residual Cl^- deposition record is not significantly correlated ($p > 0.05$, $r = -0.18$ and $df = 11$) to the 3-year running mean of this ONDJF atmospheric transport PC.

4.4 – DISCUSSION

4.4.1 – Signal-to-noise

Assuming that the long term mean deposition records best represent the deposition history of each anion species, and that 1 minus the correlation value between an individual 3-year running mean deposition record and the 3-year running mean of the composite deposition record from the 5 cores represents single-series noise variance, signal-to-noise ratios ($r / (1 - r)$; Goto-Azuma and others, 2002) of between 1.40 and 4.16 for SO_4^{2-}, 0.46 and 3.38 for NO_3^-, 0.56 and 2.49 for MSA and 0.26 and 1.46 for Cl^- are derived for the five core sites during the 1958 to 2003 period (Table 4-1). A similar examination of the signal-to-noise ratios in the five reconstructed net accumulation records (Chapter 2) finds similar values of between 0.87 and 4.42 (A: 2.57; B: 4.42; C: 3.55; D: 0.87 and E: 1.47). A previous study found signal-to-noise ratios of between 0.79 and 1.38, depending on ion species, in two 85 m ice cores recovered 2.5 m apart (Goto-Azuma and others, 2002). The cores investigated in this study were recovered up to 48 km apart (Figure 4-1). Although MSA is found at concentrations approximately two orders of magnitude lower than the other anions examined in this study, the MSA signal-to-noise ratios are similar to those of the other three long-term anion deposition records. As we assume that the anion sources and transport variability for the core sites are similar (Stohl, 2006), the large range of signal-to-noise ratios between cores and anions suggests the existence of significant spatial variability in deposition rates.

4.4.2 – Sources of anion deposition variability

Source variability was found to explain the majority of the variability in the 3-year running mean core C SO_4^{2-} ($r^2 = 0.62$) and Cl^- ($r^2 = 0.52$) deposition records, and a minority of the variability in the 3-year running mean core C MSA deposition record ($r^2 = 0.42$). As the primary modes of atmospheric transport variability identified during both the MSA and Cl^- deposition seasons were not found in the residual MSA and Cl^- deposition records, the remainder of the variability in these records ($1 - r^2$; 0.58 and 0.48 respectively) is assumed to be due to deposition / post-depositional variability. Post-depositional processes include photochemical reactions at the snow surface and the physical redistribution of anions through melting and wind redistribution of snow (Goto-Azuma and Koerner, 2001; Burkhart and others, 2006). We have no way of testing the validity of this assumption. This suggests that source and depositional / post-depositional variability are approximately equal sources of variability in the 3-year running mean core C MSA and Cl^- deposition records, while atmospheric transport variability has no discernable influence. This contrasts with sources of variability on much longer (glacial / interglacial) time-scales. An examination of dust and sea-salt concentrations in Greenland ice cores finds transport variability to be the main source of glaciochemistry variability, followed by source variability, with depositional / post-depositional variability having the smallest influence (Fischer and others, 2007).

4.4.3 – Anthropogenic sulphate and nitrate emissions

Similar to findings from previous studies, anthropogenic emissions source variability was evident in the mean SO_4^{2-} deposition record (Goto-Azuma and Koerner, 2001; Goto-Azuma and others, 2002). The long term mean SO_4^{2-} and NO_3^- deposition records allow trends to be assessed in the SO_4^{2-}:NO_3^- ratio during the 1922 to 2003 period (Figure 4-10). A significant decreasing trend was found in the SO_4^{2-}:NO_3^- ratio between 1985 and 2003 ($p < 0.01$, $r = -0.85$ and $df = 8$), while no significant trends were found during the other periods identified during break-point analysis (1936 to 1963 and 1964 to 1984). This decreasing trend in the SO_4^{2-}:NO_3^- ratio appears to be due to a decrease in SO_4^{2-} deposition, which was found to have a significant decreasing trend during the 1991 to 2003 period ($p < 0.05$, $r = -0.90$ and $df = 5$; Figure 4-3).

Although there is no strong support for a single SO_4^{2-} source region, a slightly higher correlation to North American emissions ($p < 0.01$, $r = 0.79$ and $df = 19$) than Western European emissions ($p < 0.01$, $r = 0.75$ and $df = 19$), as well as a qualitative examination of the emissions and deposition curves, suggests that North America is more likely to be the primary source area than Western Europe (Figure 4-4). We suggest that the majority of SO_4^{2-} deposition, and likely also NO_3^- deposition is derived from a combination of both sources. The apparent post-1973 decreasing trend in SO_4^{2-} deposition is likely due to decreases in Western European and North American SO_2 emissions, while the c. 1987 and c. 1995 SO_4^{2-} deposition peaks may be due to peaks in Eastern European and North Asian SO_2 emissions respectively (Figure 4-4). The lack of a primary mode of variance in the NDJF site-specific atmospheric transport dataset suggests that transport variability within the Arctic front to the Devon Island Ice Cap is either random or too minute to be resolved using the methods in this paper. The use of more lengthy back-trajectories (> 120 hr; Kahl and others, 1997; 1999) may improve the representation of site-specific NDJF long range transport variability to capture upwind anthropogenic source areas, external to the polar front, not reached by the shorter 120 hr trajectories (Reijmer and others, 2002).

4.4.4 – Sea ice-modulated MSA and chloride emissions

Similar to previous MSA studies in the Antarctic, we find a positive correlation between MSA deposition (core C 3-year running mean) and the MJJAS sea ice fraction (PC1; $p < 0.01$, $r = 0.65$ and $df = 19$), with both timeseries exhibiting significant decreasing trends ($p < 0.01$, $r > |0.50|$ and $df = 19$) during the 1963 to 2003 period (Welch and others, 1993; Curran and others, 2003). The relative abundance of DMS sources is believed to increase during years with increased sea ice fraction, as sea ice provides habitat for the marine biota which produce DMS. Within the polar pack, aquatic concentrations of DMS are highest at the pack edge, where it is believed that either meltwater from sea ice stabilizes the surface water column and maintains phytoplankton in the productive euphotic zone or the melting of sea ice releases microbes and their DMS from highly saline brine pockets within the sea ice (O'Dwyer and others, 2000; Trevena and Jones, 2006; Isaksson and others, 2006). Legrand and others (1997) attribute a post-

1945 decreasing trend in an MSA deposition record from central Greenland to either (i) increased tropospheric NO*x* concentrations, which have decreased the oxidation capacity of the atmosphere, or (ii) a decline in the marine biota which produce DMS. Our study potentially supports both hypotheses, as the long term mean NO_3^- deposition has a significant increasing trend between 1955 and 1995 ($p < 0.01$, $r = 0.61$ and $df = 19$), which is likely indicative of increased tropospheric NO*x* concentrations, and the sea ice record shows that the inferred habitat of the DMS producing marine biota has decreased since 1940.

Similar to previous studies, which have found negative correlations between sea-salt concentrations in the Penny and Devon Island Ice Caps and the sea ice fraction of southern Baffin Bay (Grumet and others, 2001; Kinnard and others, 2006), we find a negative correlation between Cl^- deposition (core C 3-year running mean) and local ONDJF sea ice variability in southern Baffin Bay (PC3; $p < 0.01$ $r = -0.63$ and $df = 19$), which suggests increased Cl^- deposition on the Devon Island Ice Cap during years of relatively decreased local sea ice fraction in southern Baffin Bay. Additionally, we also find evidence of a positive correlation between Cl^- deposition and the regional decrease in ONDJF sea ice fraction (PC1; $p < 0.05$, $r = 0.42$ and $df = 19$). As we can provide no physical explanation, we discount the apparent positive relationship between regional sea ice fraction decline and Cl^- deposition. Instead, we interpret the non-significant ($p < 0.05$) decreasing trend in Cl^- deposition between 1963 and 2003 as evidence of increasing atmospheric HCl_g concentrations over time. If sea salt aerosol emission is assumed to have been relatively constant since the beginning of the period of comparison (1963), while the atmospheric H_2SO_4 concentration is assumed to have increased over this period (as suggested by the SO_4^{2-} deposition record), then atmospheric HCl_g production would be expected to have increased since 1963. As the Cl^- in HCl_g is not effectively scavenged by snowfall, a decreasing trend would be expected in snowfall Cl^- concentrations over time, due to a decreasing availability of Cl^-. Therefore, the decreasing trend in Cl^- deposition between 1963 and 2003 is more likely attributable to an increase in atmospheric H_2SO_4 concentration, rather than the decreasing trend in sea ice fraction with which it is correlated.

4.4.5 – Arctic Oscillation

Previous ice core studies have suggested both increased pollutant and sea-salt transport to Baffin Island and western Greenland during NAO+ and AO+ phases (Grumet and others, 2001; Burkhart and others, 2006). The core C residual SO_4^{2-}, MSA and Cl^- deposition records, assumed to have main source emission variability removed, were compared to the 3-year running mean AO index (NOAA, 2005) during their respective transport seasons (NDJF for SO_4^{2-}, MJJAS for MSA and ONDJF for Cl^-). The timeseries of the AO and NAO are highly correlated ($r = 0.92$), but the AO has been shown to provide a more hemispheric signal than the NAO (Ambaum and others, 2001). None of the three residual anion deposition records were found to be significantly correlated ($p > 0.05$, $r < |0.39|$ and $df = 19$) with their respective seasonal AO indices during the 1963 to 2003 period. The AO index however, is recognized to be a limited measure of hemispheric atmospheric variability, as the changes in atmospheric distribution observed between positive and negative phases are the result of at least three modes of atmospheric variability, rather than a single over-arching mode of variability (Maslanik and others, 2007). Annual timeseries of the individual modes of atmospheric variability which comprise the AO are not available for detailed correlation studies at this time (Maslanik and others, 2007). When correlating the 3-year running mean core C deposition records with their respective seasonal AO indices, it must be remembered that annual anion deposition is a function of annual anion concentration and annual net accumulation. Therefore, the potential exists to misinterpret seasonal AO-induced variability in net accumulation, and not anion delivery, as AO-induced anion deposition variability. The annual net accumulation of the Devon Island Ice Cap however, does not appear to be correlated with AO phase during the 1963 to 2003 period (Chapter 2).

4.5 – CONCLUSION

Five long term SO_4^{2-}, NO_3^-, MSA and Cl^- deposition records, dated using the Nye time-scale, with the oldest extending back to 1922, were reconstructed from shallow firn cores recovered from the high elevation region of the Devon Island Ice Cap. These records were used to examine long term trends in anion deposition. The five individual deposition records of each anion were found to have good correlation and signal-to-noise

ratios with their respective mean deposition records. In addition to these long term records, annual layer counting was used to create a shorter term annually resolved record of anion deposition at the highest elevation core site (core C) for the 1963 to 2003 period. This record was used to explore the influences of inter-annual variability in anion sources and transport variability on anion deposition. A comparison of the 1963 to 2003 portion of core C dated using both the Nye and counted time-scales suggests periods with dating differences of up ± 2 years and annual anion deposition differences of between ± 44 and 110 % (depending on anion species). The Nye time-scale overestimates (underestimates) deposition during low (high) net accumulation periods in comparison to the counted time-scale.

The long term mean SO_4^{2-} deposition record was found to have a significant increasing (1943 -1990) and decreasing (1991 - 2003) trends, while the long term mean NO_3^- deposition record was found to have a significant increasing trend (1955 - 1995). The SO_4^{2-}:NO_3^- ratio exhibits a significant decreasing trend between 1985 and 2003, which is due to a decrease in SO_4^{2-} deposition relative to NO_3^- deposition. The annually counted core C record suggests that the majority of variation in SO_4^{2-} deposition (r^2 = 0.62) can be explained by variation in the anthropogenic SO_2 emissions of Western and Eastern Europe, Northern Asia and North America, although North America appears to be the primary source region. A site-specific long-range atmospheric transport record, constructed from daily 120 hr back-trajectories, did not identify a dominant transport route to the Devon Island Ice Cap during polar night (NDJF) which could influence SO_4^{2-} or NO_3^- transport to the ice cap.

The long term MSA deposition record had a significant decreasing trend between 1940 and 2003. The core C short term MSA deposition record is significantly correlated to the summertime (MJJAS) sea ice PC1, which describes a significant decreasing trend in regional sea ice fraction. Although the site-specific low elevation atmospheric transport record revealed a primary mode of variance, a Beaufort Sea-Baffin Bay dipole, during the MJJAS season, this mode of atmospheric variability was not reflected in the residual core C MSA deposition record. Therefore, sea ice variability appears to have a stronger influence on MSA deposition variability than variability in site-specific low elevation atmospheric transport.

Aside from a decreasing trend between 1922 and 1938, the core C Cl^- deposition record exhibited no significant trend since 1939. The core C Cl^- deposition record is significantly correlated to the wintertime (ONDJF) sea ice fraction PC3, which suggests increased Cl^- deposition on the Devon Island Ice Cap during years of relatively decreased local sea ice fraction in southern Baffin Bay. Although the non-significant decreasing trend in Cl^- deposition between 1963 and 2003 is positively correlated to the decreasing trend in regional wintertime (ONDJF) sea ice fraction (PC1), we speculate that the Cl^- deposition record is evidence of decreased Cl^- scavenging due to increased atmospheric HCl_g production since 1963. A primary mode of site-specific low elevation atmospheric transport during the ONDJF season, a Beaufort Sea-Baffin Bay dipole similar in structure to the MJJAS primary mode of atmospheric variability, was not significantly correlated to the residual core C Cl^- deposition record. Therefore, as with MSA deposition, we suggest that sea ice variability is more important than site-specific low elevation atmospheric transport variability in determining Cl^- deposition variability.

4.5 – LITERATURE CITED

Ambaum, M., B. Hoskins and D. Stephenson. 2001. Arctic Oscillation or North Atlantic Oscillation? *J. Climate*. **14**, 3495-3507.

Burkhart, J., R. Bales, J. McConnell and M. Hutterli. 2006. Influence of North Atlantic Oscillation on anthropogenic transport recorded in northwest Greenland ice cores. *J. Geophys. Res.* **111** (D22309), doi:10.1029/2005JD006771.

Cavalieri, D., P. Gloersen, C. Parkinson, J. Comiso and H. Zwally. 1997. Observed hemispheric asymmetry in global sea ice changes. *Science*. **278**, 1104-1106.

Chapman, W. and J. Walsh. 1993. Recent variation of sea ice and air temperature in high latitudes. *Bull. Amer. Meteor. Soc.* **74**, 33-47.

Curran, M., T. van Ommen, V. Morgan, K. Phillips and A. Palmer. 2003. Ice core evidence for Antarctic sea ice decline since the 1950s. *Science*. **302**, 1203-1206.

Davis, D., G. Chen, P. Kasibhatla, A. Jefferson, D. Tanner, F. Eisele, D. Lenschow, W. Neff and H. Berresheim. 1998. DMS oxidation in the Antarctic marine boundary layer: comparison of model simulations and field observations of DMS, DMSO, $DMSO_2$, H_2SO_4(g), MSA(g), and MSA(p). *J. Geophys. Res.* **103**, 1657-1678.

Dowdeswell, J., T. Benham, M. Gorman, D. Burgess and M. Sharp. 2004. Form and flow of the Devon Island Ice Cap, Canadian Arctic. *J. Geophys. Res.* **109** (F02002), doi:10.1029/2003JF000095.

Eckhardt, S., A. Stohl, S. Beirle, N. Spichtinger, P. Kames, C. Forster, C. Junker, T. Wagner, U. Platt and S. Jennings. 2003. The North Atlantic Oscillation controls air pollution transport to the Arctic. *Atmos. Chem. Phys.* **3**, 1769-1778.

Fischer, H., M. Siggaard-Andersen, U. Ruth, R. Rothlisberger and E. Wolff. 2007.

Glacial/interglacial changes in mineral dust and sea-salt records in polar ice cores: sources, transport, and deposition. *Rev. Geophys.* **45** (RG1002), doi:10.1029/2005RG000192.

Foster, K., R. Plastridge, J. Bottenheim, P. Shepson, B. Finlayson-Pitts and C. Spicer. 2001. The role of Br_2 and BrCl in surface ozone destruction at polar sunrise. *Science*. 291: 471-474.

Galloway, J., J. Aber, J. Risman, S. Seitzinger, R. Howarth, E. Cowling and B. Cosby. 2003. The nitrogen cascade. *Bioscience*. **53,** 341-356.

Goto-Azuma, K. and R. Koerner. 2001. Ice core studies of anthropogenic sulphate and nitrate trends in the Arctic. *J. Geophys. Res.* **106**, 4959-4969.

Goto-Azuma, K., R. Koerner and D. Fisher. 2002. An ice-core record over the last two centuries from Penny Ice Cap, Baffin Island, Canada. *Ann. Glaciol.* **35,** 29-35.

Grumet, N., C. Wake, P. Mayewski, G. Zielinski, S. Whitlow, R. Koerner, D. Fisher and J. Woollett. 2001. Variability of sea-ice extent in Baffin Bay over the last millennium. *Climate Change*. **49**, 129-145.

Hastings, M., E. Steig and D. Sigman. 2004. Seasonal variation in N and O isotopes of nitrate in snow at Summit, Greenland: implications for the study of nitrate in snow and ice cores. *J. Geophys. Res.* **109** (D20306), doi:10.1029/2009JD004991.

Hauglustaine, D., C. Granier, G. Brasseur and G. Mégie. 1994. The importance of atmospheric chemistry in the calculation of radiative forcing on the climate system. *J. Geophys. Res.* **99**, 1173-1186.

Holland, E. and J. Lamarque. 1997. Modeling bio-atmospheric coupling of the nitrogen cycle through NO*x* emissions and NO*y* deposition. *Nutrient Cycling in Agroecosystems*. **48**, 7-24.

Isaksson, E., T. Kekonen, J. Moore and R. Mulvaney. 2006. The methanesulphonic acid (MSA) record in a Svalbard ice core. *Ann. Glaciol.* **42**, 345-351.

Iziomon, M., U. Lohmann and P. Quinn. 2006. Summertime pollution events in the Arctic and potential implications. *J. Geophys. Res.* **111** (D12206), doi:10.1029/2005JD006223.

Johannessen, O., L. Bengtsson, M. Miles, S. Kuzmina, V. Semenov, G. Alekseev, A. Nagurnyi, V. Zakharov, L. Bobylev, L. Pettersson, K. Hasselmann and H. Cattle. 2004. Arctic climate change: observed and modelled temperature and sea-ice variability. *Tellus*. **56A,** 328-341.

Kahl, J., D. Martinez, H. Kuhns, C. Davidson, J. Jaffrezo and J. Harris. 1997. Air mass trajectories to Summit, Greenland: a 44-year climatology and some episodic events. *J. Geophys. Res.* **102,** 26,861-26,875.

Kahl, J., J. Galbraith and D. Martinez. 1999. Decadal-scale variability in long-range atmospheric transport to the Summit of the Greenland Ice Sheet. *Geophys. Res. Lett.* **26**, 481-484.

Kaleschke, L., A. Richter, J. Burrows, O. Afe, G. Heygster, J. Notholt, A. Rankin, H. Roscoe, J. Hollwedel, T. Wagner and H. Jacobi. 2004. Frost flowers on sea ice as a source of sea salt and their influence on tropospheric halogen chemistry. *Geophys. Res. Lett.* **31** (L16114), doi.10.1029/2004GL020655.

Kalnay, E., M. Kanamitsu, R. Kistler, W. Collins, D. Deaven, L. Gandin, M. Iredell, S. Sasha, G. White, J. Woollen, Y. Zhu, M. Chelliah, W. Ebisuzaki, W. Higgins, J.

Janowiak, K. Mo, C. Ropelewski, J. Wang, A Leetmaa, R. Reynolds, R. Jenne and D. Joseph. 1996. The NCEP/NCAR 40-year reanalysis project. *Bull. Amer. Meteor. Soc.* **77**, 437-471.

Keene, W., A. Pszenny, J. Galloway and M. Hawley. 1986. Sea-salt corrections and interpretation of constituent ratios in marine precipitation. *J. Geophys. Res.* **91**, 6647-6658.

Kinnard, C., C. Zdanowicz, D. Fisher and C. Wake. 2006. Calibration of an ice-core glaciochemical (sea slat) record with sea ice variability in the Canadian Arctic. *Ann. Glaciol.* **44**, 383-390.

Legrand, M., C. Hammer, M. De Angelis, J. Savarino, R. Delmas, H. Clausen and S. Johnsen. 1997. Sulfur-containing species (methanesulfonate and SO_4) over the last climate cycle in the Greenland Ice Core Project (central Greenland) ice core. *J. Geophys. Res.* **102**, 26,663-26,679.

Legrand, M. and P. Mayewski. 1997. Glaciochemistry of polar ice cores: a review. *Rev. Geophys.* **35**, 219–243.

Li, S. and L. Barrie. 1993. Biogenic sulfur aerosol in the Arctic troposphere, 1, contributions to sulphate. *J. Geophys. Res.* **98**, 20,623-20,631.

Maslanik, J., S. Drobot, C. Fowler, W. Emery and R. Barry. 2007. On the Arctic climate paradox and the continuing role of atmospheric circulation in affecting sea ice conditions. *Geophys. Res. Lett.* **34** (L03711), doi.10.1029/2006GL028269.

Moore, J., T. Kekonen, A. Grinsted and E. Isaksson. 2006. Sulfate source inventories from a Svalbard ice core record spanning the Industrial Revolution. *J. Geophys. Res.*, 111 (D15307), doi: 10.1029/2005JD006453.

Nye, J. 1963. Correction factor for accumulation measured by the ice thickness of the annual layers in an ice sheet. *J. Glaciol.* **4**, 141-150.

NOAA, 2005: The Arctic Oscillation Index. http://cpc.ncep.noaa.gov/products/precip/Cwlink/daily_ao_index/ao_index.html. Accessed 13 August 2005.

Norman, A., L. Barrie, D. Toom-Sauntry, A. Sirois, H. Krouse, S. Li and S. Sharma. 1999. Sources of aerosol sulphate at Alert: Apportionment using stable isotopes. *J. Geophys. Res.* **104**, 11,619-11,631.

O'Dwyer, J., E., Isaksson, T. Vinje, T. Jauhiainen, J. Moore, V. Pohjola, R. Vaikmae and R. van de Wal. 2000. Methanesulfonic acid in a Svalbard ice core as an indicator of ocean climate. *Geophys. Res. Lett.* **27**, 1159-1162.

Pasteur, E., R. Mulvaney, D. Peel, E. Saltzman and P. Whung. 1995. A 340-year record of biogenic sulphur from the Weddell Sea area, Antarctica. *Ann. Glaciol.* **21**, 169-174.

Pohjola, V., T. Martma, H. Meijer, J. Moore, E. Isaksson, R. Vaikmäe, R. van de Wal. 2002. Reconstruction of three centuries of annual accumulation rates based on the record of stable isotopes of water from Lomonosovfonna, Svalbard. *Ann. Glaciol.* **35**, 57-62.

Preisendorfer, R. 1988. *Principal component analysis in meteorology and oceanography*. Ed. C. Mobley. Elsevier. pp. 199-206.

Reijmer, C., M. van der Broeke and M. Scheele. 2002. Air parcel trajectories and snowfall related to five deep drilling locations in Antarctica based on the ERA-15 dataset. *J. Climate*. **15**, 1957-1968.

Sander, R., R. Vogt, G. Harris and P. Crutzen. 1997. Modeling the chemistry of ozone,

halogen compounds, and hydrocarbons in the arctic troposphere during spring. *Tellus*. **49B**, 522-532.

Shaw, G. 1995. The Arctic haze phenomenon. *Bull. Amer. Meteor. Soc.* **76**, 2403-2413.

Singarayer, J. and J. Bamber. 2003. EOF analysis of three records of sea-ice concentration spanning the last 30 years. *Geophys. Res. Lett.* **30**, 1251-1255. doi:10.1029/2002GL016640.

Sirois, A. and L. Barrie. 1999. Arctic lower tropospheric aerosol trends and composition at Alert, Canada: 1980–1995. *J. Geophys. Res.* **104**, 11,599-11,618.

Slater, J., J. Dibb, B. Keim and J. Kahl. 2001. Relations between synoptic-scale transport and interannual variability of inorganic cations in surface snow at Summit, Greenland: 1992-1996. *J. Geophys. Res.* **106**, 20,897-20,912.

Stern, D. 2005. Global sulfur emissions from 1850 to 2000. *Chemosphere*. **58**, 163–175.

Stohl, A. 2006. Characteristics of atmospheric transport into the Arctic troposphere. *J. Geophys. Res.* **111** (D11306), doi:10.1029/2005JD006888.

Toom-Sauntry, D and L. Barrie. 2002. Chemical composition of snowfall in the high Arctic: 1990–1994. *Atmos. Environ.* **36**, 2683-2693.

Trevena, A. and G. Jones. 2006. Dimethylsulphide and dimethylsulphonpropionate in Antarctic sea ice and their release during sea ice melting. *Marine Chemistry*. **98**, 210-222.

Walsh, J. 1978. A data set on Northern Hemisphere sea ice extent: World Data Center-A for Glaciology (Snow and Ice). *Glaciological Data, Report GD-2 Part 1*. 49-51.

Walsh, J. and C. Johnson. 1979. An analysis of Arctic sea ice fluctuations, 1953-77. *J. Phys. Ocean.* **9**, 580-591.

Walsh, J. and W. Chapman. 2001. 20th-century sea-ice variations from observational data. *Ann. Glaciol.* **33**, 444-448.

Walsh, J. and W. Chapman. 2006. Walsh and Chapman Northern Hemisphere Sea Ice Data Set. http://arctic.atmos.uiuc.edu/SEAICE/. Accessed 15 June 2006.

Welch, K., P. Mayewski and S. Whitlow. 1993. Methanesulfonic acid in coastal Antarctic snow related to sea-ice extent. *Geophys. Res. Lett.* **20**, 443-446.

Zeng, J., M. Katsumoto, R. Ide, M. Inagaki, H. Mukai and Y. Fujinuma. 2003. Development of meteorological data explorer for Windows. In: *Data Analysis and Graphic Display System for Atmospheric Research Using PC*. Ed. Y. Fujinuma. CGER-M014-2003. Center for Global Environmental Research, NIES, 19-72.

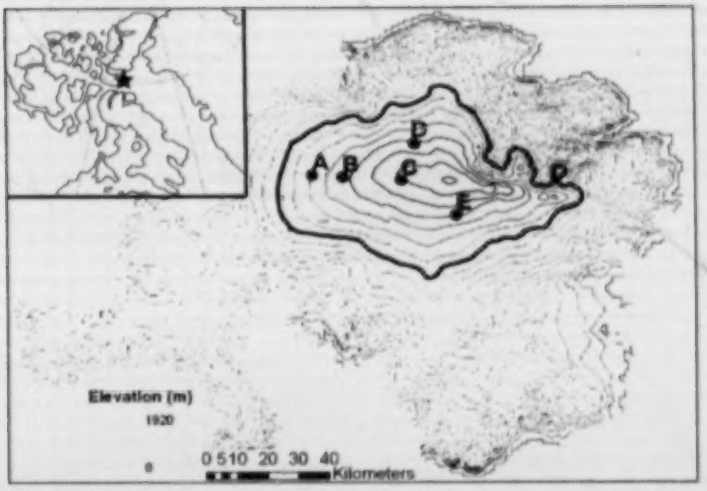

Figure 4-1 – Shaded contour map of the Devon Island Ice Cap (100 m interval), with the high elevation region enclosed by the 1200 m contour (black line) and the locations of the five shallow firn cores (A, B, C, D and E) shown. **Inset:** Devon Island within the Canadian Arctic Archipelago.

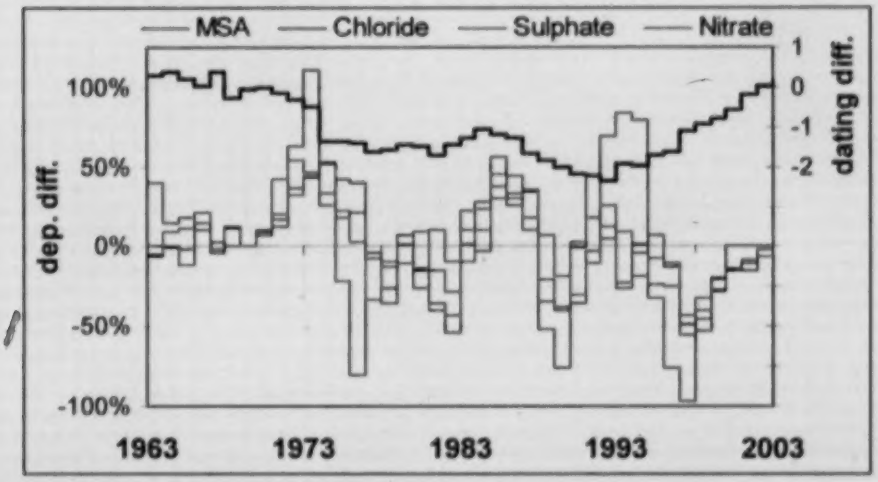

Figure 4-2 – Counted and Nye time-scale comparisons: differences in the 3-year running mean SO_4^{2-}, NO_3^-, MSA and Cl^- deposition records (counted time-scale deposition values are expressed as an anomaly from the Nye time-scale deposition values and normalized by the 1963 to 2003 Nye time-scale mean) and differences in the dating of annual layers (counted years are expressed relative to Nye time-scale years; black line).

scale anion deposition (Figure 4-2). These periods correspond approximately with the periods of lower and higher reconstructed net accumulation respectively (Chapter 2).

4.3.2 – Long term anion records: trends

During the 1958 to 2003 period common to all five cores, the 3-year running mean long term mean deposition record of each anion in the 5 cores appears to be representative of the individual 3-year running mean deposition records which comprise it (Figure 4-3). All five individual SO_4^{2-} deposition records are positively correlated with the long term mean SO_4^{2-} deposition record ($p < 0.01$, $r > 0.50$ and $df = 21$), while four individual MSA (A, B, D and E) and Cl^- (A, B, C and E) deposition records are positively correlated to their respective long term mean deposition records ($p < 0.05$, $r > 0.37$ and $df = 21$), and three individual NO_3^- records (A, D and E) are correlated to the long term mean NO_3^- deposition record ($p < 0.05$, $r > 0.37$ and $df = 21$; Table 4-3). Although core site A is at the lowest elevation (1415 m) of the five core sites, experiencing the most melt and potential anion redistribution, its individual anion deposition records are all well-correlated with the long term mean anion deposition records from the 5-core ensemble ($p < 0.01$, $r > 0.50$ and $df = 21$).

Trends, defined here as significant deposition-time regressions, were assessed in each of the long-term mean anion deposition records during the 1922 to 2003 period. Trend break points were defined by recalculating the 3-year running mean annual anion deposition values as departures from long term mean annual anion deposition values, and identifying inflection points in a plot of cumulative departure from the long term mean versus time function of each anion. The 3-year running mean SO_4^{2-} deposition record had an increasing trend between 1943 and 1990 ($p < 0.05$, $r = 0.36$ and $df = 22$) and a decreasing trend between 1991 and 2003 ($p < 0.05$, $r = -0.90$ and $df = 5$; Figure 4-3). The 3-year running mean MSA deposition record had a decreasing trend between 1940 and 2003 ($p < 0.01$, $r = -0.79$ and $df = 30$; Figure 4-3). The 3-year running mean Cl^- deposition had a decreasing trend between 1922 and 1938 ($p < 0.05$, $r = -0.78$ and $df = 7$; Figure 4-3). Although the 3-year running mean NO_3^- deposition record contained no significant trends ($p > 0.05$) in the periods identified using break point analysis (1922 to 1962 and 1963 to 2003), a significant increasing trend ($p < 0.01$, $r = 0.61$ and $df = 19$)

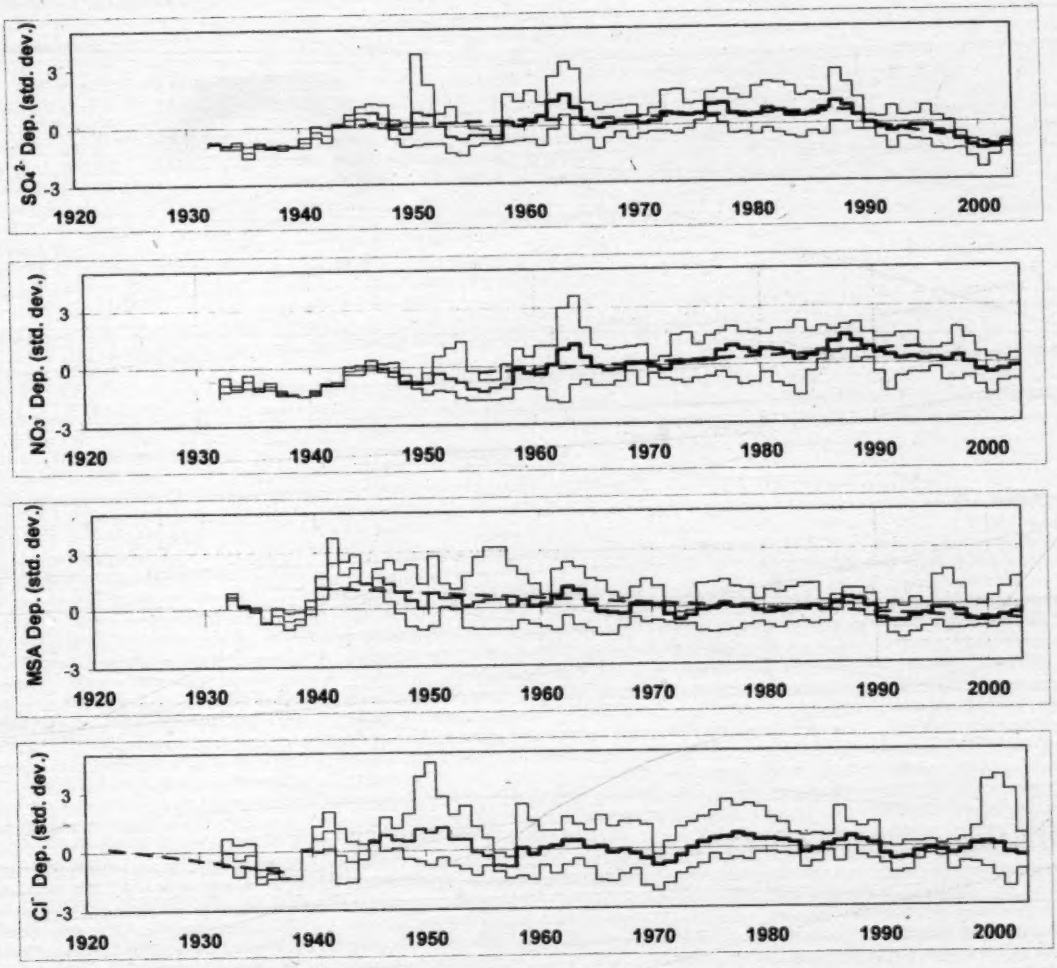

Figure 4-3 – The 3-year running mean SO_4^{2-} (**Top**), NO_3^- (**Second from top**), MSA (**Second from bottom**) and Cl^- (**Bottom**) deposition records. The thickness of the mean line reflects the number of cores comprising it. The grey lines represent maximum and minimum annual deposition values. Dashed lines indicate significant trends ($p < 0.05$).

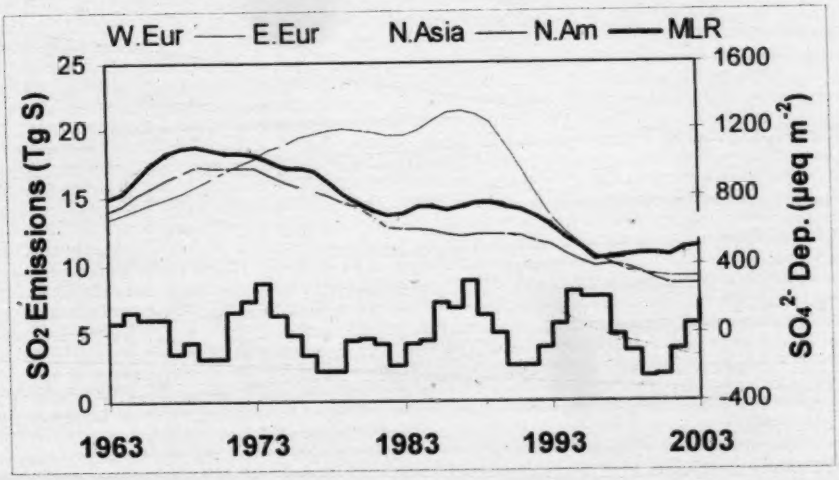

Figure 4-4 – The 3-year running mean SO_2 emissions from Western and Eastern Europe, Northern Asia and North America (Stern, 2005). The residual SO_4^{2-} deposition record (black line) was derived by regressing the 3-year running mean MLR SO_2 emission record against the 3-year running mean core C SO_4^{2-} deposition record ($p < 0.01$, adjusted $r = 0.79$ and $df = 19$; grey line).

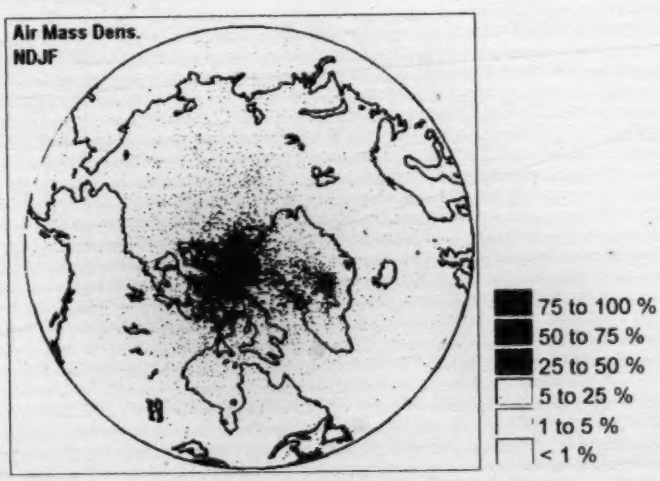

Figure 4-5 – The mean November through February (NDJF) seasonal densities of air masses en route to the Devon Island Ice Cap (D_{SX}; Equation 4-4) during the 1979 to 2003 period. D_{SX} values are classified as a percentage of the maximum D_{SX} value. The initiation points of each daily 120 hr back-trajectory are shown (points).

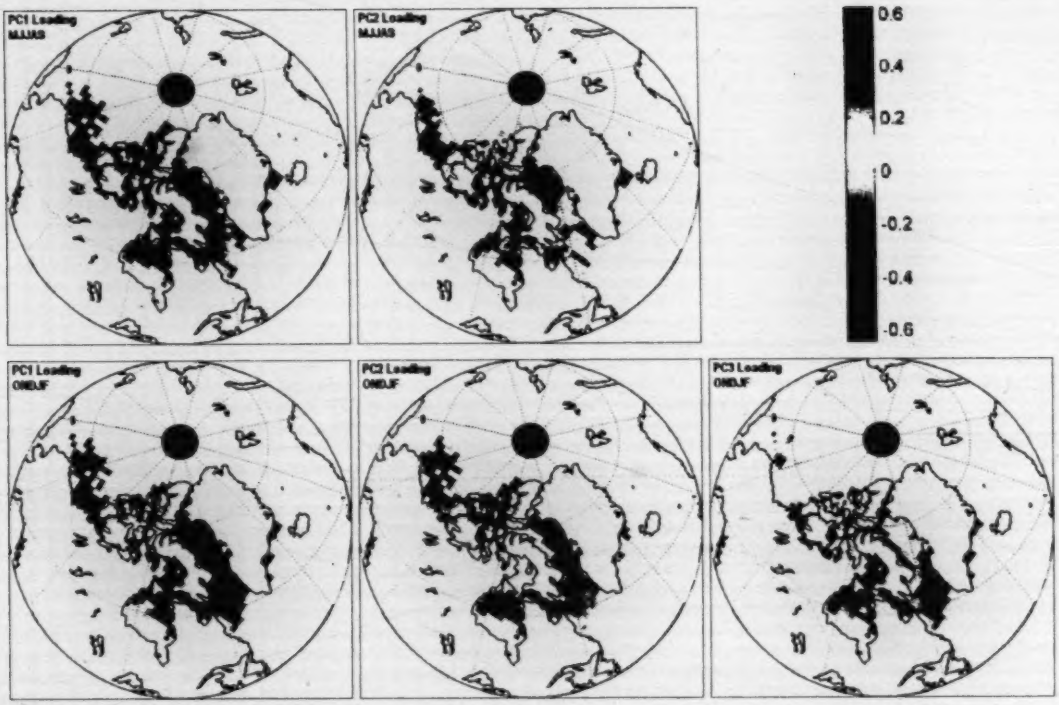

Figure 4-6 – The loading patterns of May through September (MJJAS; **Top**) sea ice fraction PCs ($n = 45$ and $p = 339$) and October through February (ONDJF; **Bottom**) sea ice fraction PCs ($n = 45$ and $p = 345$; Walsh and Chapman, 2006). White cells indicate regions of open water.

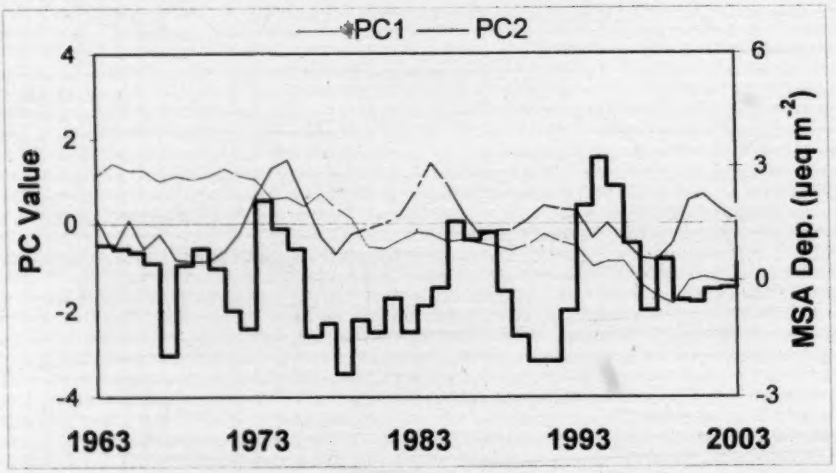

Figure 4-7 – The 3-year running mean MJJAS sea ice PCs 1 and 2 (Walsh and Chapman, 2006). The residual MSA deposition record (black line) was derived by regressing the 3-year running mean MJJAS PC1 against the 3-year running mean core C MSA deposition record ($p < 0.01$, $r = 0.65$ and $df = 19$; grey line).

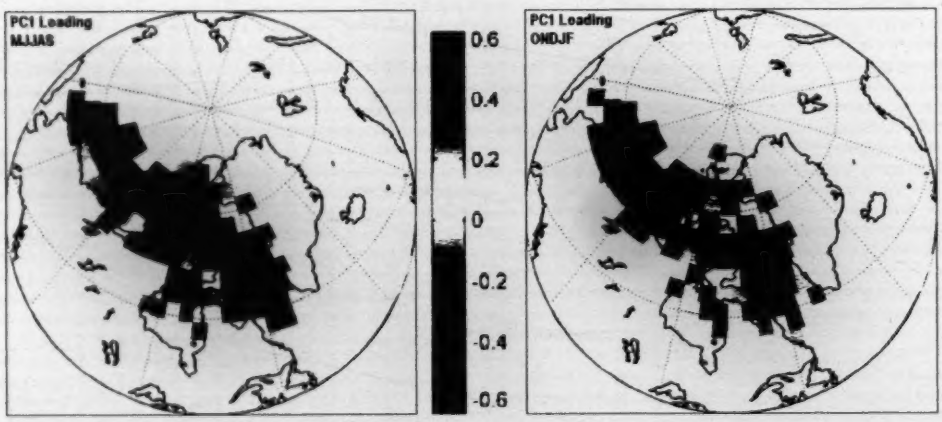

Figure 4-8 – The loading pattern of May through September (MJJAS; **Left**) and October through February (ONDJF; **Right**) low elevation (< 500 m) air mass density fraction PC1 ($n = 24$ and $p = 94$) within the previously defined moisture source region of interest (Chapter 2), during the 1979 to 2003 period.

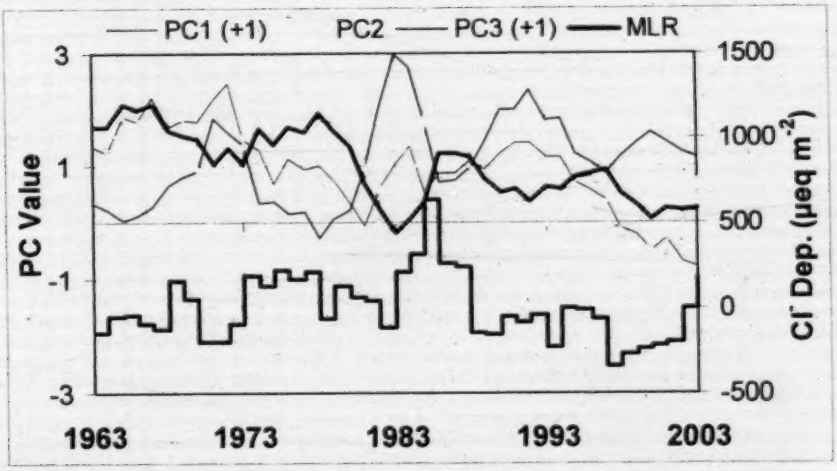

Figure 4-9 – The 3-year running mean ONDJF sea ice PCs 1, 2 and 3 (Walsh and Chapman, 2006). The residual Cl^- deposition record (black line) was derived by regressing the 3-year running mean MLR record against the 3-year running mean core C Cl^- deposition record ($p < 0.01$, adjusted $r = 0.72$ and $df = 19$; grey line).

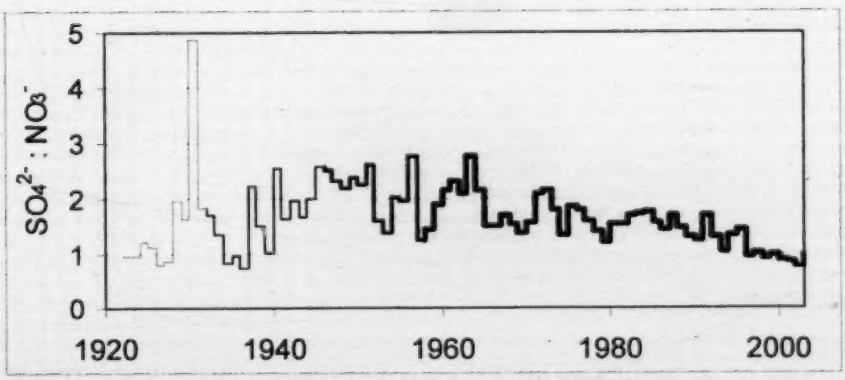

Figure 4-10 – The 3-year running mean SO_4^{2-}:NO_3^- of the five shallow firn cores. The thickness of the line corresponds to the number of cores comprising the mean.

Table 4-1 – The elevation, mean annual net accumulation between 1963 and 2003 (c; Chapter 2), ice thickness (h; Dowdeswell and others, 2004) and the oldest Nye time-scale year (t_o) at each core site.

	Elevation (m)	c (mWE a^{-1})	h (mWE)	t_o
Core A	1825	0.221	523	1932
Core B	1630	0.229	625	1958
Core C	1525	0.246	494	1950
Core D	1525	0.174	431	1922
Core E	1415	0.235	454	1946

Table 4-2 – The 3-year running mean deposition (± standard deviation) of each anion at each core site.

	SO_4^{2-} (μeq m^{-2})	NO_3^- (μeq m^{-2})	MSA (μeq m^{-2})	Cl^- (μeq m^{-2})
Core A	554.4 ± 269.9	309.2 ± 105.0	2.88 ± 2.67	580.5 ± 132.0
Core B	762.3 ± 339.2	362.7 ± 88.3	2.62 ± 1.57	421.1 ± 90.9
Core C	765.0 ± 188.1	659.2 ± 255.1	3.02 ± 1.49	779.6 ± 231.4
Core D	308.3 ± 152.5	207.6 ± 86.2	3.96 ± 2.65	492.2 ± 145.7
Core E	575.7 ± 295.2	309.6 ± 123.0	2.92 ± 2.25	623.0 ± 440.9

Table 4-3 – Correlation coefficients (r) between the 3-year running mean deposition records of each core and the 3-year running mean standard normalized long term mean deposition record, during the 1958 to 2003 period common to all five cores (* $p < 0.05$; ** $p < 0.01$ and $df = 21$). Signal-to-noise ratios ($r / (1 - r)$; Goto-Azuma and others, 2002) are given in parentheses.

	SO_4^{2-}	NO_3^-	MSA	Cl^-
Core A	0.77** (3.41)	0.77** (3.38)	0.57** (1.31)	0.59** (1.46)
Core B	0.69** (2.19)	0.31 (0.46)	0.50* (1.01)	0.40* (0.68)
Core C	0.58** (1.40)	0.34 (0.51)	0.36 (0.56)	0.53** (1.14)
Core D	0.68** (2.13)	0.48* (0.91)	0.44* (0.79)	0.21 (0.26)
Core E	0.81** (4.16)	0.77** (3.32)	0.71** (2.49)	0.50* (1.01)

5.1 – CONCLUSION

5.1.1 – Thickening scenarios

As discussed in Chapter 1, the continuity equation for ice thickness suggests that the positive rate of thickness change observed along the laser altimetry flight lines could arise from four basic scenarios: (i) if the long term net accumulation rate has remained constant or increased and the rate of outflow has decreased; (ii) if the rate of outflow has remained constant or decreased and the long term net accumulation rate has increased; (iii) if both the outflow and net accumulation rates have decreased, as long as the effect of the decrease in outflow is greater than that of the decrease in net accumulation; and (iv) if both the outflow and net accumulation rates have increased, as long as the net accumulation rate has increased relatively more than the outflow rate. Although thickening may also be due to a decrease in the rate of firnification, which would result in a decrease in the density of the surface snow pack, the firnification rate in the high elevation region of the Devon Island Ice Cap has been shown to be increasing, rather than decreasing (Chapter 3). Therefore, the thickening observed by laser altimetry is unlikely to be due to a change in the rate of firnification.

$$\frac{dh}{dt} = -\frac{dQ}{dx} + \dot{B} \qquad \text{Equation 5-1}$$

Similar to a previous study (Koerner, 2005), this investigation has found that reconstructed annual net accumulation rate significantly decreased in the 1989 to 2003 period in comparison to the 1963 to 1988 period. The mean annual ice fraction was also higher in the 1989 to 2003 period than in the 1963 to 1988 period, implying a recent increase in the rate of firnification, likely due to increased atmospheric temperatures (Chapter 3). The observed thickening is therefore unlikely to be due to scenarios (i), (ii) and (iv), all of which invoke either anomalously high or constant net accumulation rates during the survey period relative to the long term mean. Therefore, this investigation suggests that scenario (iii), which invokes decreases in both the net accumulation and outflow rates, with the effect of the latter being greater than that of the former, is the most likely explanation for the observed thickening of the high elevation region of the Devon

Island Ice Cap. The proposed anomalously high net accumulation rate during the 1995 to 2000 survey period is therefore unlikely to explain the observed thickening (Abdalati and others, 2004).

5.1.2 – Ocean and atmospheric influences on snowfall and anion deposition

Inter-annual variability in both the reconstructed annual net accumulation and anion deposition records was assessed in the context of site-specific atmospheric transport and regional sea ice fraction variability. The coupling of these datasets to calculate moisture source probabilities identified northern Baffin Bay as the primary moisture source for the Devon Island Ice Cap during the July through October season. The secondary moisture source region for the Devon Island Ice Cap is far more extensive than the primary moisture source region, and includes southern Baffin Bay, the Queen Elizabeth Islands and a region extending into the Beaufort and Labrador Seas. A decline in May through September sea ice fraction throughout this region is positively correlated to the core C MSA deposition record, while sea ice fraction variability in southern Baffin Bay is correlated to the core C Cl^- deposition record.

The influence of anthropogenic emissions source variability is discernible in the core C SO_4^{2-} deposition record. North America and Western Europe are the most likely SO_2 emissions source areas for the Devon Island Ice Cap. On the inter-annual time-scale, source variability was found to explain the majority of the variability in the core C SO_4^{2-} and Cl^- deposition records, and a minority of the variability in the core C MSA deposition record. As atmospheric transport variability was found to have no discernible influence on the core C SO_4^{2-}, MSA and Cl^- deposition records, we attribute the remainder of the variability in these records to be due to deposition / post-depositional variability. We have no way of testing the validity of this assumption. This contrasts with the sources of Greenland glaciochemistry variability on the glacial / interglacial time-scale, where transport variability is believed to be the main source ice core variability, followed by source variability, with depositional variability having the smallest influence on ice core variability (Fischer and others, 2007).

5.1.3 – Contributions to glaciology

This examination of oceanic and atmospheric controls on net accumulation and anion deposition has resulted in three important developments: (i) the production of site-specific atmospheric transport and moisture source probability datasets; (ii) a comparison between laser altimetry-derived and field-based rates of thickness change; and (iii) the identification of discernible anion source variability signals within the anion deposition timeseries.

The method used in this investigation to calculate the site-specific atmospheric transport datasets is novel, in that it produces a gridded dataset from which primary transport routes can be determined through principal components or empirical orthogonal function analyses. This is an improvement on the traditional practice of developing representative transport routes, as the mean of several back-trajectories (Reijmer and others, 2002). This novel back-trajectory gridded dataset was coupled to a gridded observed sea ice fraction record, to produce a novel statistical index of regional moisture source probabilities for the Devon Island Ice Cap. The methods employed in this thesis can be applied with relative ease to other sites throughout the Arctic, to study the atmospheric and oceanic influences on ion deposition or snowfall at other locations.

The assessment of laser altimetry-derived and field-based rates of high elevation thickness change highlight the strengths and weaknesses of both sampling methods, especially the uncertainty associated with extrapolating widespread trends and conclusions based on limited altimetry observations. Although the associated uncertainty in both methods is relatively large, in comparison to the rate of change, the 'true' uncertainty can only be quantified in the field-based calculations. The field-based rates of thickness change suggest that ice dynamics are variable at the flux basin scale, and therefore any future laser altimetry measurements should ensure that there is sufficient sampling in each flux basin.

Although positive correlations between MSA deposition and sea ice concentration or extent have been previously reported in the Antarctic and Svalbard (Curran and others, 2003; Isakkson and others, 2006), the positive correlation between MSA deposition and May through September sea ice fraction presented in this study, during the 1963 to 2003 period, is the first evidence of increasing MSA deposition with increasing sea ice fraction in the Canadian High Arctic. The MSA record reconstructed from the Devon Island Ice

Cap appears to have some value as a sea ice fraction proxy, while the SO_4^{2-} record is a good proxy for northern hemisphere anthropogenic SO_2 emissions.

5.1.4 – Future improvements

There are several opportunities to improve the methods used in this thesis for future investigations, namely: (i) improved core dating with oxygen isotopes, to better resolve the annual layers and allow layer counting throughout each entire core, which will reduce the uncertainty in the net accumulation and anion deposition records and improve timeseries analyses and correlations; (ii) cation analysis to compliment the anion analysis of each core, which should allow sea-salt (ss) and non sea-salt (nss) marine ion constituents to be assessed using the conservative Na^+ tracer, and therefore allow the marine source variability of some anions, such as SO_4^{2-}, to be assessed; (iii) annual mean temperature reconstructions in each core using oxygen isotopes, which will allow an assessment of whether the annual ice fraction is truly indicative of 'annual' temperature conditions or a few summer days; (iv) refined outflow calculations, by increasing the number of survey stakes, to decrease the size of flux basins and reduce the main source of uncertainty associated with thickness change; and (v) longer back-trajectories gridded to the same G4640 grid as the sea ice fraction dataset, to better capture emission transport across the Arctic front and better facilitate the coupling of these datasets to the higher resolution grid.

5.2 – LITERATURE CITED

Abdalati, W., W. Krabill, E. Frederick, S. Manizade, C. Martin, J. Sonntag, R. Swift, R. Thomas, J. Yungel and R. Koerner. 2004. Elevation changes of ice caps in the Canadian Arctic Archipelago. *J. Geophys. Res.* **109** (F04007), doi:10.1029/2003JF000045.

Burgess, D. and M. Sharp. 2004. Recent changes in areal extent of the Devon Ice Cap, Nunavut, Canada. *Arct., Antar., Alp. Res.* **36**, 261-271.

Curran, M., T. van Ommen, V. Morgan, K. Phillips and A. Palmer. 2003. Ice core evidence for Antarctic sea ice decline since the 1950s. *Science*. **302,** 1203-1206.

Fischer, H., M. Siggaard-Andersen, U. Ruth, R. Rothlisberger and E. Woff. 2007. Glacial/interglacial changes in mineral dust and sea-salt records in polar ice cores: sources, transport, and deposition. *Rev. Geophys.* **45** (RG1002), doi:10.1029/2005RG000192.

Isaksson, E., T. Kekonen, J. Moore and R. Mulvaney. 2006. The methanesulphonic

acid (MSA) record in a Svalbard ice core. *Ann. Glaciol.* **42**, 345-351.

Johannessen, O., L. Bengtsson, M. Miles, S. Kuzmina, V. Semenov, G. Alekseev, A. Nagurnyi, V. Zakharov, L. Bobylev, L. Pettersson, K. Hasselmann and H. Cattle. 2004. Arctic climate change: observed and modelled temperature and sea-ice variability. *Tellus*. **56A**, 328-341.

Koerner, R. 2005. Mass balance of glaciers in the Queen Elizabeth Islands, Nunavut, Canada. *Ann. Glaciol.* **42,** 417-423.

Reijmer, C., M. van der Broeke and M. Scheele. 2002. Air parcel trajectories and snowfall related to five deep drilling locations in Antarctica based on the ERA-15 dataset. *J. Climate*. **15**, 1957-1968.